Coherent And Incoherent Optical Source Based Cavity Enhanced Absorption Spectroscopy For Trace Molecule Sensing.

Thesis submitted for the degree of

Doctor of Philosophy (Science)

in

Physics (Experimental)

Submitted by

Ardhendu Pal

Department of Physics

University of Calcutta

2024

Dedicated to my muktinath, boromaa, paternal and maternal grandparents and supervisor…

Acknowledgement

Foremost, I want to express my sincere respect and gratitude to my supervisor Prof. Manik Pradhan. He has given me the opportunity to work in his lab at S. N. Bose National Centre for Basic Sciences. From the very first day he encouraged me, motivated me and showed me the hope and made me believe that I can do it. He continuously remains attached with his students from the very beginning and brings the work out of them by repeatedly pushing to accelerate the work speed. Very few professors like him make themselves involve completely with the students in such a manner. He becomes selfless when something needs to be done for his PhD students or for his lab and he has the potential to fearlessly move up to any extent depending on the situation. This provides a solid mental strength to his students, which is the crucial criterion in the PhD career. He have groomed me in several ways, his various important advices and instructions helped me a lot to improve my presentation skill and fluently present my research work in front of the audiences. Thank you sir for everything I received and learnt from you throughout this journey.

I would like to acknowledge S. N. Bose National Centre for Basic Sciences for providing me the fellowship throughout my PhD tenure and excellent research facilities. I also like to thank all the members of the academic section, accounts section, purchase section and administrative section of S. N. Bose National Centre for Basic Sciences for showing cooperation whenever required during this tenure.

When I joined this lab the senior most student of my sir Dr. Abhijit Maity made me familiar with this lab people and lab environment. I have learnt lot of things from him, how to handle different lab responsibilities, how to look at various research problems from different angle etc. So, I want to express my love and respect to Abhijit da. I also like to thank my seniors Dr. Mithun Pal, Dr. Sanchi Maithani and Dr. Akash Das for various valuable discussions. Mr. Biswajit Panda is one year senior to me in this lab, with him I first started to work on the experimental setups and later we have developed different experimental setup together. The support I received from him is enormous. Panda bhaiya you deserve a special thanks from my side. Dr. Puspendu Barik is a person with overflow of knowledge in varied direction

and never hesitates to share those knowledge to anyone who wants to know from him. I want to thanks Puspendu da for showing such a beloved gesture and personality. I am also thankful to other lab members Dr. Jayeta Bannerjee, Dr. Koushik Mondol, Mr. Souman Mondal, Mr. Soumyadipta Chakraborty, Ms. Indrayani Patra, Mr. Dinesh Chandra Dey and Ms. Anuradha Sett for helping me with my research works and for maintaining a friendly and healthy lab atmosphere. The chicken dinner party mostly cooked by the master chef of our lab Biswajit and Soumen shall be remembered.

I am grateful to my late grandfathers Dr. Bibhuti Bhushan Pal, Mr. Sushil Kumar Dutta and my late paternal grandmother Mrs. Durga Rani Pal for making my childhood and life colourful with their love, affections and blessings. I express my gratitude and love for my jamma late Mrs. Anjana Guha for her valuable presence in my life.

I also want to express my sincere respect to my maternal grandmother Mrs. Namita Dutta for her constant love, blessings and trust on me. I owe my sincere gratitude, respect and love to all my family members Kaku, Moni, Chotopimoni, Boropimoni, Chotopimosai, Boropimosai, Dadabhai, Didibhai, Mumpi, Roni, Manai, Jaya boudi, Animesh dada, Duggu, Masimoni, Mesomoni, Disona, Soumo, Debraj dada, Aviraj, Swagata dada and Jethu for standing beside me every time unconditionally throughout my life.

I extend my deepest appreciation to my seniors and juniors at SNBNCBS for the delightful companionship they provided throughout my tenure at the institution, in particular Jayeta di, Anupam da, Anirban da, Abhik da, Siddharta da, Anish da, Amrit da, Pratap da, Debayan da, Premasis da, Saniur da, Rajdeep, Jayarshi, Krishendu, Monodip, Riju, Subham, Anirban, Sayan, Arun, Shreya, Soma, Riya, Amrita, Prapti, Sayari, Sinjini, Ipshita, Saheli, Pallabi and Ananya for their invaluable assistance in every conceivable aspect, and for infusing joy into my life with their presence. Late night drama rehearsals for the Bose Fest, intense team meeting and strategy making for the tournaments at SNBNCBS shall be remembered.

Finally, I have to mention about the two persons my beloved mother and my beloved father, without their endless support and sacrifice nothing would have been possible. Sometimes I have busy schedule and have tremendous workloads in my lab and it becomes around 2 am to 3 am to return to my room and they are the person who remains awake waiting for my phone call to listen that I have returned to my room and getting into my bed. Whenever I felt low and demotivated during my PhD days I talked with my mother for hours and she helped me to strengthen my mind and encouraged me to move ahead. Before my any presentation I use to practice my talk by connecting to my mother over phone. She never gets bored to repeatedly listen to the same chanting of mine, further she gives me suggestions about my fluency, clarity and the time I took to present the talk after every round of practice. I have shared each and everything with them and they guided me towards the right direction every time. There are numerous things to speak about them which will not end if I start telling about it all. They have fulfilled all my needs and wishes before I spend a single word from my mouth. I cannot thank them or express my gratitude for them; I can only hug them and kiss them on their chicks. Lots of love for them and wish for their good health.

Lastly, it is all the grace and blessings of almighty that I have reached and unrevealed my life upto this point. I want to apologize to him for all the mistakes I may have done knowingly or unknowingly and ask him to forgive me if possible. Further, I have to wait and watch what he has planned and kept for me next.

~~~Ardhendu Pal

Table of contents

Abstract……xi

সারাংশ……..xii

List of publications related to Thesis work……xiv

List of publications apart from Thesis work……xv

Chapter: 1

Trace molecule sensing: why it is so important?

1.1 Introduction……..1

1.2 Why trace gas sensing is necessary?.....3

1.2.1 Environmental monitoring……..3

1.2.2 Biomedical diagnosis……4

1.2.3 Isotopic analysis……5

1.3 Detection methods of trace gas molecules……...6

1.4 References…….....…….7

Chapter: 2

Coherent and incoherent optical sources

2.1 Introduction……13

2.2 Coherent light source……....……13

2.2.1 Diode Laser……..14

2.2.2 Quantum cascade laser…….....14

2.3 Incoherent light source…….....16

2.3.1 Light-Emitting Diodes……16

2.4 References…….....17

Chapter: 3

Fundamental aspects of spectroscopy

3.1 Introduction……20
3.2 Infrared absorption spectroscopy……21
3.2.1 Vibrational spectroscopy……...22
3.2.2 Rotational spectroscopy……25
3.2.3 Ro-vibrational spectroscopy……..26
3.3 Spectral line width……28
3.4 Overview of techniques for trace gas analysis……..30
3.4.1 Tunable diode laser absorption spectroscopy……30
3.4.2 Photo acoustic spectroscopy……..31
3.4.3 Cavity ring-down spectroscopy……32
3.4.4 Incoherent broadband cavity enhanced spectroscopy……..32
3.4.5 Wavelength modulation spectroscopy……33
3.4.6 Differential optical absorption spectroscopy……..34
3.4.7 Fourier transform infrared spectroscopy…….....34
3.5 References…….....35

Chapter: 4

High-resolution investigation of spectral doublets in ^{15}N-β-site nitrous oxide isotopomer

4.1 Introduction……42
4.2 Experimental Section……45
4.3 Results and discussions……46
4.3.1 Setup parameters…….....46
4.3.2 High-resolution *l*-type doublet spectra of β-N_2O……..47
4.4.3 Determination of *l*-type doubling constant……52

4.3.4 Pressure broadening effect *l*-type doublet spectral transitions……54
4.3.5 Evaluation of band centres, rotational constants and centrifugal distortion constants…….....58
4.4 Conclusion…….....59
4.5 References…….....60

Chapter: 5

Study of doublet splittings in Δ vibrational state of $^{15}N^{14}N^{16}O$ using QCL based CRDS system

5.1 Introduction……63
5.2 Experimental technique……66
5.3 Results and discussions…….68
5.4 Conclusion…….....75
5.5 References……...75

Chapter: 6

Λ-doublet splittings of NO in $^2\prod_{3/2}$ and $^2\prod_{1/2}$ spin-split sub-bands at mid-IR

6.1 Introduction……78
6.2 Experimental section……....….81
6.3 Results and discussions…….82
6.3.1 Setup parameters……....82
6.3.2 Λ doublet spectral lines of NO……..83
6.3.3 Variation of doublet separation with rotational quantum number…….....87
6.3.4 Transition Dipole Moment and Herman-Wallis coefficients……...88
6.3.5 Pressure broadening coefficients and its variation with rotational quantum number…….....91

6.3.6 Variation of collisional cross-sections with rotational quantum number…….....…….....96
6.4 Conclusions…….97
6.5 References…….....……98

Chapter: 7

Development of a diode laser-based cavity-enhanced spectrometer for the detection of NO_2 levels in exhaust gas

7.1 Introduction……..102
7.2 Experimental setup…….....…….106
7.3 Result and discussions……108
7.3.1 Selection of interference free spectral region for NO_2 detection…108
7.3.2 Laser profile and Allan variance analysis……110
7.3.3 Measurement principle in cavity-enhanced absorption spectroscopy……...111
7.3.4 Minimum detection limit of nitrogen dioxide measured from the developed setup……114
7.3.5 Calibration of the developed experimental technique……115
7.3.6 Detection of nitrogen dioxide concentration in different exhaust air samples……117
7.4 Conclusion……118
7.5 References…….....119

Chapter: 8

UV-A light-induced low-energy barrier gas phase oxygen isotope exchange between carbon dioxide and nitrogen dioxide

8.1 Introduction…….124

8.2 Experimental method……..126
8.3 Results and discussions……...128
8.3.1 General observation……..128
8.3.2 Investigation of the stoichiometry of the reactants in isotopic exchange……...……..131
8.3.3 Assessment of reaction mechanism……132
8.4 Conclusion……....139
8.5 References……..…140

Chapter: 9

Development of a LED based cavity-enhanced spectrometer for high-sensitive detection of diacetyl in gas phase

9.1 Introduction……..143
9.2 Experimental……144
9.3 Results and discussions……..……145
9.4 Conclusions……..……152
9.5 References…….....…152

Chapter: 10

Summary and future perspective

10.1 Summary of the thesis……...156
10.2 Future perspective…….....158
10.2.1 Fundamental spectroscopic study of α-nitrous oxide……...158
10.2.2 Study of nitrogen dioxide from car exhaust…….....158

Abstract

Trace molecule sensing is an important field of current research for atmospheric-monitoring, biomedical-diagnosis and fundamental-spectroscopic analysis. High-sensitive spectroscopic techniques with proper resolution is necessary to detect these trace molecules precisely at ultra-low concentrations. We have developed, implemented and utilized high-sensitive cavity-enhanced absorption spectroscopy (CEAS) technique coupled with coherent and incoherent optical sources to study the fundamental-spectroscopic properties, isotopic-exchange and detect various trace molecules in gas-phase.

In this thesis, we have studied the Λ-type and *l*-type doublet feature in diatomic and linear-polyatomic molecule, respectively. High-resolution spectroscopic measurements of rotationally-resolved spectral-doublets were carried out by cavity ring-down spectroscopy (CRDS) coupled with a continuous-wave external-cavity quantum cascade laser (cw-EC-QCL). Several spectroscopic features have been explored that are influenced by the *l*-type doubling of the fine-structure lines of the site-specific beta-isotopomer of nitrous-oxide (N_2O), corresponding to $(11^10)\leftarrow(01^10)$ and $(12^20)\leftarrow(02^20)$ transition in the 7.8 μm mid-IR-region. We have studied the rotationally-resolved e- and f-components of the Λ-doublet splittings in the $(^2\prod_{1/2}$-$^2\prod_{1/2})$ and $(^2\prod_{3/2}$-$^2\prod_{3/2})$ allowed sub-bands of the v=1←0 fundamental vibrational-band of nitric-oxide (NO) molecule near mid-IR-region (5.2 μm). Several spectroscopic-parameters were determined for these doublet-spectral transitions.

Further, we have exploited CEAS technique to develop a simple and cost-effective optical detection method for high-sensitive and selective real-time measurement of nitrogen-dioxide (NO_2) levels using a diode laser operating at 406 nm. We have detected the NO_2 levels in different exhaust-gases employing this developed-setup.

Next, we provided the direct experimental evidence of ^{16}O- and ^{18}O-oxygen isotope-exchange between CO_2 and NO_2 which are simultaneously emitted into the atmosphere from common sources. A combined near-infrared and UV-Vis optical cavity-enhanced experimental investigations along with quantum-chemical calculations followed by reaction modelling study revealed that CO_2 and NO_2 can communicate isotopically by near-ultraviolet-driven NO_2 photolysis.

Finally, we reported the development of an optical system based on the incoherent broadband cavity-enhanced absorption spectroscopy coupled with LED source operating at 450 nm for the precise detection of diacetyl molecule in gas-phase. The sensor system was utilized for the detection of diacetyl concentration in different curd sample and beer. Thus, we developed and utilized different CEAS techniques and implemented them for varied perspective of studies.

সারাংশ

ট্রেস মলিকিউল শনাক্ত করা একটা গুরুত্বপূর্ণ গবেষণার দিক। এই শনাক্তকরণের মাধ্যম দিয়ে আমরা বায়ুমণ্ডল মনিটারিং, বায়ো মেডিকেল ডায়াগনসিস, কাইনেটিক স্টাডি এবং মৌলিক স্পেকট্রোস্কপিক বিশ্লেষণ করতে সক্ষম। উচ্চ সেন্সেটিভ স্পেকট্রোস্কপিক পদ্ধতি, সাথে সঠিক রেজোলিউশনের প্রয়োজন এই ট্রেস মলিকিউল গুলোকে স্বল্পমাত্রায় সনাক্ত করার জন্য। আমরা তৈরি করেছি, প্রয়োগ করেছি এবং ব্যবহার করেছি উচ্চ সেন্সিটিভ ক্যাভিটি এনহ্যান্সড অ্যাবসরপশন স্পেকট্রোস্কপি (CEAS) তার সাথে যুক্ত করে কোহারেন্ট এবং ইনকোহারেন্ট আলোর উৎস কে যাতে আমরা ফান্ডামেন্টাল স্পেক্টরস্কপিক প্রপার্টিজ, আইসোটোপিক এক্সচেঞ্জ এবং আরো বিভিন্ন বিষয়কে বিশ্লেষণ করতে পারি। আমরা সম্পূর্ণ কাজগুলো গ্যাস ফেসয়ে করেছি।

এই গবেষণার কাজে, আমরা যথাক্রমে ল্যামডা টাইপ ও এল টাইপ ডাবলেট এর বৈশিষ্ট্য যা ডাইয়াটোমিক ও লিনিয়ার পলিয়াটমিক মলিকিউলে খুঁজে পাওয়া যায় তা অধ্যায়ন করেছি। উচ্চ রেজোলিউশন স্পেক্ট্রোস্কোপিক পরিমাপ করা হয়েছে রোটেশনালি রিসলভড স্পেক্ট্রাল ডাবলেটস এর জন্য। এই পরিমাপ করার জন্য ব্যবহার করা হয়েছে ক্যাভিটি রিং-ডাউন স্পেক্ট্রোস্কোপিক (CRDS) সাথে একটা কন্টিনিউয়াস ওয়েভ এক্সটার্নাল কেভিটি কোয়ান্টাম ক্যাস্কেড লেজার (cw-EC-CRDS)। সাইট স্পেসিফিক নাইট্রাস অক্সাইড এর বিটা আইসোটোপোমারে (N_2O), i.e. $^{15}N^{14}N^{16}O$ (or $^{15}N^{\beta}$) এই এল টাইপ ডাব্লিং দেখতে পাওয়া যায়। আমরা তার বহু স্পেক্ট্রোস্কোপিক বৈশিষ্ট্য খুঁজে পেয়েছি এবং নির্ধারণ করেছি। মূলত আমরা $(11^10)\leftarrow(01^10)$ এবং $(12^20)\leftarrow(02^20)$ এই ট্রানজিশন গুলোকে ৭.৮ মাইক্রোমিটার মিড আইআর রিজিয়ানে পরীক্ষা করেছি। পরবর্তীতে নাইট্রিক অক্সাইডের (NO) জন্য ল্যামডা টাইপ ডাবলেট বিভাজনের রোটেশনালি রিসলভড ই এবং এফ কম্পনেন্টস যেগুলি $(^2\prod_{1/2} - ^2\prod_{1/2})$ এবং $(^2\prod_{3/2} - ^2\prod_{3/2})$ অ্যালাউড সাব ব্যান্ডের অন্তর্গত, সেগুলিকে আমরা ৫.২ মাইক্রোমিটার মিড ইনফ্রারেড রিজিয়ানে পরীক্ষা করে দেখেছি। এই পরীক্ষার ফলস্বরূপ আমরা বিভিন্ন স্পেক্ট্রোস্কোপিক প্যারামিটারস ক্যালকুলেট এবং বিশ্লেষণ করেছি।

আরেকটি কাজে আমরা ক্যাভিটি এনহ্যান্সড অ্যাবসরপশন স্পেকট্রোস্কোপি (CEAS) ব্যবহার করে সহজ উপায় এবং স্বল্প ব্যয় নাইট্রোজেন ডাই অক্সাইড (NO_2) শনাক্তকরণের উপায় বার করেছি। অপটিক্যাল সোর্স হিসেবে আমরা ৪০৬ ন্যানোমিটার ডায়োড লেজার ব্যবহার করেছি। এই

পদ্ধতির দ্বারা আমরা ন্যূনতম ৩৩০ পিপিবি নাইট্রোজেন ডাই অক্সাইড সনাক্ত করতে সক্ষম। আমাদের এই নির্মিত সেটাপ ব্যবহার করে বিভিন্ন গাড়ির ধোঁয়াতে নাইট্রোজেন ডাই-অক্সাইডের মাত্রা পরীক্ষা করা হয়েছে।

পরবর্তীতে, আমরা সাধারণ উৎস থেকে একই সাথে উষ্চারিত হয়ে আসা কার্বন ডাইঅক্সাইড (CO_2) এবং নাইট্রোজেন ডাইঅক্সাইডের (NO_2) মধ্যে ^{১৬}O- এবং ^{১৮}O- অক্সিজেন আইসোটোপ-এক্সচেঞ্জের সরাসরি পরীক্ষামূলক প্রমাণ প্রদান করেছি। একটি সম্মিলিত নিয়ার-ইনফ্রারেড এবং UV-Vis অপটিক্যাল ক্যাভিটি-এনহ্যান্সড পরীক্ষা এবং কোয়ান্টাম রাসায়নিক হিসেবের পরের পর্যায়ে রিয়েকশন মডেলিং অধ্যয়নের সাথে একটি সমন্বিত প্রায়োজন অনুসন্ধানের মাধ্যমে প্রদান করেছি যে CO_2 এবং NO_2 প্রায় নিকট-ইউ-ভি আলো-চালিত NO_2 ফোটোলাইসিস দ্বারা আইসোটোপিকভাবে যোগাযোগ করতে পারে।

অবশেষে, আমরা একটি অপ্টিক্যাল সিস্টেমের উন্নতি প্রতিবেদন করেছি, যা ৪৫০ ন্যানোমিটার LED ব্যবহার করে ইনকোহারেন্ট ব্রডব্যান্ড ক্যাভিটি-এনহ্যান্সড অ্যাবসরপশন স্পেকট্রোস্কোপির (IBBCEAS) উপর ভিত্তি করে, যাতে গ্যাস পর্যায়ে ডাইএসিটিল মলিকিউল ($C_4H_6O_2$) সঠিক পরিমাপ করা যায়। এই উন্নত সেটআপের সাথে ডাইএসিটিল মলিকিউলের জন্য প্রায় ~ ১৯০ পিপিবি স্বাভাবিক প্রবৃদ্ধি সীমা অর্জন করা হয়েছিল। এই সেন্সর সিস্টেমটি আরও অপটাইমাইজ করা হয়েছিল, ক্যালিব্রেট করা হয়েছিল এবং ডাইএসিটিল স্তর বিভিন্ন দই নমুনা এবং বিয়ারে পরিমাপ করার জন্য প্রদর্শন করা হয়েছিল। এইভাবে, আমরা বিভিন্ন CEAS প্রযুক্তি উন্নত করেছি এবং তাদেরকে ব্যবহার করেছি।

List of publications related to Thesis work

[1] **Ardhendu Pal**, Biswajit Panda, Sanchi Maithani, and Manik Pradhan "Cavity ring-down spectroscopy of *l*-type doubling in ^{15}N-β-site N_2O isotopomer near 7.8 μm." ***Journal of Molecular Spectroscopy*** 381, 111523, (2021).

[2] **Ardhendu Pal**, Biswajit Panda, Sanchi Maithani, and Manik Pradhan "*l*-doublet splittings in Δ vibrational state of $^{15}N^{14}N^{16}O$ isotopomer." ***Chemical Physics Impact*** 3, 100049, (2021).

[3] **Ardhendu Pal**, Soumyadipta Chakraborty, Biswajit Panda, and Manik Pradhan "Elucidating Λ-doublet splittings and rotational quantum number-dependent collisional broadenings in $^2\prod_{1/2}$ and $^2\prod_{3/2}$ spin-split sub-bands of NO at 5.2 μm." ***Journal of Molecular Spectroscopy*** 391, 111719, (2023).

[4] **Ardhendu Pal**, Koushik Mondal, Biswajit Panda, and Manik Pradhan "Development of a compact 406 nm diode laser-based cavity-enhanced spectrometer for high-sensitive detection of NO_2 levels in exhaust gas." ***Laser Physics Letters*** 20(7), 075701, (2023).

[5] Koushik Mondal, **Ardhendu Pal**, Biswajit Panda, and Manik Pradhan "Oxygen-isotope exchange between CO_2 and NO_2 with implications for atmospheric chemistry" (Manuscript submitted) (2023)

[6] "Development of incoherent broadband cavity enhances absorption spectrometer for the precise detection of diacetyl." (Manuscript under preparation) (2024)

List of publications apart from Thesis work

[1] Abhijit Maity, Sanchi Maithani, **Ardhendu Pal**, and Manik Pradhan "Highresolution spectroscopic probing of ortho and para nuclear-spin isomers of heavy water in the gas phase." ***Chemical Physics*** 541, 111041, (2021).

[2] Biswajit Panda, **Ardhendu Pal**, Sanchi Maithani, Abhijit Maity, and Manik Pradhan "Ro-vibrational spectral features and pressure broadening dynamics of dideutero-methane ($^{12}CH_2D_2$) in the ν9 (B2) fundamental band." ***Journal of Molecular Spectroscopy*** 384, 111572, (2022).

[3] Biswajit Panda, **Ardhendu Pal**, and Manik Pradhan "Direct and 2f-wavelength modulation spectroscopy of NO and OCS using an astigmatic multipass cell coupled with a mid-IR 5.2 μm cw-QCL." ***Laser Physics*** 32(3), 035702, (2022).

[4] Biswajit Panda, **Ardhendu Pal**, Soumyadipta Chakraborty, and Manik Pradhan "An EC-QCL based dual-species (CH_4/N_2O) detection method at 7.8 μm in mid-IR region for simultaneous applications of atmospheric monitoring and breath diagnostics." ***Infrared Physics & Technology*** 125, 104261, (2022).

[5] Soumyadipta Chakraborty, **Ardhendu Pal**, Biswajit Panda, Indrayani Patra, and Manik Pradhan "Elucidation of rotational-interaction coupling and collision-induced effects in rovibrational transitions of β-N_2O isotopologue at 7.8 μm mid-infrared region by cavity ring-down spectroscopy." ***Infrared Physics & Technology*** 133, 104752, (2023).

[6] Soumyadipta Chakraborty, **Ardhendu Pal**, Biswajit Panda, Indrayani Patra, and Manik Pradhan "High-resolution rovibrational cavity ring-down spectroscopy of ($12^00 \leftarrow 02^00$) vibrational band of β-site-specific N_2O isotopologue near 7.8 μm region." ***Journal of Chemical Sciences*** 135(4), 113 (2023).

[7] Soumyadipta Chakraborty, Jayeta Banerjee, Indrayani Patra, **Ardhendu Pal**, Puspendu Barik and Manik Pradhan "Anomalous scattering of polystyrene

microparticles by evanescent-wave coupled cavity ring-down spectroscopy". ***Analyst*** (2024)

[8] "Direct probing of allowed and forbidden ortho and para nuclear spin-isomers of NH_3 at 6.2 μm using cavity ring-down spectroscopy." (Manuscript submitted) (2023)

Chapter: 1

Trace molecule sensing: why it is so important?

1.1 Introduction

Trace gases are gases found in limited quantities in a specific environment, like the atmosphere of a planet. Nitrogen gas (78.1 %) is the primary constituent of our earth's atmosphere followed by oxygen gas (20.9 %), argon an inert gas (0.9 %) and remaining 0.1 % is the trace gas [1-3]. Irony is the even though trace gases are found in small amounts in our atmosphere but they are playing a significant roles in various atmospheric phenomenon. So, several researchers are motivated to study theses trace gas molecules to understand missing links still now. Trace gases in atmosphere are composed of numerous inorganic and organic molecules such as methane (CH_4), carbon dioxide (CO_2), acetylene (C_2H_2), ozone (O_3), sulphur dioxide (SO_2), nitrous oxide (N_2O), hydrogen sulphide (H_2S), and oxides of nitrogen (NOx). In spite of their low concentration compared to the whole atmosphere, the balance in their concentration is highly necessary to maintain the atmospheric stability. However, human activities such as the industrial revolution, deforestation, fossils fuels burning and accumulation of waste products in a random manner accelerate the enhancement of the concentration of those trace constituents during the last two centuries rapidly. Further, the exact trace gas concentrations vary from region to region depending on their sources of origin like anthropogenic or biogenic (emission from different natural phenomenon) sources [4,5]. Even many trace molecules and radicals have immense astrophysical significance and their study leads to reveal various interesting processes in interstellar space.

Atmosphere of the earth is a complex mixture of various trace gases, and their measurements play a significant role in chemical and climatic models. Recent advancements in atmospheric science have largely depend on data collected from the atmosphere, especially in understanding how the sun interacts with the

atmospheric constituents, resulting in chemical and radiative changes which in turn have impact on the environmental and climatic change. When it comes to technology, there was a substantial progress in measuring various atmospheric trace components, both through in situ (on-site) and remote sensing techniques, particularly in the lower atmosphere. Trace gases are crucial in understanding climate change and various environmental challenges. Recent developments in both in situ and remote sensing instruments have provided researchers with the capability to study atmospheric processes in intricate detail [6,7].

Detecting trace gases and pollutants in the environment is crucial for ensuring a safe workplace and a healthy surrounding. Furthermore, modern technology demands sensors that are highly portable and possess exceptional detection limits, sensitivity, and selectivity. Gas sensors have come a long way since their traditional use in coal mines, like the Davy lamp in 1816, and are now applied in numerous fields such as controlling outdoor and indoor air quality, industry, upper atmosphere research, security, and detecting volatile organic compounds (VOCs), among other applications [8]. In today's context, state-of-the-art gas sensors must be responsive, safe, easy to operate, portable, cost-effective, and highly selective, capable of identifying target gases even at very low concentrations, measured in parts per billion to million by volume (ppb to ppm), even when surrounded by complex and unknown gas mixtures [9]. Additionally, modern applications require gas sensors to be portable and compatible with the Internet of Things (IoT), making them suitable for both industrial and household use. The performance of a gas sensor is assessed depending on several factors or figures of merit, including sensitivity, selectivity, response time, energy efficiency, reversibility, gas absorption capacity, and manufacturing cost. The choice of analytical techniques is critical in enhancing a sensor's selectivity, particularly when identifying specific gases at low concentrations in diverse environments. Gas sensors must also meet the criteria of stability and reproducibility, which can be affected by factors like design flaws, structural changes, the introduction of foreign contaminants over time, chemical reactions with gases, and alterations in the surrounding conditions. However, while significant efforts have been made to improve the sensitivity of trace gas sensors,

research should focus on enhancing their selectivity, ensuring they have minimal or zero cross-sensitivity to other gases present in the working environment.

1.2 Why trace gas sensing is necessary?

1.2.1 Environmental monitoring

Monitoring trace gases helps in controlling and improving air quality, which directly impacts human health. Elevated levels of certain trace gases, like carbon monoxide (CO) and nitrogen dioxide (NO_2), can lead to serious health issues like respiratory problems and others. Trace gases such as nitrous oxide (N_2O), methane (CH_4), and carbon dioxide (CO_2) are greenhouse gases. Detecting their levels is essential for understanding and mitigating climate change. They are the crucial components causing global warming by trapping heat inside the earth's atmosphere. Measuring trace gases concentration can provide early warnings of environmental hazards. For example, detecting the presence of hydrogen sulphide (H_2S) can prevent accidents and maintain workers' safety in industrial area. Trace gas monitoring is fundamental scientific research area, enabling a better understanding of natural processes, environmental changes, and their consequences. The typical concentrations of some trace gases and their atmospheric importance are depicted in Table 1.1.

Table 1.1: Trace gases concentration and their atmospheric importance. [10-22]

Trace gas	**Concentrations ppbv (10^{-9})**	**Importance**
Nitrous oxide (N_2O)	300-340	Greenhouse gas, causes ozone layer depletion, released from anthropogenic and natural sources.
Nitrogen dioxide (NO_2)	0.01 - 200	Regulates atmospheric chemistry and affect ozone concentrations.
Nitric oxide (NO)	10 - 50	Plays a vital role in atmospheric chemistry as well as acts as biological biomarker.

Methane (CH_4)	1500 - 2000	Greenhouse gas, emitted from fossils fuels.
Acetylene (C_2H_2)	0.5 - 3	Act as gas fuel for welding and cutting process.
Carbon dioxide (CO_2)	350 - 400	Essential for life on earth, primary Greenhouse gas.
Carbon monoxide (CO)	80 - 100	Toxic gas produced from combustion of fossil fuels and biomass.
Ammonia (NH_3)	0.01 - 50	Produced from fertilizer use.
Hydrogen Sulfide (H_2S)	0.11 – 0.33	Acts as mediator of many physiological processes.

1.2.2 Biomedical diagnosis

Trace gas analysis has gained significant importance in biomedical diagnosis. Trace gases monitoring can help in the early detection and diagnosis of several diseases. Typically the human exhaled air contains nearly 2000 trace constituents, out of which most of them are volatile organic compounds (VOC's). For instance, the presence of specific volatile organic compounds (VOCs) in a person's breath can indicate the presence of certain diseases. Trace gas detection in human breath can provide a non-invasive and continuous way to monitor an individual's health condition. Breath analysis can be used to track the patients' health condition suffering with chronic diseases like asthma or chronic obstructive pulmonary disease (COPD). It offers a non-invasive alternative to traditional diagnostic methods which are really painful, reducing patient discomfort and the need for invasive procedures. Monitoring trace gases is crucial for research in areas like drug development, pharmacology, and physiology, enabling a better understanding of metabolic processes and disease mechanisms. Advances in trace gas monitoring technology have led to the development of portable, wearable, and point-of-care

devices, making health monitoring more accessible and convenient. Table 1.2 comprises of trace molecules in exhaled breath and diseases associated with it.

Table 1.2: Trace gases concentration in human breath and linked diseases. [23-36]

Trace gas	**Concentrations in exhaled breath**	**Diseases/ Conditions**
Nitrous oxide (N_2O)	250-350 ppbv	Nitrification and denitrication process in human body
Nitric oxide (NO)	5-60 ppbv	Cystic fibrosis, Asthma
Ammonia (NH_3)	0.05-2 ppmv	Liver cirrhosis, Kidney diseases
Hydrogen sulfide (H_2S)	0.2-2 ppmv	Halitosis, Airway diseases
Carbon dioxide (CO_2) and its isotopes	3-5%	Diabetes mellitus, H. Pylori infection in stomach
Methane ($^{12}CH_4$)	2-10 ppmv	Intestinal diseases, Fermentation by gut microbes

1.2.3 Isotopic analysis

Trace gas monitoring allows for the identification and measurement of specific isotopes in a sample. This is crucial in various fields, including geology, environmental science, and nuclear physics. In archaeology and geology, trace gas monitoring is essential for radiocarbon dating. By measuring the trace amounts of radioactive carbon-14 (^{14}C) in a sample, researchers can estimate the age of organic materials. Trace gas monitoring is used to trace the reaction pathways and sources of isotopes in the environment. This is valuable for understanding processes like groundwater flow, pollutant transport, and nutrient cycling. Isotope analysis of trace gases, such as carbon dioxide ($^{16}O^{12}C^{16}O$, $^{16}O^{12}C^{18}O$, $^{16}O^{13}C^{16}O$), methane ($^{12}CH_4$, $^{13}CH_4$, $^{12}CH_3D$, $^{12}CH_2D_2$), nitrous oxide ($^{14}N^{14}N^{16}O$, $^{15}N^{14}N^{16}O$, $^{14}N^{15}N^{16}O$) and water vapour (H_2O, $^{18}OH^{16}O$, $^{17}OH^{16}O$, HDO, D_2O), provides insights into paleoclimatic

informations, helping scientists reconstruct climatic history and study climatic changes [37-42]. In the food and beverage industry, trace gas monitoring is employed to detect isotopic fraud, ensuring product quality and authenticity, such as verifying the origin of wines or the authenticity of organic products. Isotope analysis of trace gases like water vapour provides insights into the sources of water in hydrological systems hence helping manage water resources and assess groundwater contamination. Many industrial processes require precise control of trace gases and chemicals. Sensors that can detect and monitor trace molecules are crucial for quality control, safety, and process optimization in industries like manufacturing, petrochemicals, and semiconductor fabrication.

1.3 Detection methods of trace gas molecules

As trace gases are available in very low concentrations in the order of parts per billion by volume (ppbv) to parts per trillion by volume (pptv). Therefore, high sensitive and highly selective detection methods are essential to detect those molecules in trace levels. So, over the decades several spectroscopic [43-46] and non-spectroscopic [47,48] techniques have been developed coupled with different coherent and incoherent optical light sources. In this thesis we will find the utilization of high-resolution and ultra-sensitive spectroscopic method for the fundamental spectroscopic study of *l*-type doublet [37,49] in site-specific nitrous oxide molecule and Λ-type doublet [50] in nitric oxide molecule. Development of coherent and incoherent optical source based cavity enhanced absorption spectroscopy (CEAS) technique for the detection of inorganic and organic compounds [51]. Further, the isotopic exchange study between carbon dioxide and nitrogen dioxide molecule to find how these isotopes communicating among them isotopically has been discussed in this thesis.

1.4 References

[1] L. K. Sahu, N. Tripathi, and R. Yadav, "Observations of trace gases in Earth's lower atmosphere: instrumentation and platform." *Current Science*, 118(12), 25 (2020).

[2] C. E. Junge, "Residence time and variability of tropospheric trace gases." *Tellus*, 26(4), 477 (1974).

[3] P. Barik, and M. Pradhan, "Selectivity in trace gas sensing: recent developments, challenges, and future perspectives." *Analyst*, 147(6), 1024 (2022).

[4] S. Prakash, and A. K. Verma, "Anthropogenic activities and Biodiversity threats." *International Journal of Biological Innovations*, 4(1), 94 (2022).

[5] B. Chen, X. Zhang, J. Tao, J. Wu, J. Wang, P. Shi, Y. Zhang, and C. Yu, "The impact of climate change and anthropogenic activities on alpine grassland over the Qinghai-Tibet Plateau." *Agricultural and Forest Meteorology*, 189, 11 (2014).

[6] B. Thomas, A. Miffre, G. David, J. P. Cariou, and P. Rairoux, "Remote sensing of trace gases with optical correlation spectroscopy and lidar: theoretical and numerical approach." *Applied Physics B*, 108, 689 (2012).

[7] B. Deng, C. Sima, Y. Xiao, X. Wang, Y. Ai, T. Li, P. Lu, and D. Liu, "Modified laser scanning technique in wavelength modulation spectroscopy for advanced TDLAS gas sensing." *Optics and Lasers in Engineering*, 151, 106906 (2022).

[8] Y. M. Kim, S. Harrad, and R. M. Harrison, "Concentrations and sources of VOCs in urban domestic and public microenvironments." *Environmental science & technology*, 35(6), 997 (2001).

[9] I. Galli, S. Bartalini, S. Borri, P. Cancio, D. Mazzotti, P. De Natale, and G. Giusfredi, "Molecular gas sensing below parts per trillion: radiocarbon-dioxide optical detection." *Physical Review Letters*, 107(27), 270802 (2011).

[10] O. R. Cooper, D. D. Parrish, J. Ziemke, N. V. Balashov, M. Cupeiro, I. E. Galbally, S. Gilge, L. Horowitz, N. R. Jensen, J. F. Lamarque, and V. Naik, "Global

distribution and trends of tropospheric ozone: An observation-based review." *Elementa*, 2, 000029 (2014).

[11] K. von Bobrutzki, C. F. Braban, D. Famulari, S. K. Jones, T. Blackall, T. E. L. Smith, M. Blom, H. Coe, M. Gallagher, M. Ghalaieny, and M. R. McGillen, "Field inter-comparison of eleven atmospheric ammonia measurement techniques." *Atmospheric Measurement Techniques*, 3(1), 91 (2010).

[12] G. R. Carmichael, M. Ferm, N. Thongboonchoo, J. H. Woo, L. Y. Chan, K. Murano, P. H. Viet, C. Mossberg, R. Bala, J. Boonjawat, and P. Upatum, "Measurements of sulfur dioxide, ozone and ammonia concentrations in Asia, Africa, and South America using passive samplers." *Atmospheric Environment*, 37(9-10), 1293 (2003).

[13] F. Schreiber, P. Wunderlin, K. M. Udert, and G. F. Wells, "Nitric oxide and nitrous oxide turnover in natural and engineered microbial communities: biological pathways, chemical reactions, and novel technologies." *Frontiers in microbiology*, 3, 372 (2012).

[14] S. K. Kharol, R. V. Martin, S. Philip, B. Boys, L. N. Lamsal, M. Jerrett, M. Brauer, D. L. Crouse, C. McLinden, and R. T. Burnett, "Assessment of the magnitude and recent trends in satellite-derived ground-level nitrogen dioxide over North America." *Atmospheric Environment*, 118, 236 (2015).

[15] A. Syakila, and C. Kroeze, "The global nitrous oxide budget revisited." *Greenhouse gas measurement and management*, 1(1), 17 (2011).

[16] A. J. Turner, C. Frankenberg, P. O. Wennberg, and D. J. Jacob, "Ambiguity in the causes for decadal trends in atmospheric methane and hydroxyl." *Proceedings of the National Academy of Sciences*, 114(21), 5367 (2017).

[17] P. J. Crutzen, and H. G. Brauch, eds., Paul J. Crutzen: a pioneer on atmospheric chemistry and climate change in the Anthropocene (Vol. 50). *Springer* (2016).

[18] U. Siegenthaler, and J. L. Sarmiento, "Atmospheric carbon dioxide and the ocean." *Nature*, 365(6442), 119 (1993).

[19] S. N. Behera, M. Sharma, V. P. Aneja, and R. Balasubramanian, "Ammonia in the atmosphere: a review on emission sources, atmospheric chemistry and deposition on terrestrial bodies." *Environmental Science and Pollution Research*, 20, 8092 (2013).

[20] C. A. M. Brenninkmeijer, T. Röckmann, M. Bräunlich, P. Jöckel, and P. Bergamaschi, "Review of progress in isotope studies of atmospheric carbon monoxide." *Chemosphere-Global Change Science*, 1(1-3), 33 (1999).

[21] E. A. Davidson, "Sources of nitric oxide and nitrous oxide following wetting of dry soil." *Soil Science Society of America Journal*, 56(1), 95 (1992).

[22] E. D. Schulze, S. Luyssaert, P. Ciais, A. Freibauer, I. A. Janssens, J. F. Soussana, P. Smith, J. Grace, I. Levin, B. Thiruchittampalam, and M. Heimann,. "Importance of methane and nitrous oxide for Europe's terrestrial greenhouse-gas balance." *Nature geoscience*, 2(12), 842 (2009).

[23] B. P. J. de Lacy Costello, M. Ledochowski, and N. M. Ratcliffe, "The importance of methane breath testing: a review." *Journal of breath research*, 7(2), 024001 (2013).

[24] S. Das, and M. Pal, "Non-invasive monitoring of human health by exhaled breath analysis: A comprehensive review." *Journal of The Electrochemical Society*, 167(3), 037562 (2020).

[25] Y. H. Chen, W. Z. Yao, B. Geng, Y. L. Ding, M. Lu, M. W. Zhao, and C. S. Tang, "Endogenous hydrogen sulfide in patients with COPD." *Chest*, 128(5), 3205 (2005).

[26] J. H. Kim, E. Lin, and M. Pimentel, "Biomarkers of irritable bowel syndrome." *Journal of neurogastroenterology and motility*, 23(1), 20 (2017).

[27] J. M. Escamilla-Gil, M. Fernandez-Nieto, and N. Acevedo, "Understanding the cellular sources of the fractional exhaled nitric oxide (FeNO) and its role as a biomarker of type 2 inflammation in asthma." *BioMed Research International*, (2022).

[28] S. J. Davies, P. Španěl, and D. Smith, "Breath analysis of ammonia, volatile organic compounds and deuterated water vapor in chronic kidney disease and during dialysis." *Bioanalysis*, 6(6), 843 (2014).

[29] T. Hibbard, and A. J. Killard, "Breath ammonia analysis: Clinical application and measurement." *Critical Reviews in Analytical Chemistry*, 41(1), 21 (2011).

[30] K. Syrjänen, M. Eskelinen, A. Peetsalu, T. Sillakivi, P. Sipponen, M. Härkönen, L. Paloheimo, M. Mäki, T. Tiusanen, O. Suovaniemi, and F. DiMARIO, "GastroPanel® biomarker assay: The most comprehensive test for Helicobacter pylori infection and its clinical sequelae. a critical review." *Anticancer Research*, 39(3), 1091 (2019).

[31] M. Pimentel, R. P. Gunsalus, S. S. Rao, and H. Zhang, "Methanogens in human health and disease." *The American Journal of Gastroenterology Supplements*, 1(1), 28 (2012).

[32] D. Feng, L. Du, X. Xing, C. Wang, J. Chen, Z. Zhu, Y. Tian, and D. Yang, "Highly sensitive and selective NiO/WO_3 composite nanoparticles in detecting H_2S biomarker of halitosis." *ACS sensors*, 6(3), 733 (2021).

[33] S. M. Gordon, L. A. Wallace, M. C. Brinkman, P. J. Callahan, and D. V. Kenny, "Volatile organic compounds as breath biomarkers for active and passive smoking." *Environmental health perspectives*, 110(7), 689 (2002).

[34] C. Ghosh, S. Mandal, G. D. Banik, A. Maity, P. Mukhopadhyay, S. Ghosh, and M. Pradhan, "Targeting erythrocyte carbonic anhydrase and ^{18}O-isotope of breath CO2 for sorting out type 1 and type 2 diabetes." *Scientific Reports*, 6(1), 35836 (2016).

[35] F. L. Suarez, J. K. Furne, J. Springfield, and M. D. Levitt, "Morning breath odor: influence of treatments on sulfur gases." *Journal of dental research*, 79(10), 1773-1777 (2000).

[36] F. G. Marcondes-Braga, I. G. Gutz, G. L. Batista, P. H. Saldiva, S. M. Ayub-Ferreira, V. S. Issa, S. Mangini, E. A. Bocchi, and F. Bacal, "Exhaled acetone as a new biomarker of heart failure severity." *Chest*, 142(2), 457 (2012).

[37] A. Pal, B. Panda, S. Maithani, and M. Pradhan, "Cavity ring-down spectroscopy of *l*-type doubling in ^{15}N-β-site N_2O isotopomer near 7.8 μm." *Journal of Molecular Spectroscopy*, 381, 111523 (2021).

[38] B. Panda, A. Pal, S. Maithani, A. Maity, and M. Pradhan, "Ro-vibrational spectral features and pressure broadening dynamics of dideutero-methane ($^{12}CH_2D_2$) in the ν_9 (B2) fundamental band." *Journal of Molecular Spectroscopy*, 384, 111572 (2022).

[39] T. H. Heaton, "Isotopic studies of nitrogen pollution in the hydrosphere and atmosphere: a review." *Chemical Geology: Isotope Geoscience Section*, 59, 87 (1986).

[40] S. Maithani, B. Panda, A. Maity, and M. Pradhan, "Gas-Phase Isotopic Fractionation Study of Singly and Doubly Deuterated Isotopologues of Water in the H–D Exchange Reaction by Cavity Ring-Down Spectroscopy." *The Journal of Physical Chemistry A*, 124(6), 1104 (2020).

[41] B. J. Peterson, and B. Fry, "Stable isotopes in ecosystem studies." *Annual review of ecology and systematics*, 18(1), 293 (1987).

[42] C. A. Brenninkmeijer, C. Janssen, J. Kaiser, T. Röckmann, T. S. Rhee, and S. S. Assonov, "Isotope effects in the chemistry of atmospheric trace compounds." *Chemical Reviews*, 103(12), 5125 (2003).

[43] R. T. Jongma, M. G. Boogaarts, I. Holleman, and G. Meijer, "Trace gas detection with cavity ring down spectroscopy." *Review of scientific instruments*, 66(4), 2821 (1995).

[44] F. J. Harren, G. Cotti, J. Oomens, and S. te Lintel Hekkert, "Photoacoustic spectroscopy in trace gas monitoring." *Encyclopedia of analytical chemistry*, 3, 2203 (2000).

[45] J. Xia, F. Zhu, J. Bounds, E. Aluauee, A. Kolomenskii, Q. Dong, J. He, C. Meadows, S. Zhang, and H. Schuessler, "Spectroscopic trace gas detection in air-

based gas mixtures: Some methods and applications for breath analysis and environmental monitoring." *Journal of Applied Physics*, 131(22) (2022).

[46] K. Song, and E. C. Jung, **"**Recent developments in modulation spectroscopy for trace gas detection using tunable diode lasers.**"** *Applied Spectroscopy Reviews*, *38*(4), 395 (2003).

[47] E. Matisova, and M. Dömötörová, **"**Fast gas chromatography and its use in trace analysis.**"** *Journal of Chromatography A*, 1000(1-2), 199 (2003).

[48] J. De Gouw, C. Warneke, T. Karl, G. Eerdekens, C. Van der Veen, and R. Fall, "Sensitivity and specificity of atmospheric trace gas detection by proton-transfer-reaction mass spectrometry**.**" *International Journal of Mass Spectrometry*, 223, 365 (2003).

[49] A. Pal, B. Panda, S. Maithani, and M. Pradhan, "*l*-doublet splittings in Δ vibrational state of $^{15}N^{14}N^{16}O$ isotopomer.**"** *Chemical Physics Impact*, 3, 100049 (2021).

[50] A. Pal, S. Chakraborty, B. Panda, and M. Pradhan, "Elucidating Λ-doublet splittings and rotational quantum number-dependent collisional broadenings in $^2\prod_{1/2}$ and $^2\prod_{3/2}$ spin-split sub-bands of NO at 5.2 μm." *Journal of Molecular Spectroscopy*, 391, 111719 (2023).

[51] A. Pal, K. Mondal, B. Panda, and M. Pradhan, "Development of a compact 406 nm diode laser-based cavity-enhanced spectrometer for high-sensitive detection of NO_2 levels in exhaust gas." *Laser Physics Letters*, 20(7), 075701 (2023).

Chapter: 2

Coherent and incoherent optical sources

2.1 Introduction

Light is an essential part of live. We know light is an electromagnetic wave which is a fundamental entity in the field of photonics [1,2]. It can be classified on the basis of frequencies, wavelength, and intensity. Photons constitute light waves, which exhibit distinct attributes such as phase, amplitude, frequency, and period. [3-5]. When it comes to optical light sources, they can be broadly categorized into two types: coherent and incoherent. These classifications are based on the behaviour of the light waves they emit, particularly in terms of their phase relationship [6-9]. Understanding the differences between these two types of light sources is very crucial for various applications in optics like laser technology, spectroscopy, imaging and communication.

2.2 Coherent light source

Coherent light sources are characterized by the emission of light waves with a well-defined phase relationship. In other words, the peaks and troughs of the individual waves are synchronized, maintaining a constant phase difference between them. This coherence is a result of the underlying physics of the light generation process. Important features of light emitted from these coherent sources are as follows: Coherent light sources emit light at a specific well-defined frequency. This monochromatic property is one of the defining characteristics of coherent light. Coherent light sources produce highly directional beams of light. When two coherent light beams of the same frequency intersect, they can produce interference patterns, which can be observed as alternating regions of constructive and destructive interference. This property is often exploited in applications like interferometry and holography. Coherent light sources exhibit both temporal and

spatial coherence. Temporal coherence refers to the synchronization of waves at different points in same time, while spatial coherence pertains to the synchronization of waves at different points in space. Few examples of coherent optical sources are He-Ne laser, diode laser, quantum cascade laser (QCL) etc.

2.2.1 Diode Laser

Diode laser is specifically fabricated p-n junction diode which emits laser light when subjected to forward bias [10-16]. In a forward-biased state, this diode enables the movement of electrons from the n-region and holes from the p-region across the junction, leading to their recombination. During the recombination process, photons of light are released from certain direct band gap semiconductors, such as Ga-As. This released light is known as recombination radiation. The emitted photons, during recombination, stimulate other electrons and holes to recombine as well. This results in stimulated emission, which is responsible for lasing action. The application of a substantial forward bias voltage to the PN junction results in the injection of a significant concentration of electrons and holes into the junction region. Near the junction, a notable population of electrons resides in the conduction band, accompanied by a substantial number of holes in the valence band. When the population density becomes high, it leads to a state of population inversion. In this condition, electrons and holes readily recombine, producing radiation in the form of light. With an increase in the forward-biased voltage gradually, more light photons are emitted, intensifying the light coming out of the diode laser. These photons, in turn, initiate a chain reaction of stimulated recombination, resulting in the emission of coherent photons. In this thesis we have utilized diode laser operating at 406 nm wavelength region for the trace detection of nitrogen dioxide molecule.

2.2.2 Quantum cascade laser

The fundamental principle behind LASER (Light Amplification by Stimulated Emission of Radiation) is rooted in the concept of stimulated emission of photons, leading to the generation of coherent radiation. Laser radiation demonstrates exceptional temporal and spatial coherence, as well as high spectral power densities,

offering significant advantages in a wide range of spectroscopic techniques. However, a crucial requirement for achieving lasing action is the establishment of population inversion within the electronic states of the active medium, coupled with effective optical feedback provided by a resonator. Conventional semiconductor lasers adhere to this principle by producing wavelength-dependent radiation through inter-band transitions, which involve radiative recombination between electrons in the conduction band and holes in the valence band. Different materials possess distinct bandgap energies, resulting in varied emission wavelengths. Conversely, in the case of Quantum Cascade Lasers (QCLs), emission is accomplished by harnessing intersubband transitions of a single type of charge carrier, which is an electron [17-23]. Therefore, QCLs are referred to as unipolar laser sources, and their lasing principle significantly deviates from conventional bipolar semiconductor lasers.

QCLs differ from diode lasers both in terms of their structure and mechanism. Diode lasers rely on the interband transition of electrons to produce photons, while QCLs exploit intersubband transitions in thin semiconductor layers. The fundamental mechanism of photon generation in a QCL involves arrangement of alternating thin semiconductor layers acting as quantum wells. When an appropriate electric field bias is applied, electron transitions occur between these subbands, resulting in the emission of photons. Subsequently, electrons tunnel through barriers to reach other subbands, undergoing further transitions, and generating additional photons. This process continues, creating a cascade of photon output. One of the notable advantages of QCLs is their capacity to produce different output wavelengths by varying the thickness of semiconductor layers. Consequently, the same semiconductor materials can yield different wavelengths by simply adjusting the thickness of these layers.

Some important features of QCL are wide tuning range, can operate at room temperature and have impressively high output power. It has extremely narrow line width and provides access to mid-IR figure print region. This recent advancement of QCL enabled the researcher to couple this QCL with different techniques to pursue high-resolution spectroscopic study of various trace gas molecules. In this thesis, we

have coupled high-resolution cavity ring-down spectroscopy (CRDS) with QCL to explore the fundamental spectroscopic parameters of site specific nitrous oxide isotope.

2.3 Incoherent light source

Incoherent light sources, in contrast, emit light waves with random or uncorrelated phases. The individual waves lack synchronization in the alignment of their peaks and troughs, and there is no consistent phase relationship between them. This incoherence is a characteristic of many common light sources. Some characteristics of this incoherent light source are as follows: Light emitted from incoherent sources spans a spectrum of frequencies. They are not limited to a single wavelength, making them suitable for various applications where a broad spectrum of light is needed. Incoherent light sources emit light in multiple directions. There is no well-defined direction for the emitted light, making it suitable for illumination purposes. When two incoherent light beams intersect, they do not produce well-defined interference patterns. The random phase relationship results in a lack of coherent interference effects. Incoherent sources may exhibit partial spatial and temporal coherence, but these characteristics are not as pronounced as in coherent sources. Natural sun light, LED, tungsten filament, light bulb etc. are some examples of incoherent light source.

2.3.1 Light-Emitting Diodes

Light-Emitting Diodes (LED) are electronic devices based on solid-state technology that produce light upon the passage of an electric current [24-29]. They are widely used for various applications, including displays, indicators, lighting, and optical communication. The operation of LEDs is based on a fundamental principle known as electroluminescence. LEDs are typically constructed using semiconductor materials. The most common semiconductor materials used in LEDs are gallium arsenide (GaAs), gallium nitride (GaN), and others. The wavelength or color, of the emitted light is dictated by the choice of material. Within an LED, there exists a p-n junction characterized by an abundance of holes in the p region and an excess of

electrons introduced through doping in the n region. Applying a forward bias voltage across the p-n junction, with the p-side connected to the positive terminal and the n-side to the negative terminal of a power supply, results in the injection of electrons from the n-side into the p-side. Subsequently, these electrons combine with the available holes in the p-side. The process of recombination liberates energy in the form of photons, manifesting as light emission. The energy emitted by photons is determined by the energy band gap of the semiconductor material. The energy associated with the emitted photons corresponds to the difference in energy levels between electrons in the conduction band and holes in the valence band. This is responsible for the specific color of light produced. The semiconductor material properties dictate the wavelength of the emitted light, which can cover a wide spectrum, from ultraviolet (UV) to infrared (IR). LEDs are highly efficient light sources because nearly all of the input electrical energy is converted into light. In this thesis, we have developed a cavity enhanced absorption spectroscopy (CEAS) setup using an incoherent LED light source for the trace detection of organic molecule.

2.4 References

[1] L.A. Weinstein, "Electromagnetic waves" *Radio i svyaz', Moscow, (*1988).

[2] J. A. Polo Jr, and A. Lakhtakia, "Surface electromagnetic waves: a review." *Laser & Photonics Reviews*, 5(2), 234 (2011).

[3] C. Mead, "The nature of light: what are photons**?"** *SPIE,* 8832, 15 (2013).

[4] D. Baylor, "How photons start vision." *Proceedings of the National Academy of Sciences*, 93(2), 560 (1996).

[5] D. E. Godar, "Light and death: photons and apoptosis." *Journal of Investigative Dermatology Symposium Proceedings,* 4(1), 17 (1999).

[6] D. Psaltis, "Coherent optical information systems." *science*, 298(5597), 1359 (2002).

[7] M. Song, V. Torres-Company, and A. M. Weiner, "Noise comparison of RF photonic filters based on coherent and incoherent multiwavelength sources." *IEEE Photonics Technology Letters*, 24(14), 1236 (2012).

[8] S. H. Zhang, L. Gao, J. Xiong, L. J. Feng, D. Z. Cao, and K. Wang, "Spatial interference: From coherent to incoherent." *Physical review letters*, 102(7), 073904 (2009).

[9] S. Ayotte, and L. A. Rusch, "Experimental comparison of coherent versus incoherent sources in a four-user/spl lambda/-t OCDMA system at 1.25 Gb/s." *IEEE photonics technology letters*, 17(11), 2493 (2005).

[10] R. L. Byer, "Diode laser—pumped solid-state lasers." *Science*, 239(4841), 742 (1988).

[11] H. Nasim, and Y. Jamil, "Diode lasers: From laboratory to industry." *Optics & Laser Technology*, 56, 211 (2014).

[12] L. Li, "The advances and characteristics of high-power diode laser materials processing." *Optics and lasers in engineering*, 34(4-6), 231 (2000).

[13] J. C. Camparo, "The diode laser in atomic physics." *Contemporary Physics*, 26(5), 443 (1985).

[14] M. Sciamanna, and K. A. Shore, "Physics and applications of laser diode chaos." *Nature photonics*, 9(3), 151 (2015).

[15] A. Müller, S. Marschall, O. B. Jensen, J. Fricke, H. Wenzel, B. Sumpf, and P. E. Andersen, "Diode laser based light sources for biomedical applications." *Laser & Photonics Reviews*, 7(5), 605 (2013).

[16] F. G. Bachmann, "High-power diode laser technology and applications." *High-Power Lasers in Manufacturing*, 3888, 394 (2000).

[17] S. Maithani, A. Maity, and M. Pradhan, "Quantum cascade laser spectroscopy for atmospheric sensing and biomedical diagnostics." *Advances in Spectroscopy: Molecules to Materials: Proceedings of NCASMM 2018*, *Springer Singapore,* 67 (2019).

[18] M. Pal, and M. Pradhan, "Quantum Cascade Laser Spectroscopy." *Modern Techniques of Spectroscopy: Basics, Instrumentation, and Applications*, 363 (2021).

[19] J. Faist, F. Capasso, D. L. Sivco, C. Sirtori, A. L. Hutchinson, and A. Y. Cho, "Quantum cascade laser." *Science*, 264(5158), 553 (1994).

[20] C. Gmachl, F. Capasso, D. L. Sivco, and A. Y. Cho, "Recent progress in quantum cascade lasers and applications." *Reports on progress in physics*, 64(11), 1533 (2001).

[21] M. S. Vitiello, G. Scalari, B. Williams, and P. De Natale, "Quantum cascade lasers: 20 years of challenges." *Optics express*, 23(4), 5167 (2015).

[22] F. Capasso, C. Gmachl, R. Paiella, A. Tredicucci, A. L. Hutchinson, D. L. Sivco, J. N. Baillargeon, A. Y. Cho, and H. C. Liu, "New frontiers in quantum cascade lasers and applications." *IEEE Journal of selected topics in quantum electronics*, 6(6), 931 (2000).

[23] A. Hugi, R. Maulini, and J. Faist, "External cavity quantum cascade laser." *Semiconductor Science and Technology*, 25(8), 083001 (2010).

[24] S. Pimputkar, J. S. Speck, S. P. DenBaars, and S. Nakamura, "Prospects for LED lighting." *Nature photonics*, 3(4), 180 (2009).

[25] N. Zheludev, "The life and times of the LED—a 100-year history." *Nature photonics*, 1(4), 189 (2007).

[26] E. F. Schubert, "Light-Emitting Diodes" (2018).

[27] C. M. Bourget, "An introduction to light-emitting diodes." *HortScience*, 43(7), 1944 (2008).

[28] G. B. Nair, and S. J. Dhoble, "A perspective perception on the applications of light-emitting diodes." *Luminescence*, 30(8), 1167 (2015).

[29] N. G. Yeh, C. H. Wu, and T. C. Cheng, "Light-emitting diodes—their potential in biomedical applications." *Renewable and Sustainable Energy Reviews*, 14(8), 2161 (2010).

Chapter: 3

Fundamental aspects of spectroscopy

3.1 Introduction

Spectroscopy is an efficient scientific technique that allows us to study the interaction of matter with electromagnetic radiation. It encompasses a wide range of methods for studying the interaction of light with matter, offering valuable insights into the composition, structure, and behaviour of atoms, molecules, and materials. Fundamental spectroscopy [1-4] serves as the foundational framework upon which the diverse branches of spectroscopic analysis are developed. Extending across a broad spectrum, electromagnetic radiation encompasses radio waves characterized by long wavelengths to gamma rays with exceedingly short wavelengths. Spectroscopy involves the study of how matter interacts with this entire spectrum, but it most commonly focuses on regions such as the visible, ultraviolet, infrared, and microwave. When matter interacts with electromagnetic radiation, it can either absorb or emit energy. Absorption occurs when a material absorbs specific wavelengths of light, leading to the excitation of its electrons or other energy transitions. Emission, on the other hand, results in the release of energy in the form of light as electrons transition back to lower energy states. This emission can be of two types spontaneous and stimulated. In atoms and molecules, electrons exist in discrete energy levels or orbitals. Spectroscopy is concerned with transitions between these energy levels. For example, electronic transitions involve changes in the energy levels of electrons, leading to absorption or emission of light in the UV and visible regions. Spectroscopy deals with the measurement of the wavelength (λ) and frequency (ν) of electromagnetic radiation. These two properties are inversely related through the speed of light (c) as $\lambda\nu = c$. Wavelength determines the color or type of radiation, while frequency relates to its energy. Spectroscopic techniques often result in the generation of spectral lines or bands. These are specific, discrete

lines in a spectrum that correspond to the wavelengths of absorbed or emitted light. Spectral lines are characteristic of the material and transitions involved, making them valuable for identifying substances. Spectroscopy encompasses various techniques, each tailored to investigate specific properties of matter. Common types include X-ray spectroscopy, Nuclear Magnetic Resonance (NMR) spectroscopy, UV-Visible spectroscopy, and Infrared spectroscopy, among others [5-9]. Absorption spectroscopy employs the Beer-Lambert law, establishing a connection between the concentration of an absorbing substance, the path length of the sample, and the material's absorbance. This relationship is fundamental for quantitative analysis. Spectroscopy finds applications in various fields, including chemistry, physics, astronomy, biology, environmental science, and materials science. It is used for identifying substances, quantifying their concentrations, probing molecular structures, and monitoring chemical reactions.

This thesis is focused on the implementations and development of spectroscopic techniques for trace gas sensing in vehicular exhaust and kinetic study. This thesis contains a range of spectroscopic techniques, including mid-infrared quantum cascade lasers, diode lasers, and light-emitting diodes (LEDs). Hence, the objective of this chapter is to provide an introduction to infrared spectroscopy and explore various spectroscopic approaches for monitoring trace gases.

3.2 Infrared absorption spectroscopy

In the infrared (IR) spectral region, molecules experience vibrational transitions, giving rise to absorption spectra characterized by numerous closely spaced components (usually ≤ 10 cm^{-1}). These components originate from rotational transitions linked to each vibrational excitation. Individual spectral line possesses a specific linewidth and shape, influenced by the temperature and the molecular environment. This section briefly discusses the spectroscopic transitions occurring in the infrared fingerprint region between vibrational, rotational, and rotational-vibrational (ro-vibrational) states.

3.2.1 Vibrational spectroscopy

Molecular vibration is manifested when the atoms within a molecule undergo either stretching or bending of bonds in response to exposure to electromagnetic (EM) radiation. This displacement among the atoms results in a change in dipole moment, facilitating transitions between quantized vibrational energy levels. Such vibrations are considered IR-active. Significantly, IR-active transitions take place during alterations in the dipole moment, whether along the symmetry axis or perpendicular to it. This stands in contrast to molecules with a permanent dipole moment. Therefore, heteronuclear diatomic molecules like NaCl, KBr, or OH exhibit differences in atomic polarizabilities, leading to a non-zero permanent dipole moment and its magnitude changes during bond stretching. In contrast, homonuclear diatomic molecules such as H_2 and N_2 are deemed infrared inactive since there is no probability of change in the dipole moment to occure.

In the case of polyatomic molecules, the complexity increases, as the motion of individual atoms can be analysed in terms of components along the three axes of a Cartesian coordinate system. Consequently, a molecule comprising N atoms exhibits a total of 3N degrees of freedom, covering vibrational, translational, and rotational motions. For a polyatomic linear molecule containing N atoms, the degrees of freedom can be represented by 3N-5 (or 3N-6 for a non-linear molecule), offering a characterization of the molecule's vibrational modes. For example, nitrous oxide (N_2O), having 3 atoms, comprises of degrees of freedom 3N-5 = 4 (being a linear molecule), which means it has 4 normal modes of vibration as depicted in Figure 3.1. Each vibrational mode quantum number is specified in normal mode notation; ν_1 and ν_3 represent the symmetric and asymmetric stretching, respectively. ν_2 represent the doubly degenerate bending modes leading to 4 vibrational degrees of freedom in total from 3 vibrational modes. All the three vibrational modes of nitrous oxide are IR-active leading to IR absorption in the mid-IR region.

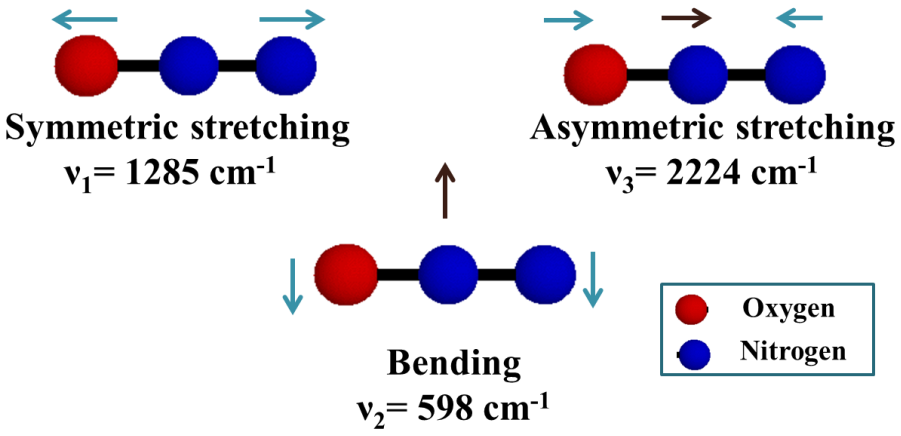

Figure 3.1: *Different vibrational modes of nitrous oxide molecule.*

These vibrational modes can be defined as the combinational displacement of individual atoms and can be assumed to behave as a simple harmonic oscillator (SHO). The well-known Schrödinger equation can be employed to evaluate the permitted vibrational energy levels E_v. Solving the equation the quantised value of energy is obtained as follows:

$$E_v = \left(v + \frac{1}{2}\right) h\nu \qquad v = 0, 1, 2, 3, 4 \ldots\ldots\ldots\ldots \tag{3.1}$$

where, h is Planck's constant, v is the vibrational quantum number, ν is the oscillation frequency of the molecule and is given by:

$$\nu = \frac{1}{2\pi}\sqrt{\frac{k}{\mu}} \tag{3.2}$$

where, k is the bond force constant and μ is the reduced mass of the molecule.

This bond force constant is related to potential energy function which is parabolic in nature.

$$V(r) = \frac{1}{2}kx^2 \tag{3.3}$$

x is defined as the difference between the internuclear and the equilibrium separation of the bond.

$$x = r - r_e \tag{3.4}$$

In spectroscopic units (cm^{-1}) vibrational terms are expressed as;

$$G(v) = \frac{E_v}{hc} = (v + \frac{1}{2})\bar{\nu} \quad \textbf{(3.5)}$$

$$\bar{\nu} = \frac{1}{2\pi c}\sqrt{\frac{k}{\mu}} \quad \textbf{(3.6)}$$

The vibrational selection rule for a simple harmonic oscillator is $\Delta v = \pm 1$. The derivation of this selection rule originates from the properties of the harmonic oscillator wave function, and under this condition, the primary vibrational transition ($1 \leftarrow 0$) takes precedence. Two successive vibrational energy levels are separated by $E_{v \leftarrow v+1} = h\omega$ and therefore adjacent levels are equally spaced.

In real situation the vibrating motion of the atoms are not exactly simple harmonic. The motion becomes anharmonic and the restoring force is no more directly proportional to the displacement of the atoms. Morse potential function is the simplest representation of this anharmonic effect:

$$V(r) = D_e[1 - e^{-a(r-r_e)}]^2 \quad \textbf{(3.7)}$$

where, D_e is the dissociation energy and a is a constant for a particular molecule.

In the presence of anharmonicity the available vibrational energy levels are described by the following expression:

$$E_v = \left(v + \frac{1}{2}\right)h\nu - (v + \frac{1}{2})^2 x_e h\nu \quad \textbf{(3.8)}$$

The parameter x_e is called the anharmonicity constant. For an anharmonic oscillator the selection rules are as follows:

$$\Delta v = \pm 1, \pm 2, \pm 3, \pm 4, \ldots\ldots$$

Due to the presence of anharmonicity vibrational energy level converges and this is the cause for the appearance of weaker overtone transitions ($2 \leftarrow 0$, $3 \leftarrow 0$, $4 \leftarrow 0$, …….) that are forbidden by the selection rule $\Delta v = \pm 1$. However, still now we have considered that each vibration is independent and unaffected by others. When the restriction to simple harmonic behaviour is lifted, then selection rules permit

combination bands and overtone transitions. These arise when the two or more fundamental or overtone transitions excite simultaneously.

3.2.2 Rotational spectroscopy

Inside each vibrational energy level, there are numerous closely spaced rotational lines, forming a dense array. The stack of rotational lines is a result of the interaction between the dipole moment of the rotating molecule and the oscillating electric field of incident infrared light. Rotational transitions necessitate the existence of a permanent electric dipole moment in the molecule, experiencing periodic changes as the molecule rotates around its centre of gravity. Rotational spectroscopy provides significant insights into a molecule's bond angle and bond length. This information is extracted through pure rotational transitions observed in the electromagnetic spectrum, specifically in the microwave region. The energy levels of rotational motion for linear polyatomic molecules and spherical rotors, excluding centrifugal distortion, are expressed as:

$$E_J = BJ(J+1) \quad \textbf{(3.9)}$$

Where, $B = \frac{\hbar}{8\pi^2 IC}$, J (=0,1,2,3….) is the angular momentum quantum number, B is the rotational constant, which depends on the moment of inertia (I) with respect to a particular axis.

The selection rule governing rotational transitions is expressed as ΔJ = ±1. Where $\Delta J = +1$ corresponds to the absorption of a photon and $\Delta J = -1$ corresponds to emission of a photon. The rotational lines are equally spaced with adjacent rotational levels are separated by 2BJ.

In a real scenario, when a molecule begins to rotate under the influence of electromagnetic (EM) radiation, the interatomic distance within the molecule increases due to centrifugal force. Consequently, the moment of inertia experiences an increment, leading to a gradual reduction in the spacing between two consecutive

rotational energy levels as the quantum number J increases. Therefore, taking into account the distortion effect the rotational energy can be expressed with centrifugal distortion term $D_j \mathrm{J}(\mathrm{J}+1)^{2}$ in equation 3.10, where D_j is the centrifugal distortion constant.

$$E_J = BJ(J+1) - D_j \mathrm{J}(\mathrm{J}+1)^2 \quad \textbf{(3.10)}$$

3.2.3 Ro-vibrational spectroscopy

In the ro-vibrational spectroscopy the fine structure of the vibrational band are analysed. This fine structure emerges from rotational transitions coupled with vibrational excitations. In practical terms, a molecule can undergo multiple vibrations within a single rotation period, given that the vibrational frequency significantly surpasses the rotational frequency (typically by one to two orders of magnitude). Utilizing the Born-Oppenheimer approximation, the ro-vibrational energy can be represented as the sum of the distinct energies linked to vibrational and rotational motions. Therefore, the ro-vibrational energy can be expresed, ignoring centrifugal distortion and anharmonicity as follows:

$$E_{total} = E_{rot} + E_{vib} \quad \textbf{(3.11)}$$

$$E_{total} = \left(v + \frac{1}{2}\right)\bar{\nu} + BJ(J+1) \quad \textbf{(3.12)}$$

Ro-vibrational transition having the selection rules which is same for individual component separately, i.e $\Delta J = \pm 1$ and $\Delta v = \pm 1$. The difference in energy between a rotational level within the first vibrational state (v = 1, J') and a rotational level in the ground vibrational state (v = 0, J") can be expressed through the following equations:

$$\Delta E = E_{v=1,J'} - E_{v=0,J''} \quad \textbf{(3.13)}$$

$$\Delta E = \bar{\nu} + 2hB(J''+1), \text{ for } \Delta J = +1, \quad J' = J'' + 1 \quad \textbf{(3.14)}$$

$$\Delta E = \bar{\nu} - 2hB(J''+1), \text{ for } \Delta J = -1, J'' = J' + 1 \quad \textbf{(3.15)}$$

We can combine and write the above two equation as:

$\Delta E = \bar{\nu} + 2Bm$ m= ±1, ±2, ±3, ±4 ……. **(3.16)**

In the combined ro-vibrational spectrum, the lines to the high frequency side of the band centre are denoted as R-branch ($\Delta J = +1$), whereas the lines to the low frequency side of the band centre are signified as P-branch ($\Delta J = -1$). Further, when the angular momentum becomes perpendicular to the major axis of rotational symmetry then ro-vibrational transition with $\Delta J = 0$ is also allowed. Thus, this selection rule results in the emergence of a Q-branch characterized by an energy gap $\Delta E = \bar{\nu}$.

When the anharmonicity is taken into account the rotational constant B is no longer considered to be the constant for different vibrational levels. Consequently, Born-oppenheimar approximation regarding energy separation breaks down. Hence, the rotational constant can be expressed as:

$$B_v = B_e - \alpha\left(v + \frac{1}{2}\right) \quad \textbf{(3.17)}$$

Where, $B_e$is the rotational constant for equilibrium bond length and α denotes the vibrational-rotation coupling constant, which has a positive value for most of the molecule.

For this situation considered above, the energy of the transition can be described by:

$$\Delta E = \bar{\upsilon}_0 + (B_1 + B_0)m + (B_1 - B_0)m^2 \quad \textbf{(3.18)}$$

Where, $B_1$and B_0 indicate the upper and the lower rotational constant, respectively.

It is crucial to note that in the absence of anharmonicity effects, the spectra resulting from ro-vibrational transitions exhibit symmetry about the origin, and the frequency spacing between two rotational lines of a specific vibrational transition is precisely 2B. However, when anharmonicity is present, asymmetrical spectra emerge. In the presence of anharmonicity, the R-branch lines draw closer with increasing quantum number m, while the P-branch lines become more widely spaced with an increase in the quantum number m. Figure 3.2 shows the HITRAN simulation of the ro-vibrational absorption bands of nitrous oxide isotopes in mid-infrared region. It also demonstrates the capability of ro-vibrational spectroscopy to distinguish between

the isotopes of a molecule. HITRAN (high-resolution transmission) is a simulated spectroscopic database of trace molecules in the atmosphere [10].

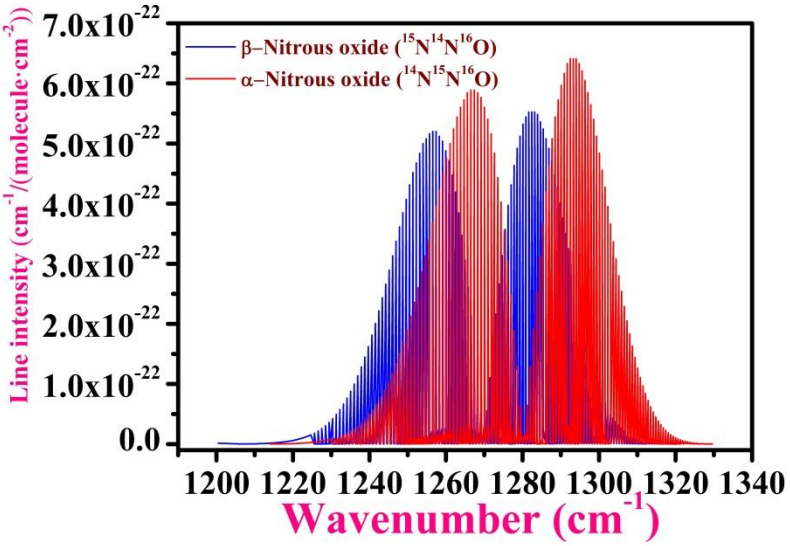

Figure 3.2: *HITRAN simulated ro-vibrational transitions for alpha and beta nitrous oxide.*

3.3 Spectral line width

The consistent presence of a definite width in spectral lines provides valuable information about both the energy levels and the surrounding environment of the specific molecule. The broadening of spectral lines is influenced by several factors, and the extent to which these factors contribute to overall spectral broadening is determined by the experimental conditions. Doppler broadening, arising from the Doppler shift wherein the frequency of radiation undergoes changes as the source moves either toward or away from the observer, constitutes a primary source of spectral broadening. The observed spectral profile shows the Maxwell-Boltzmann distribution of molecular velocities parallel to the line of sight. Doppler broadening can be expressed as Gaussian line shape function with full-width half maximum (FWHM):

$$\Delta\nu_{FWHM} = \frac{2\nu_0}{c}\left(\frac{2kT}{m}\ln 2\right)^{\frac{1}{2}} \quad \textbf{(3.19)}$$

where, ν_0 is the transition frequency, m is the mass of the molecule, c is the speed of light, k is the Boltzmann constant and T is the temperature. The aforementioned expression leads to the conclusion that Doppler broadening escalates with increasing sample temperature, as molecules exhibit a broader range of speeds at higher temperatures. In contrast, lower temperatures result in narrower spectral lines due to the constrained speed range of molecules.

Another source of spectral broadening originates from the lifetime of the transition which is known as lifetime broadening. This can be explained by the very well-known quantum mechanical effect i.e. Heisenberg uncertainty principle. In accordance with this principle, if the lifetime of a system in a specific state is denoted by τ, then the energy levels of that state will be uncertain by an extent of ΔE.

$$\Delta E \approx \frac{h}{\tau} \quad \textbf{(3.20)}$$

Since, no excited state possesses an infinite lifetime, spectral transition lines consistently display a certain width. Even at low temperatures, residual broadening persists due to this inherent characteristic.

Pressure deactivation and spontaneous emission are among the notable factors that significantly influence the finite lifetime of a state. When pressures rise above 50-100 Torr, collisional deactivation becomes possible, resulting in pressure broadening. This phenomenon results in line shapes characterized by Lorentzian profiles. Collisions induce transient interactions among colliding molecules, perturbing their energy levels and causing additional broadening and frequency shifts in spectral lines. The rate of spontaneous emission depends on the transition frequency. Hence, the 'natural width' of the spectral line is affected by the particular region of the electromagnetic spectrum used for measurement. Lorentzian line shape profiles emerge from the broadening caused by the 'natural' lifetime, contributing to the overall width of the spectral lines. It is essential to emphasize that when the broadening of an individual line profile is influenced by both Doppler and Lorentzian broadening; fitting the spectral line appropriately requires a Voigt

profile. This profile results from the convolution of a Gaussian line shape with a Lorentzian line shape.

3.4 Overview of techniques for trace gas analysis

Over the past few years, laser-based trace gas sensing has garnered considerable interest in various fields. This technique finds applications in various fields like chemical analysis for industrial process control, pollution monitoring, medical diagnostics through exhaled breath analysis, industrial emission measurement and also contributing to advancements in homeland security. Across the decades, the growing importance of identifying and quantifying individual trace molecules, along with their stable isotopologues has prompted the development of various non-spectroscopic and spectroscopic detection methods dedicated to monitoring trace molecules.

A range of versatile spectroscopic methods is available for tracking the concentrations and diverse spectroscopic properties of trace molecules. Cavity ring-down spectroscopy (CRDS), Tunable diode laser absorption spectroscopy (TDLAS), Wavelength modulation spectroscopy (WMS), Incoherent broadband cavity enhanced spectroscopy (IBBCEAS), Differential optical absorption spectroscopy (DOAS), Photo acoustic spectroscopy (PAS), and Fourier transform infrared spectroscopy (FTIR) are widely utilized spectroscopic techniques for the measurements of various trace molecules. This section provides a concise overview of the gas detection techniques mentioned above.

3.4.1 Tunable diode laser absorption spectroscopy

Tunable Diode Laser Absorption Spectroscopy (TDLAS) is one of the most common spectroscopic technique for analyzing trace gas properties and constituents, including concentration, temperature, pressure, and flow velocity. It was pioneered in 1970 by E D Hinkley [11]. TDLAS measures the wavelength-dependent

absorption of light as it passes through a sample medium. Utilizing a diode laser with tunable-wavelength characteristics as the light source, this approach identifies variations in light intensity when the laser wavelength aligns with an absorption line of a gas species within the sample. For the sample containing extremely low concentrations of probing gas the change in transmission intensity is very small and becomes challenging to detect. To overcome this limitation, TDLAS sensitivity is significantly augmented by modulating the current of the laser. This modulation, affecting both wavelength and light intensity, allows for enhanced detection. The absorption response information is retrieved by demodulating the signal from the photodetector at both the modulating frequency and its second-order harmonic. Consequently, TDLAS proves invaluable for high-sensitivity measurements, finding applications in diverse fields such as industrial processes, environmental monitoring, and scientific research [12-16].

3.4.2 Photo acoustic spectroscopy

Photo-acoustic spectroscopy (PAS) is another spectroscopic approach to capture absorption spectra in gases and condensed media. In PAS, this is accomplished by detecting acoustic vibrations induced in an analyzed sample through modulated optical radiation. The technique hinges on converting the initial optically induced excitation (rotational, vibrational, electronic, excitation of optical phonons, etc.) into heat, leading to the thermal expansion of the irradiated volume. The resultant pressure changes are then detected by a sound transducer. The roots of PAS can be traced back to the works of A.G. Bell, though his initial intentions did not involve applying optical sound generation for chemical analysis [17-18]. Instead, he visualised its potential for free-space communication. In earlier studies of PAS, the technique was termed 'opto-acoustic spectroscopy,' while the term 'photo-acoustic' was reserved for phenomena related to optically generated phonons in crystals. Photo-acoustic (PA) detection finds application in analyzing various media, including solids, liquids, biological tissues, and gases. Its versatility extends to tasks such as identifying spot defects in optical materials, conducting microscopy on

biological tissues, determining dye concentrations in the textile industry, and analyzing trace gases [19-23].

3.4.3 Cavity ring-down spectroscopy

O'Keefe and Deacon introduced Cavity Ring-Down Spectroscopy (CRDS) in 1988, which stands as a state-of-the-art, ultra-high sensitivity direct absorption technique [24]. This method enables cavity-enhanced absorption measurements of weakly absorbing species with extremely low concentrations. CRDS leverages the concept of a stable optical resonator to achieve an effective optical path length of several kilometers within a compact physical sample length. Furthermore, CRDS boasts several distinct advantages over existing spectroscopic techniques: In CRDS, signal detection occurs in the time domain, rendering the technique immune to intensity fluctuations of the optical source; CRDS provides an effective absorption path length of several kilometers through the sample; The technique ensures limiting sensitivity in the orders of 10^{-8} to 10^{-10} cm^{-1} with high temporal and spatial resolution; No secondary calibration is required; This versatile technique is well-suited for detecting gas-phase atoms, molecules, and radicals; The instrumentation associated with the technique is compact and robust [25-29].

3.4.4 Incoherent broadband cavity enhanced spectroscopy

Introduced in 2003, the IBBCEAS technique is theoretically straightforward and demonstrates exceptional sensitivity in trace gas detection [30]. In this approach, the detection involves capturing the output light from a stable optical cavity, where the input light is sourced from an incoherent broadband light source. In IBBCEAS, an optical cavity formed by two highly reflective mirrors is coupled with a broadband light beam. Subsequently, light escaped from the cavity undergoes dispersion through a grating monochromator and is detected by a sensitive photodiode array or a charge-coupled device (CCD) array. Gas species concentration levels are

determined using a least-square algorithm commonly employed in Differential Optical Absorption Spectroscopy (DOAS). IBBCEAS offers several advantages like: its experimental setup is cost-effective, simple, and suitable for field measurements; it does not require mode matching or mode-hop-free scanning, distinguishing it from CEAS; IBBCEAS can be applied across a spectral range from ~190 nm (ultraviolet) to ~10 μm (infrared); it allows the simultaneous measurement of multiple gas species in a broad wavelength range. Consequently, IBBCEAS finds wide applicability in various fields, including chemical analysis, gas sensing, water and air quality monitoring, remote vegetation sensing, process control both in existing and emerging domains [31-35].

3.4.5 Wavelength modulation spectroscopy

Molecules can absorb photons at specific wavelengths, inducing transitions from lower to higher energy levels. The amount of absorbed light at a given wavelength is proportionate to the fraction of molecules in the absorbing quantum state. Laser-Absorption Spectroscopy (LAS) stands on this relationship, offering quantitative measurements of gas temperature and composition. Wavelength-Modulation Spectroscopy (WMS), a LAS technique, enhances measurements in challenging environments. Professor Goldenstein has pioneered multiple WMS techniques, adopted worldwide, with ongoing efforts to enhance measurement capabilities and WMS-based diagnostics' quality [36-37]. The laser wavelength modulates at frequency f_m, embedding discrete frequencies in the detector signal while scanning the laser's nominal wavelength across a molecule's absorption transition. Modulation shifts absorption information to harmonics of f_m, extractable via digital lock-in filters in post-processing. Wavelength scanning allows measurement of WMS signal spectra. These signals are then employed to calculate gas concentration using calibration involved or calibration-free WMS models. WMS offers noise-rejection advantages, crucial for investigating hostile combustion environments [38-43].

3.4.6 Differential optical absorption spectroscopy

Differential Optical Absorption Spectroscopy (DOAS) was initially documented by Platt et al. [44]. The DOAS method involves positioning the light source and receiver several kilometers apart to utilize absorption spectroscopy for determining the concentrations of a specific species. The extended path length contributes to remarkable sensitivity. However, DOAS faces a limitation in spatial resolution, as it evaluates the average concentration of the sample along the entire path length. To address this limitation, Multi-Pass Optical Absorption Spectroscopy (MOAS) enhances spatial resolution by utilizing a White cell or Herriott Cell, providing an extended path length within a confined region. In DOAS, the direct measurement of the light intensity I_0 in the absence of the sample is not feasible. Hence, to ascertain the sample concentration, a differential absorption cross-section is utilized. Typically, the determination of this cross-section involves comparing the light intensity received by the detector both when the molecular absorption feature is on resonance and when it is off resonance. As a result, DOAS requires a reference spectrum acquired in the laboratory, which can be adjusted to atmospheric spectra to calculate the mixing ratio of the trace species [45-49].

3.4.7 Fourier transform infrared spectroscopy

Fourier-Transform Infrared Spectroscopy (FTIR) is a prominent technique utilized for obtaining the infrared spectrum of absorption or emission from solids, liquids, or gases [50-51]. The FTIR spectrometer captures high-resolution spectral data simultaneously across a broad spectral range, offering a significant advantage over dispersive spectrometers that measure intensity within a narrow wavelength range at a time. The name Fourier-transform infrared spectroscopy stems from the requirement for a mathematical process known as Fourier transform, which is essential for converting raw data into the actual spectrum. Absorption spectroscopy techniques, including FTIR and ultraviolet-visible (UV-vis) spectroscopy, aim to measure the light absorption of a sample at each wavelength. Unlike the

straightforward dispersive spectroscopy technique, which directs a monochromatic light beam at the sample, Fourier-transform spectroscopy utilizes a beam that encompasses multiple frequencies simultaneously. It measures how much of this beam is absorbed by the sample, and this process is rapidly repeated, generating a dataset that a computer then processes using the Fourier transform algorithm to deduce absorption at each wavelength.

The beam is generated by starting with a broadband light source containing the full spectrum of wavelengths to be measured. The incident light enters a Michelson interferometer, which is a mirror configuration featuring one mirror that is displaced by a motor. During the motion of the mirror, wave interference within the interferometer periodically obstructs and allows the transmission of each wavelength of light. This process generates a modulated beam with a distinct spectrum corresponding to each moment or mirror position. Computer processing is essential to transform the raw data, which includes light absorption at each mirror position, into the desired outcome, which is the light absorption for each wavelength. The Fourier transform algorithm is commonly employed for this conversion, turning the raw data, known as an interferogram, from one domain (mirror displacement in cm) into its inverse domain (wavenumbers in cm^{-1}) [52-56].

3.5 References

[1] W. Demtröder, "Molecular physics: theoretical principles and experimental methods." *John Wiley & Sons* (2008).

[2] C. N. Banwell, and E. M. McCash, "Fundamentals of molecular spectroscopy." *Indian Edition* (2017).

[3] C. H. Townes, and A. L. Schawlow, "Microwave spectroscopy." *Courier Corporation* (2013).

[4] M. H. Penner, "Basic principles of spectroscopy." *Food analysis*, 79 (2017).

[5] H. Förster, "UV/vis spectroscopy." *Characterization*, 337 (2004).

[6] M. Picollo, M. Aceto, and T. Vitorino, "UV-Vis spectroscopy." *Physical sciences reviews*, 4(4), 20180008 (2018).

[7] C. P. S. Hsu, "Infrared spectroscopy." *Handbook of instrumental techniques for analytical chemistry*, 249 (1997).

[8] J. B. Lambert, E. P. Mazzola, and C. D. Ridge, "Nuclear magnetic resonance spectroscopy: an introduction to principles, applications, and experimental methods." *John Wiley & Sons* (2019).

[9] J. Yano, and V. K. Yachandra, "X-ray absorption spectroscopy." *Photosynthesis research*, 102, 241 (2009).

[10] I. E. Gordon, L. S. Rothman, R. J. Hargreaves, R. Hashemi, E. V. Karlovets, F. M. Skinner, E. K. Conway, C. Hill, R. V. Kochanov, Y. Tan, and P. Wcisło, "The HITRAN2020 molecular spectroscopic database." *Journal of quantitative spectroscopy and radiative transfer*, 277, 107949 (2022).

[11] E. D. Hinkley, "High-Resolution Infrared Spectroscopy with a Tunable Diode Laser." *Applied Physics Letters*, 16(9), 351 (1970).

[12] M. Lackner, "Tunable diode laser absorption spectroscopy (TDLAS) in the process industries–a review." *Reviews in Chemical Engineering*, 23(2), 65 (2007).

[13] H. I. Schiff, G. I. Mackay, and J. Bechara, "The use of tunable diode laser absorption spectroscopy for atmospheric measurements." *Research on chemical intermediates*, 20, 525 (1994).

[14] S. Lin, J. Chang, J. Sun, and P. Xu, "Improvement of the detection sensitivity for tunable diode laser absorption spectroscopy: A review." *Frontiers in Physics*, *10*, 136 (2022).

[15] D. R. Bowling, S. D. Sargent, B. D. Tanner, and J. R. Ehleringer, "Tunable diode laser absorption spectroscopy for stable isotope studies of ecosystem–atmosphere CO_2 exchange." *Agricultural and forest meteorology*, 118(1-2), 1 (2003).

[16] B. Yu, X. Wu, M. Zhang, T. He, and J. Li, "Tunable diode laser absorption spectroscopy for open-path monitoring gas markers in fire combustion products." *Infrared Physics & Technology*, 131, 104690 (2023).

[17] D. Hutt, "Alexander Graham Bell's optical disc and other inventions" **(**1996).

[18] A. G. Bell, "Upon the production of sound by radiant energy." *The London, Edinburgh, and Dublin Philosophical Magazine and Journal of Science*, 11(71), 510 (1881).

[19] D. C. Dumitras, D. C. Dutu, C. Matei, A. M. Magureanu, M. Petrus, and C. Popa, "Laser photoacoustic spectroscopy: principles, instrumentation, and characterization." *Journal of Optoelectronics and Advanced Materials*, 9(12), 3655 (2007).

[20] B. K. Sarkar, and S. Sarkar, "Photoacoustic spectroscopy: A tool for optical properties study." *AIP Conference Proceedings*, 2305(1), (2020).

[21] A. Rosencwaig, "Photoacoustic spectroscopy. New tool for investigation of solids." *Analytical Chemistry*, 47(6), 592 (1975).

[22] S. Schilt, L. Thévenaz, M. Niklès, L. Emmenegger, and C. Hüglin, "Ammonia monitoring at trace level using photoacoustic spectroscopy in industrial and environmental applications." *Spectrochimica Acta Part A: Molecular and Biomolecular Spectroscopy*, 60(14), 3259 (2004).

[23] J. Li, W. Chen, and B. Yu, "Recent progress on infrared photoacoustic spectroscopy techniques." *Applied Spectroscopy Reviews*, 46(6), 440 (2011).

[24] A. O'Keefe, and D. A. Deacon, "Cavity ring-down optical spectrometer for absorption measurements using pulsed laser sources." *Review of scientific instruments*, 59(12), 2544 (1988).

[25] A. Maity, S. Maithani, and M. Pradhan, "Cavity ring-down spectroscopy: recent technological advancements, techniques, and applications." *Analytical Chemistry*, 93(1), 388 (2020).

[26] S. Maithani, and M. Pradhan, "Cavity ring-down spectroscopy and its applications to environmental, chemical and biomedical systems." *Journal of Chemical Sciences*, 132, 1 (2020).

[27] A. Maity, S. Maithani, A. Pal, and M. Pradhan, "Highresolution spectroscopic probing of ortho and para nuclear-spin isomers of heavy water in the gas phase." *Chemical Physics*, 541, 111041 (2021).

[28] M. D. Wheeler, S. M. Newman, A. J. Orr-Ewing, and M. N. Ashfold, "Cavity ring-down spectroscopy." *Journal of the Chemical Society, Faraday Transactions*, 94(3), 337 (1998).

[29] G. Berden, R. Peeters, and G. Meijer, "Cavity ring-down spectroscopy: Experimental schemes and applications." *International reviews in physical chemistry*, 19(4), 565 (2000).

[30] S. E. Fiedler, A. Hese, and A. A. Ruth, "Incoherent broad-band cavity-enhanced absorption spectroscopy." *Chemical physics letters*, 371(3-4), 284 (2003).

[31] K. Zheng, C. Zheng, Y. Zhang, Y. Wang, and F. K. Tittel, "Review of incoherent broadband cavity-enhanced absorption spectroscopy (IBBCEAS) for gas sensing." *Sensors*, 18(11), 3646 (2018).

[32] T. Wu, W. X. Zhao, W. D. Chen, W. Zhang, and X. Gao, "Incoherent broadband cavity enhanced absorption spectroscopy for in situ measurements of NO_2 with a blue light emitting diode." *Applied Physics B*, 94, 85 (2009).

[33] A. A. Ruth, S. Dixneuf, and R. Raghunandan, "Broadband cavity-enhanced absorption spectroscopy with incoherent light." *Cavity-enhanced spectroscopy and sensing*, Springer, 485 (2014).

[34] A. Aalto, G. Genty, T. Laurila, and J. Toivonen, "Incoherent broadband cavity enhanced absorption spectroscopy using supercontinuum and superluminescent diode sources." *Optics express*, 23(19), 25225 (2015).

[35] G. Wang, L. Meng, Q. Gou, B. Hanoune, S. Crumeyrolle, T. Fagniez, C. Coeur, R. Akiki, and W. Chen, "Novel broadband cavity-enhanced absorption spectrometer

for simultaneous measurements of NO_2 and particulate matter." *Analytical Chemistry*, 95(6), 3460 (2023).

[36] C. S. Goldenstein, C. A. Almodóvar, J. B. Jeffries, R. K. Hanson, and C. M. Brophy, "High-bandwidth scanned-wavelength-modulation spectroscopy sensors for temperature and H_2O in a rotating detonation engine." *Measurement Science and Technology*, 25(10), 105104 (2014).

[37] C. S. Goldenstein, "Wavelength-modulation spectroscopy for determination of gas properties in hostile environments." *Stanford University* (2014).

[38] J. M. Supplee, E. A. Whittaker, and W. Lenth, "Theoretical description of frequency modulation and wavelength modulation spectroscopy." *Applied Optics*, 33(27), 6294 (1994).

[39] G. B. Rieker, J. B. Jeffries, and R. K. Hanson, "Calibration-free wavelength-modulation spectroscopy for measurements of gas temperature and concentration in harsh environments." *Applied optics*, 48(29), 5546 (2009).

[40] B. Panda, A. Pal, and M. Pradhan, "Direct and 2f-wavelength modulation spectroscopy of NO and OCS using an astigmatic multipass cell coupled with a mid-IR 5.2 μm cw-QCL." *Laser Physics*, 32(3), 035702 (2022.).

[41] B. Panda, A. Pal, S. Chakraborty, and M. Pradhan, "An EC-QCL based dual-species (CH_4/N_2O) detection method at 7.8 μm in mid-IR region for simultaneous applications of atmospheric monitoring and breath diagnostics." *Infrared Physics & Technology*, 125, 104261 (2022).

[42] M. Pal, A. Maity, and M. Pradhan, "A continuous-wave quantum cascade laser near 7.5 μm combined with 2f-wavelength modulation spectroscopy for trace monitoring of ambient CH_4 concentrations." *Laser Physics*, 28(10), 105702 (2018).

[43] A. Maity, M. Pal, S. Maithani, G. D. Banik, and M. Pradhan, "Wavelength modulation spectroscopy coupled with an external-cavity quantum cascade laser operating between 7.5 and 8 μm." *Laser Physics Letters*, 15(4), p.045701 (2018).

[44] U. Platt, D. Perner, and H. W. Pätz, "Simultaneous measurement of atmospheric CH2O, O3, and NO2 by differential optical absorption." *Journal of Geophysical Research: Oceans*, 84(C10), 6329 (1979).

[45] B. ISAC, "Differential optical absorption spectroscopy." (1994).

[46] H. Edner, P. Ragnarson, S. Spännare, and S. Svanberg, "Differential optical absorption spectroscopy (DOAS) system for urban atmospheric pollution monitoring." *Applied optics*, 32(3), 327 (1993).

[47] C. Kern, S. Trick, B. Rippel, and U. Platt, "Applicability of light-emitting diodes as light sources for active differential optical absorption spectroscopy measurements." *Applied optics*, 45(9), 2077 (2006).

[48] J. Meinen, J. Thieser, U. Platt, and T. Leisner, "Using a high finesse optical resonator to provide a long light path for differential optical absorption spectroscopy: CE-DOAS." *Atmospheric Chemistry and Physics*, 10(8), 3901 (2010).

[49] F. A. Videla, D. C. Schinca, and J. O. Tocho, "Alternative method for concentration retrieval in differential optical absorption spectroscopy atmospheric-gas pollutant measurements." *Applied optics*, 42(18), 3653 (2003).

[50] A. Dutta, "Fourier transform infrared spectroscopy." *Spectroscopic methods for nanomaterials characterization*, 73 (2017).

[51] B. C. Smith, "Fundamentals of Fourier transform infrared spectroscopy." *CRC press* (2011).

[52] A. A. Ismail, F. R. van de Voort, and J. Sedman, "Fourier transform infrared spectroscopy: principles and applications." *Techniques and instrumentation in analytical chemistry,* 18, 93 (1997).

[53] J. Schmitt, and H. C. Flemming, "FTIR-spectroscopy in microbial and material analysis." *International Biodeterioration & Biodegradation*, 41(1), 1 (1998).

[54] M. Paraskevaidi, S. Karim, M. Santos, K. Lima, and S. Crean, "The use of ATR-FTIR spectroscopy for the diagnosis of Alzheimer's disease using oral buccal cells." *Applied Spectroscopy Reviews*, 1 (2023).

[55] Z. Bacsik, J. Mink, and G. Keresztury, "FTIR spectroscopy of the atmosphere. I. Principles and methods." *Applied Spectroscopy Reviews*, 39(3), 295 (2004).

[56] M. O. Guerrero-Pérez, and G. S. Patience, "Experimental methods in chemical engineering: Fourier transform infrared spectroscopy—FTIR." *The Canadian Journal of Chemical Engineering*, 98(1), 25 (2020).

Chapter: 4

High-resolution investigation of spectral doublets in ^{15}N-β-site nitrous oxide isotopomer

4.1 Introduction

The concept of *l*-type doubling in linear polyatomic molecules was first demonstrated by G. Herzberg and the phenomenon is primarily caused due to rotation-vibration interaction, where *l* is the vibrational angular momentum quantum number [1]. Later on, Neilsen and Shaffer pointed out the existence of *l*-type doubling with adequate theoretical explanations [2]. The *l*-type doubling leads to the splitting of degenerate energy levels due to Coriolis-type interaction which is the interaction between vibrational states in a rotating molecule. [3]. It is worth noting that this *l*-type doubling is entirely analogous to the Λ-type doubling of diatomic molecules that arises due to the coupling between the rotational motion and the unpaired electronic motion of the molecule, leading to the splitting of rotational energy levels. However, the accurate measurements of *l*-type doublet fine splitting of the isotopomers of linear nonsymmetrical molecules such as nitrous oxide (N_2O) are challenging because of extremely small splitting. Precise high-resolution spectroscopic data of *l*-type doublet splitting involving the parity doublet e and f sub-states deepens our understanding of the molecular properties of linear polyatomic molecules and their isotopomers. In the present study, we aimed to focus on N_2O molecule because of its site-specific isotopomers which arises due to the intramolecular distribution of ^{15}N-isotopes within N_2O. This molecule has also received special attention over the years because it is an active greenhouse gas in the atmosphere and also plays a significant role in stratospheric ozone-regulation chemistry [4-6].

N_2O is a non-symmetrical linear molecule (N-N-O) that comprises a few site-specific isotopologues among which $^{14}N^{15}N^{16}O$ and $^{15}N^{14}N^{16}O$ are most abundant with natural abundance of 0.364%. Some other isotopologues like $^{14}N^{14}N^{18}O$ and $^{14}N^{14}N^{17}O$ have an abundance of 0.198% and 0.036%, respectively and remaining isotopologues of nitrous oxide have much lesser abundances. When the heavy isotope of nitrogen, i.e. ^{15}N is at the central position within N_2O isotopomer, it is called α-site N_2O (or $^{15}N^{\alpha}$) and when ^{15}N is at the end-site, it is referred to as β-site isotopomer of N_2O (or $^{15}N^{\beta}$). Both $^{15}N^{\alpha}$ and $^{15}N^{\beta}$ isotopomers have identical masses and they are indistinguishable using the conventional mass-spectrometric (MS) methods. However, the site-specific spectroscopic signatures are attributed to ^{15}N-O and ^{14}N-O bonds within N_2O. The high-resolution mid-IR quantum cascade laser (QCL) spectroscopy provides the inherent advantage of site-selectivity along with ultra-high sensitivity and good time-resolution when it is combined with the optical cavity-enhanced absorption techniques such as cavity ring-down spectroscopy (CRDS) [7]. N_2O has three fundamental vibrational bands ν_1,ν_2 and ν_3 in the IR region in which the ν_1 and ν_3 are stretching modes, located at 1285 cm^{-1} (7.8 μm) and 2224 cm^{-1} (4.5μm), respectively. The ν_2 band which is a degenerate bending mode of vibration has its origin at long wavelengths near 589 cm^{-1} (17 μm). The ν_1 band is comparatively strong and until recently only few spectroscopic measurements of N_2O have been carried out in this fundamental band. In this study the splittings of *l*-type doublet features of β-site specific N_2O isotopomer were therefore accomplished by probing the $(11^10)\leftarrow(01^10)$ transition for Π state (i.e. l=1) vibrational state near 7.8 μm. It is important to note that in the 'ν_1' (stretching vibration) type $(11^10)\leftarrow(01^10)$ band, the doublets arise due to the non-zero value of l=1 and ν_2=1 in both the lower and upper states, which makes the energy levels non-degenerate as e and f levels.

Over the past decades, studies primarily focused on the measurements of various spectroscopic properties of $^{14}N_2^{16}O$ and its isotopes with abundances using Fourier-transform infrared spectrometry (FTIR) and Photo-ionization mass spectroscopy (PIMS) combined with IR spectroscopy [8-11]. The group of Liu and co-workers used the cavity ring-down spectroscopy (CRDS) to study ^{15}N-enriched N_2O isotopes to determine various ro-vibrational parameters around 1.56 μm [12]. CRDS technique

near 0.8 μm was also used by Song et al.to determine different spectroscopic parameters of ^{15}N-substituted N_2O in $6\nu_3$ bands [13]. Es-sebbar *et al*. reported the broadening coefficients and line intensities of N_2O in the ν_3 band near 4.5 μm [14]. In another earlier study, Shearer and co-workers measured the *l*-type doubling separations in the 1.5-2.4 μm region [15].Therefore, in view of the previous studies, the high-resolution spectroscopic investigation of *l*-type doublets of the site-specific α or β-isotopomers of N_2O and their fine splittings between e and f sub-states for l=1 or Π vibrational state near 7.8 μm has not been reported earlier (to our knowledge).

In this present work, we have studied the *l*-type doublet features of the transitions in the $(11^10)\leftarrow(01^10)$ band of $^{15}N^{14}N^{16}O$, such as the difference in doublet spacings in the P and R branches, the effect of pressure, temperature and the pressure broadening coefficients of the transitions on the doublets. Moreover, we have determined *l*-type doubling constants which were not mentioned in previous papers and we have also calculated the Coriolis constants. Hence, the present study presents a different approach and set of spectroscopic features different from the other studies. Nevertheless, for clarity we have included a table for comparison of the present work with previous spectroscopic studies for the $(11^10)\leftarrow(01^10)$ transition (Table 4.1). The present study thus offers new fundamental understanding of the *l*-type doubling in site-specific $^{15}N^{\beta}$ isotopomer.

Table 4.1: *Comparison of the present and previous works on the spectroscopic study of* $(11^10)\leftarrow(01^10)$ *transition band of* $^{15}N^{14}N^{16}O$.

Features	**Wang et al.[11]**	**C. Amiot[16]**	**Present Work**
Spectral Range	1250 – 1650 cm^{-1}	1750 – 6000 cm^{-1}	1245 – 1313 cm^{-1}
Resolution	0.005 cm^{-1}	0.001 cm^{-1}	0.001 cm^{-1}
Method used	Fourier transform spectroscopy	Fourier transform spectroscopy	CRDS
Path length	15 m	36 m	2500 m

Features determined	Line positions and assignment of ro-vibrational transitions, rotational constants, distortion constants	Band origins and Ro-vibrational transitions, rotational constants, distortion constants, Interaction between different levels	Line positions of the ro-vibrational transitions, rotational constants, distortion constants, *l*-type doubling constants, investigated the dependence of *l*-type doublet splitting on some external parameters or not, Coriolis constants, Pressure broadening coefficients

4.2 Experimental Section

CRDS technique coupled with a *cw*-EC QCL was used for this present work. The spectrometer was in our lab and its detailed experimental arrangement has been given elsewhere [7]. In brief, a widely-tunable water-cooled *cw* EC-QCL (MHF-41078; Daylight Solutions, USA) with mode-hop-free (MHF) tuning range of 7.5 µm-8 µm (1341-1257 cm^{-1}) was used as a high-power (~100 mW) optical source for this study. Recording of high-resolution ro-vibrational spectral lines was possible due to extremely narrow line width (~0.0003 cm^{-1}) of the *cw* EC-QCL. The measurement of wavenumbers of the EC-QCL was done by a wavemeter (621B-MIR; Bristol Instruments) with an accuracy of 0.001 cm^{-1}. The high- finesse optical cavity was constructed with a 50cm long quartz-coated cylindrical ring-down cell (RDC). Two highly reflective (HR) mirrors (R > 99.98%, CRD Optics Inc.; USA) were attached at

two ends of the RDC. The periodic resonance between laser mode and cavity mode was achieved by utilizing the cavity-length modulation technique when a ramp voltage was applied to the three piezo-electric transducers (PZT, Thorlabs PE4) attached to the end-HR mirror of RDC. The leaked-out optical signal from the cavity was focused onto a mercury-cadmium-telluride (MCT) detector (PVI-4TE-8-1X1, Vigo Systems S.A.). The output signal was then amplified using a preamplifier (SR560; Stanford Research Systems) and finally the data was acquired with the help of a high-speed data acquisition card (PCI 5122, 14-bit, 100 MHz bandwidth, National Instruments) and further analysis was carried out using custom written LabVIEW program. It is also noted that the optical cavity was wrapped with a heating jacket to perform the experiments at higher temperatures. Highly-sensitive pressure gauge from Pfeiffer Vacuum (CMR 361) was used to monitor the pressure inside the optical cavity.

4.3 Results and discussions

4.3.1 Setup parameters

In our CRDS experiments, we achieved a typical empty cavity ring-down time of τ_o = 8.6 μs and standard deviation (1σ) of 1.53% with an averaging of 20 successive ring-down events. From these parameters, the limiting sensitivity of the CRDS system i.e. minimum absorption coefficient was estimated to be $\alpha_{min} = 5.93 \times 10^{-8}$ cm^{-1}. The noise equivalent absorption coefficient (NEA) was determined to be 8.38×10^{-9} cm^{-1} $Hz^{-1/2}$. A typical detection limit for $^{15}N^{\beta}$ isotopomer in terms of mixing ratio at a cavity pressure of 30 Torr was determined to be ~17 ppbv (parts by billion by volume, 1 part in 10^9) for a transition line at 1290.7498 cm^{-1} with the line-strength of 8.563×10^{-21} cm^2 $molecule^{-1}cm^{-1}$ at 296 K. With allowance for the effect of pressure broadening, this detection limit at an ambient pressure of 1 atm would correspond to ~667 pptv (parts per trillion by volume, 1 part in 10^{12}).

4.3.2 High-resolution *l*-type doublet spectra of β-N_2O

To record the high-resolution CRDS spectra of *l*-type doublets for $^{15}N^{\beta}$ isotopomer, we have used a certified calibrated gas mixture of (33.0±0.4) ppmv (parts per million by volume, 1 part in 10^6) of β-N_2O gas (Cambridge Isotope Laboratories. Inc., USA, 99.99%) with zero-air (Air Liquid, UK, 99.99%) inside the optical cavity with a range of pressure 1.5-3.0 Torr depending on the experimental conditions. We probed rotationally resolved *l*-type doublet transitions with a resolution of 0.001 cm^{-1} for $^{15}N^{\beta}$ isotopomer in both P- and R-branches in the $(11^10)\leftarrow(01^10)$ ro-vibrational transition. There were 19 *l*-type doublets in the R-branch and 13 *l*-type doublets in the P-branch that we have primarily recorded in the 1245-1313 cm^{-1}spectral region. Spectral plots between the ring-down decay rate vs wavenumber are shown in Figure 4.1 and 4.2 for the P-and R-branches, respectively. The CRDS spectra were fitted with the Voigt line-shape function with the width constrained to that expected from Doppler broadening. We observed the fine *l*-type doublet splitting between e and f sub-states of the corresponding rotational lines in the Π vibrational state of $^{15}N^{\beta}$ isotopomer.

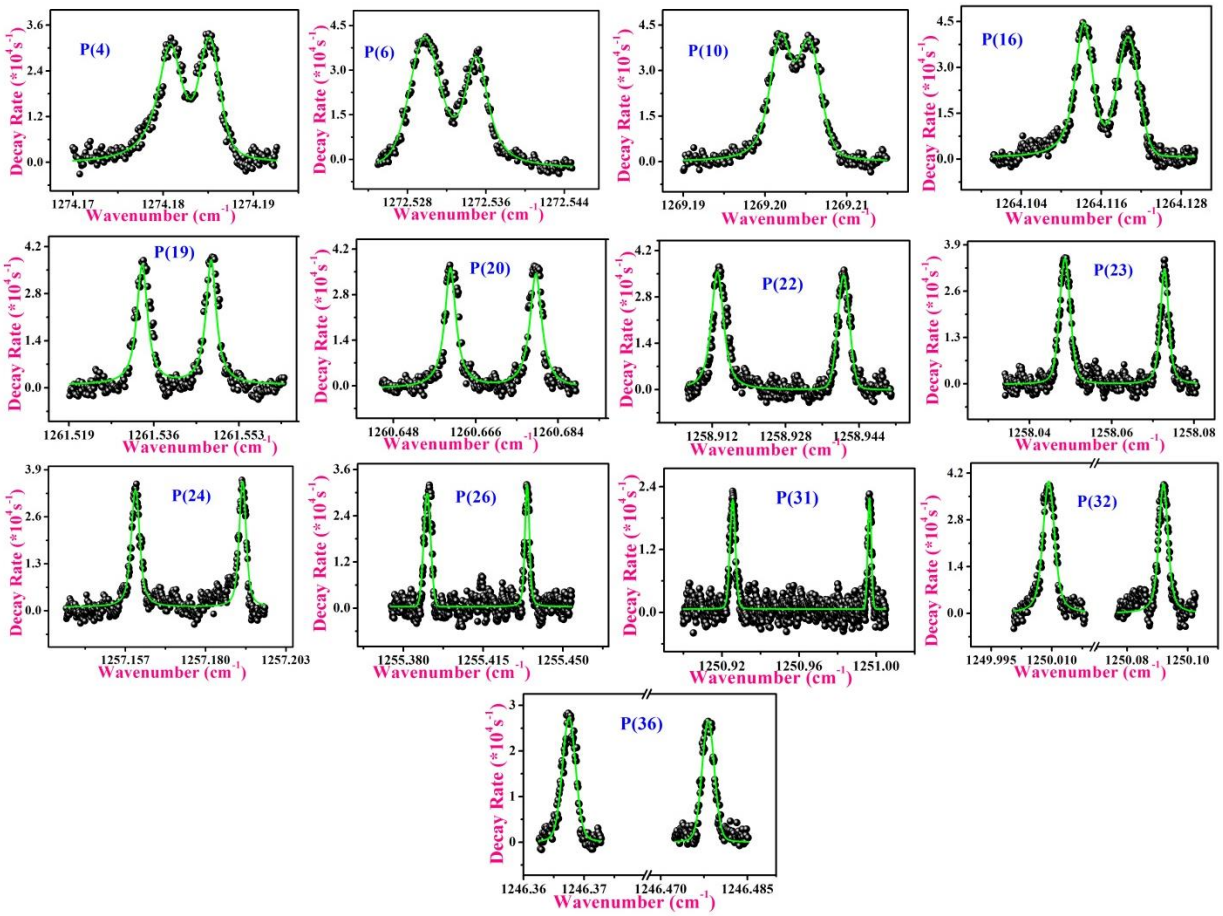

Figure 4.1: *CRDS spectra of l-type doublets of β-N_2O in P-branch for $(11^10)\leftarrow(01^10)$transition. Spectra were fitted with the Voigt line-shape function.*

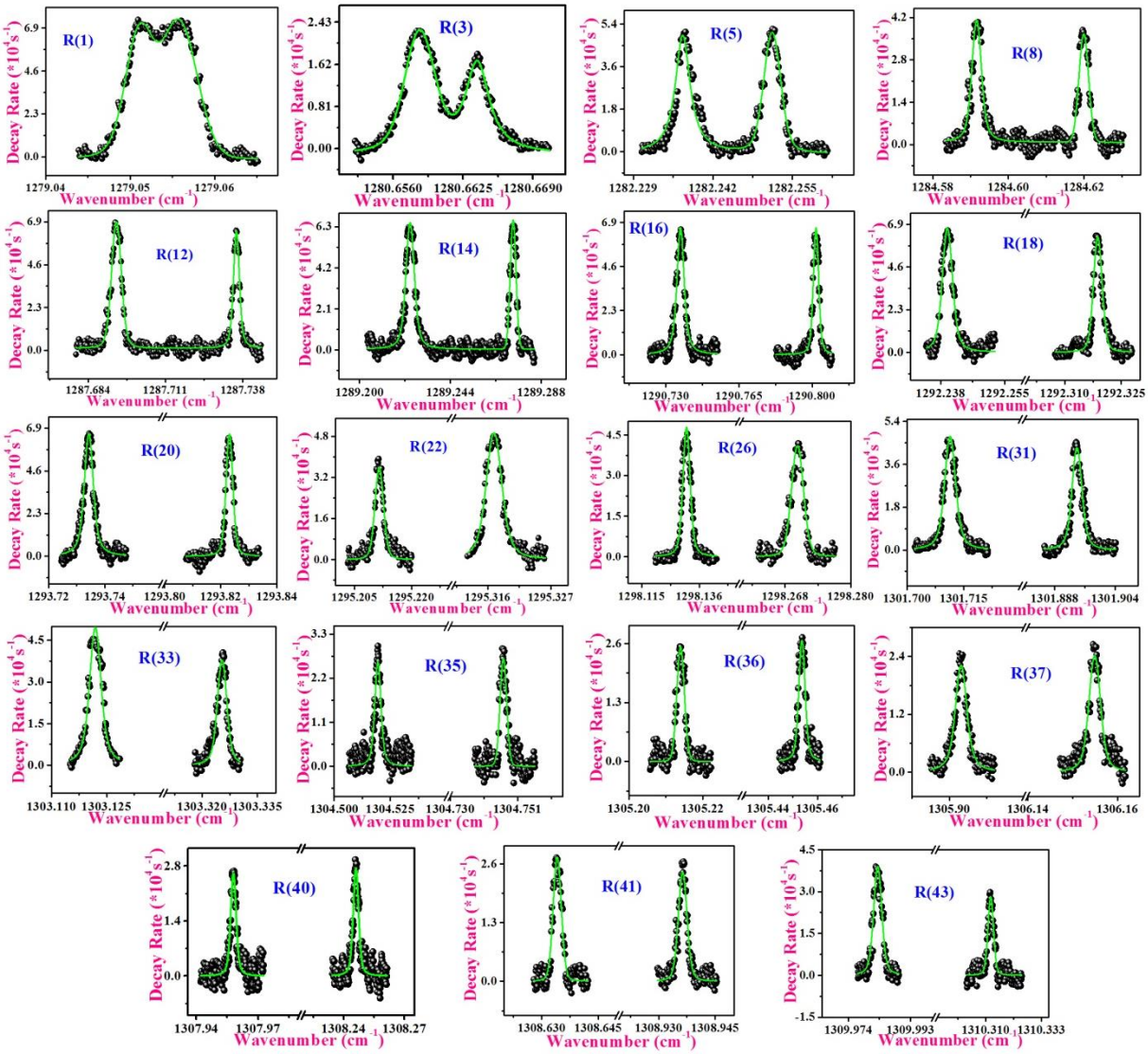

Figure 4.2: *CRDS spectra lines of l-type doublets of β-N_2O in R-branch for the* $(11^10)\leftarrow(01^10)$ *transition. Spectra were fitted with the Voigt line-shape function.*

We have tabulated all the experimentally recorded peak centres of the *l*-type doublets for both P-and R-branches in Table 4.2 and Table 4.3, respectively. We subsequently compared our experimentally obtained values with the values obtained from the HITRAN simulation [17,18] and also calculated the splitting between the e and f sub-components in cm^{-1}. The data obtained from our experiments agrees well with the values documented in the HITRAN database.

Table 4.2: *Experimental and HITRAN simulated line positions of e and f sub-states in P-branch for the (11^10)←(01^10) transition. J is the ground state rotational quantum number.*

J	CRDS Experimental			HITRAN simulation		
	Peak Center (cm^{-1}) (Pe)	Peak Center (cm^{-1}) (Pf)	(Pf)-(Pe) (cm^{-1})	Peak Center (cm^{-1}) (Pe)	Peak Center (cm^{-1}) (Pf)	(Pf)-(Pe) (cm^{-1})
36	1246.367(5)	1246.478(2)	0.110(7)	1246.38068	1246.49216	0.11148
32	1250.009(2)	1250.092(0)	0.082(8)	1250.0237	1250.10481	0.08111
31	1250.925(6)	1250.996(6)	0.071(0)	1250.92718	1251.00147	0.07429
26	1255.390(9)	1255.434(3)	0.043(4)	1255.40069	1255.44535	0.04466
24	1257.160(1)	1257.190(4)	0.030(3)	1257.16948	1257.20429	0.03481
23	1258.048(6)	1258.072(3)	0.023(7)	1258.04941	1258.07972	0.03031
22	1258.913(6)	1258.940(6)	0.027(0)	1258.92637	1258.95246	0.02609
20	1260.660(8)	1260.679(1)	0.018(3)	1260.67135	1260.68984	0.01849
19	1261.533(9)	1261.547(5)	0.013(6)	1261.53935	1261.55444	0.01509
16	1264.113(5)	1264.120(1)	0.006(6)	1264.12532	1264.13183	0.00651
10	1269.201(8)	1269.205(6)	0.003(8)	1269.212055	1269.21562	0.00357
6	1272.529(8)	1272.534(9)	0.005(1)	1272.54307	1272.54823	0.00516
4	1274.180(8)	1274.185(1)	0.004(3)	1274.19169	1274.19613	0.00444

Table 4.3: *Experimental and HITRAN simulated line positions of e and f sub-states in R branch for the (11^10)←(01^10) transition. J is the ground state rotational quantum number.*

J	CRDS Experimental			HITRAN simulation		
	Peak Center (cm^{-1}) (Re)	Peak Center (cm^{-1}) (Rf)	(Rf)-(Re) (cm^{-1})	Peak Center (cm^{-1}) (Re)	Peak Center (cm^{-1}) (Rf)	(Rf)-(Re) (cm^{-1})
1	1279.050(7)	1279.054(9)	0.004(2)	1279.06582	1279.06954	0.00372
3	1280.658(4)	1280.663(7)	0.005(3)	1280.66427	1280.67272	0.00845
5	1282.237(5)	1282.251(6)	0.014(1)	1282.25027	1282.26446	0.01419
8	1284.591(8)	1284.614(1)	0.022(3)	1284.60590	1284.63059	0.02469
12	1287.693(6)	1287.735(8)	0.042(2)	1287.70296	1287.74522	0.04226
14	1289.224(6)	1289.274(4)	0.049(8)	1289.23269	1289.28528	0.05259
16	1290.737(0)	1290.801(7)	0.064(7)	1290.74984	1290.81383	0.06399
18	1292.239(7)	1292.318(7)	0.079(0)	1292.25442	1292.33086	0.07644
20	1293.734(3)	1293.823(1)	0.088(8)	1293.74640	1293.83638	0.08998
22	1295.211(5)	1295.317(1)	0.105(6)	1295.22577	1295.33038	0.10461
26	1298.131(3)	1298.270(2)	0.138(9)	1298.14663	1298.28390	0.13727
31	1301.711(3)	1301.893(8)	0.182(5)	1301.72660	1301.91125	0.18465
33	1303.121(9)	1303.325(4)	0.203(5)	1303.13646	1303.34218	0.20572
35	1304.519(4)	1304.746(5)	0.227(1)	1304.53366	1304.76171	0.22805
36	1305.213(9)	1305.453(6)	0.239(7)	1305.22752	1305.46721	0.23969
37	1305.903(1)	1306.154(9)	0.251(8)	1305.91821	1306.16987	0.25166
40	1307.958(0)	1308.246(1)	0.288(1)	1307.97132	1308.26088	0.28956
41	1308.634(1)	1308.936(3)	0.302(2)	1308.64937	1308.95224	0.30287
43	1309.982(9)	1310.312(1)	0.329(2)	1309.99598	1310.32653	0.33055

4.4.3 Determination of *l*-type doubling constant

It was observed that with an increase in J value the splitting between the e and f sub-states increases for both P-and R-branches and the doublet spacing (Δν) are clearly distinguishable between the two branches as depicted in Figure 4.3. Here, the separation between the doublets (Δν in cm^{-1}) has been plotted against the rotational quantum number J. The *l*-type doubling constant was calculated from fittings of the plots using the following equation (4.1) [15]:

$$\Delta\nu = (q' + q'')m + (q' - q'')(m^2 - 1) \quad \textbf{(4.1)}$$

where, q' and q" are the *l*-type doubling constants for the upper and lower states, respectively, Δν is the separation between the doublets, m = -J for P-branch doublets and m=J+1 for R-branch doublets. In our study, the *l*-type doubling constants for the P-branch in the Π vibrational state (*l*=1) of $^{15}N^{\beta}$ isotopomer were found to be 8.33×10^{-4} cm^{-1} and 7.07×10^{-4} cm^{-1} for the upper and lower states, respectively. However, for the R-branch it was determined to be 7.589×10^{-4} cm^{-1} and 6.210×10^{-4} cm^{-1} for the upper and lower states, respectively.

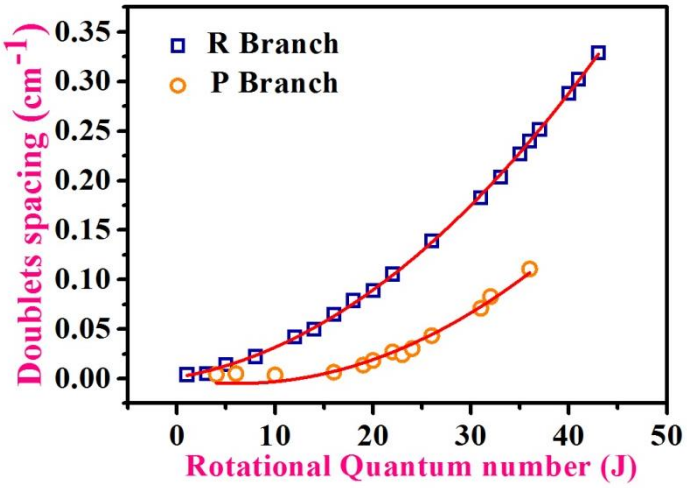

Figure 4.3: *Plot between Δν vs J of the doublets in P-and R-branches and fitted with the above equation (4.1).*

Subsequently, we determined the Coriolis constant Q_1 using the following equation (4.2) [15]:

$$q_\nu = Q_1(\nu_1 + 1) + Q_2(\nu_2 + 1) + Q_3(\nu_3 + 1) \quad \textbf{(4.2)}$$

where Q_i are referred to as the Coriolis constants, q_v is the doubling constant, v_1, v_2 and v_3 are vibrational quantum numbers of the state. In our study, the values of the Coriolis constants, Q_1 for the P-and R-branches are determined to be 1.25×10^{-4} and 1.38×10^{-4} cm^{-1}, respectively.

Next, we investigated if the doublet spacing is affected by parameters such as temperature and pressure. Keeping the temperature (298 K) fixed, we changed the pressure inside the optical cavity and calculated the corresponding splitting between e and f sub-states, but no significant change was observed in the *l*-type doubling constant (Figure 4.4a). Further, keeping the pressure fixed (~2.5 Torr) inside the cavity, we varied the temperature of the cavity from 298 K to 358 K as shown in Figure 4.4b, to observe the *l*-type doubling effect, but no significant change was noticed in the *l*-type doubling constant.

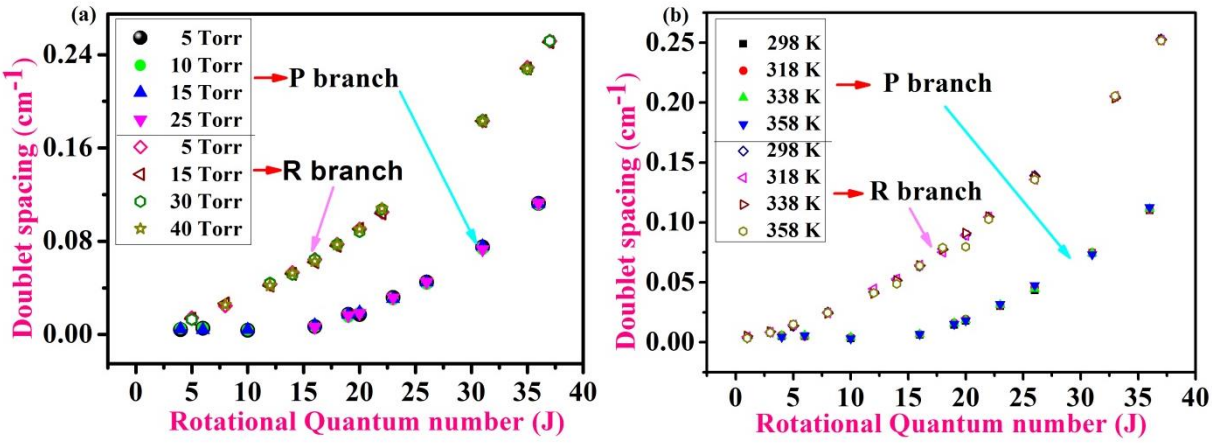

Figure 4.4: *Plots between the doublet spacing (Δ ν) vs Rotational quantum number (J) for the l-type doublets in P-and R-branches in the* $(11^10)\leftarrow(01^10)$ *transition* ***(a)*** *at different pressures and* ***(b)*** *at different temperatures.*

We have obtained the doubling constants for P- and R- branches and there is a slight difference in the doubling constant value for the respective branches and this might be due to the inherent property of the molecule and not due to the pressure. The selection rules for P- and R- branches are ΔJ = -1 and ΔJ = 1, respectively. P branch lies towards the lower wavenumber side and R branch lies towards the higher wavenumber side with respect to the Q branch. The spectrum that is expected based on the ideal situation consists of spectral lines equidistant in energy from one

another, separated by a value of 2B. But in reality, the lines in the R branch are more closely spaced with increasing wavenumber and that the lines of the P branch become further apart with decreasing wavenumber. This is attributable to two phenomena rotational-vibrational coupling and centrifugal distortion. If we look into Table 4.2 and Table 4.3 carefully it is found that the trend for the increase of doublet splittings with an increase in rotational quantum number is slightly different for P- and R- branches. Therefore, sample pressure will not bring any change in the *l*-type doubling constant of $^{15}N^{14}N^{16}O$. Nevertheless it should be mentioned that when we increase the pressure gradually, each component of the doublet will get broadened and after some optimum pressure it becomes difficult to distinguish between e and f components of the doublet. The experimental trend obtained in Table 4.2 and Table 4.3 has a good correlation with HITRAN simulation values for both P- and R- branches.

4.3.4 Pressure broadening effect *l*-type doublet spectral transitions

We then studied the effects of pressure broadening on the spectral doublets of $^{15}N^{\beta}$ isotopomer at room temperature. Calibrated gas mixture of β-N_2O was injected into the cavity and subsequently cavity-pressure was increased by injecting zero-air over it and spectral data were accumulated at different pressures ranging from 5 to 40 Torr. Figure 4.5 represents the pressure broadening effect on the doublets of $^{15}N^{\beta}$ in the $(11^10)\leftarrow(01^10)$ transition for Re(5) and Rf(5) spectral lines as a representative example. It was observed that with the increase in cavity- pressure, the peak height was decreased and gradually became wider, which eventually balanced the peak-area of the fitted absorption spectra. However, no shifts of the line-centre positions of the *l*-type doublet spectra due to pressure-induced effects were observed in our study. The *l*-type doublet CRDS spectra were fitted with the Voigt line-shape function. Figures 4.6a and 4.6b indicate the plots of the Lorentzian full-width at half-maximum (FWHM) against the optical cavity pressure. The pressure broadening coefficients (γ in cm^{-1} atm^{-1}) were calculated from the slope of the linear fit of the data set of the respective spectral transition lines.

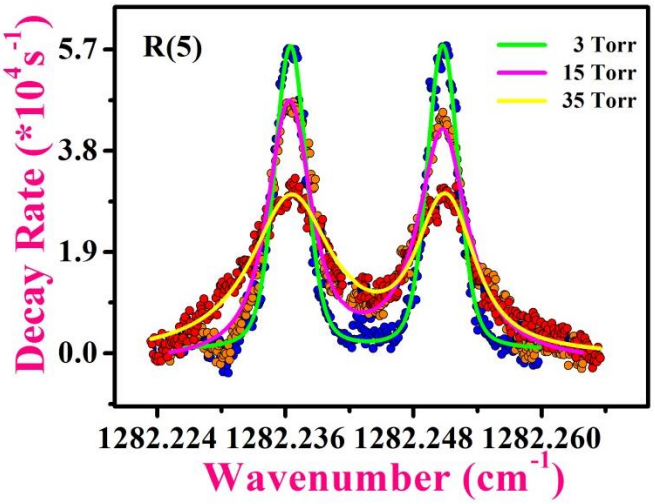

Figure 4.5: *Variation of R(5) spectral doublet with pressure in the (11^{1}0)←(01^{1}0) transition band.*

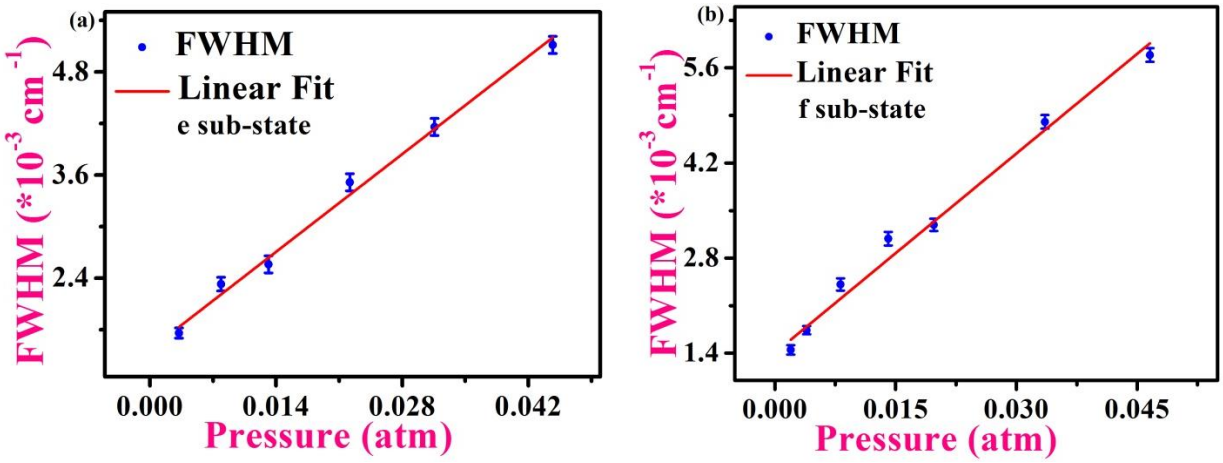

Figure 4.6: (a) & **(b)** *Linear plot of Lorentzian FWHM vs cavity pressure of e and f sub-states of R(5) doublet, respectively.*

Pressure broadening coefficients for the *l*-type doublet spectral lines of Re(5) and Rf(5) were determined to be γ=(0.095 ± 0.003) cm^{-1} atm^{-1} and γ=(0.081 ± 0.004) cm^{-1} atm^{-1},respectively. Broadening coefficients for all other spectral lines of the P-and R-branches involving e and f sub-states are tabulated in Table 4.4a and 4.4b. The experimental values obtained by the CRDS measurements were compared with the HITRAN simulated values and a good agreement was obtained between them,

whereas the values in the HITRAN database are associated with an uncertainty ranging from 5% to 10% [17,18].

Henceforth, we explored if there was any dependency of the pressure broadening coefficients with the rotational quantum number (J). We then plotted the pressure broadening coefficients as a function of J as shown in Figures 4.7a and 4.7b and we observed that broadening coefficients decreased with increase of J irrespective of P- or R-branch involving e and f sub-states.

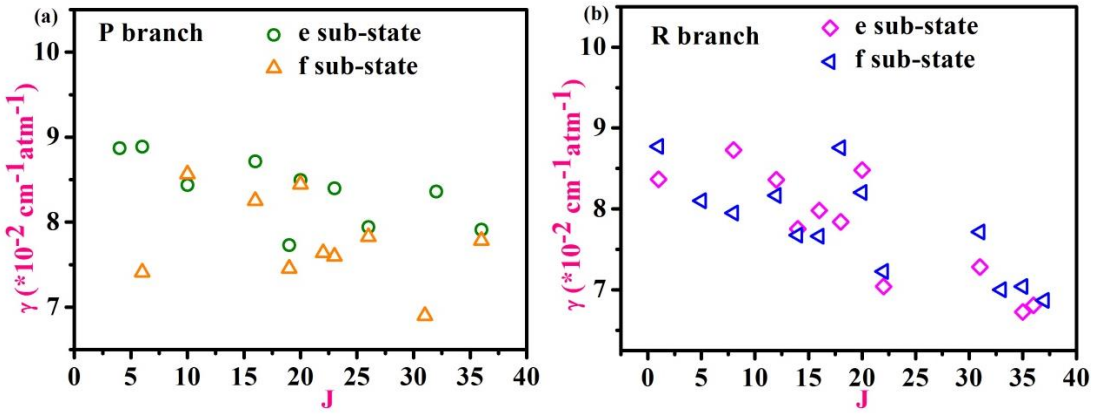

Figure 4.7: (a) *Dependence of pressure broadening coefficient (γ) with J in P branch for e and f sub-states.* **(b)** *Dependence of pressure broadening coefficient (γ) with J in R branch for e and f sub-states.*

Table 4.4a: *Experimental and HITRAN simulated pressure broadening coefficients of beta nitrous oxide for e and f sub-states in the P-branch.*

P(01^10 – 11^10)e				P(01^10 – 11^10)f			
Wavenumber (cm^{-1})	J	Pressure Broadening coefficient (cm^{-1} atm^{-1})		Wavenumber (cm^{-1})	J	Pressure Broadening coefficient (cm^{-1} atm^{-1})	
		Experimental CRDS	HITRAN			Experimental CRDS	HITRAN
1246.367(5)	36	0.079 ± 0.002	0.0700	1246.478(2)	36	0.077 ± 0.005	0.0699
1250.009(2)	32	0.083 ± 0.003	0.0710	1250.996(6)	31	0.069 ± 0.002	0.0713
1250.925(6)	31	0.096 ± 0.001	0.0713	1255.434(3)	26	0.078 ± 0.004	0.0729
1255.390(9)	26	0.079 ± 0.006	0.0729	1258.072(3)	23	0.075 ± 0.007	0.0741

1258.048(6)	23	0.083 ± 0.006	0.0741	1258.940(6)	22	0.076 ± 0.001	0.0745
1260.660(8)	20	0.084 ± 0.001	0.0755	1260.679(1)	20	0.084 ± 0.001	0.0755
1261.533(9)	19	0.077 ± 0.003	0.0760	1261.547(5)	19	0.074 ± 0.006	0.0760
1264.113(5)	16	0.087 ± 0.001	0.0778	1264.120(1)	16	0.082 ± 0.001	0.0778
1269.201(8)	10	0.084 ± 0.006	0.0827	1269.205(6)	10	0.085 ± 0.003	0.0827
1272.529(8)	6	0.088 ± 0.002	0.0874	1272.534(9)	6	0.074 ± 0.003	0.0874
1274.180(8)	4	0.088 ± 0.001	0.0901	1274.185(1)	4	0.106 ± 0.003	0.0901

Table 4.4b: *Experimental and HITRAN simulated pressure broadening coefficients of beta nitrous oxide for e and f sub-states in the R-branch.*

R($01^10 - 11^10$)e				R($01^10 - 11^10$)f			
Wavenumber (cm^{-1})	J	Pressure Broadening coefficient (cm^{-1} atm^{-1})		Wavenumber (cm^{-1})	J	Pressure Broadening coefficient (cm^{-1} atm^{-1})	
		Experimental CRDS	HITRAN			Experimental CRDS	HITRAN
1279.050(7)	1	0.083 ± 0.004	0.0941	1279.054(9)	1	0.087 ± 0.005	0.0941
1282.237(5)	5	0.095 ± 0.003	0.0881	1282.251(6)	5	0.081 ± 0.004	0.0881
1284.591(8)	8	0.087 ± 0.001	0.0849	1284.614(1)	8	0.079 ± 0.002	0.0849
1287.693(6)	12	0.083 ± 0.002	0.0801	1287.735(8)	12	0.081 ± 0.003	0.0801
1289.224(6)	14	0.077 ± 0.003	0.0785	1289.274(4)	14	0.076 ± 0.001	0.0785
1290.737(0)	16	0.079 ± 0.005	0.0771	1290.801(7)	16	0.076 ± 0.005	0.0771
1292.239(7)	18	0.078 ± 0.001	0.0760	1292.318(7)	18	0.087 ± 0.001	0.0760
1293.734(3)	20	0.084 ± 0.003	0.0750	1293.823(1)	20	0.082 ± 0.002	0.0750
1295.211(5)	22	0.070 ± 0.001	0.0741	1295.317(1)	22	0.072 ± 0.003	0.0741
1301.711(3)	31	0.072 ± 0.001	0.0710	1301.893(8)	31	0.077 ± 0.001	0.0710
1304.519(4)	35	0.067 ± 0.004	0.0699	1303.325(4)	33	0.070 ± 0.005	0.0704
1305.213(9)	36	0.068 ± 0.001	0.0696	1304.746(5)	35	0.070 ± 0.002	0.0699
1305.903(1)	37	0.042 ± 0.006	0.0694	1306.154(9)	37	0.068 ± 0.005	0.0694

4.3.5 Evaluation of band centres, rotational constants and centrifugal distortion constants

Finally, we investigated the band centres, rotational constants and centrifugal distortion constants of e and f sub-states of the (11^10) and (01^10) vibrational levels. To measure such parameters, we have scanned the *l*-type doublet spectra of the probed rotational lines belonging to the (11^10)←(01^10) transition and noted the transition frequencies of e and f sub-states. Further, these transition frequencies were then fitted with the equation (4.3) [19]:

$$\nu = \nu_o + B'_v[J'(J'+1) - l^2] - D'_v[J'(J'+1) - l^2]^2 - B''_v[J''(J''+1) - l^2] + D''_v[J''(J''+1) - l^2]^2 \quad \textbf{(4.3)}$$

where, ν is the peak centre, ν_o is the band centre, B'_v and B''_v are rotational constants of higher and lower states, respectively, D'_v and D''_v are centrifugal distortion constants of higher and lower states, respectively. All the new spectroscopic values of the band centres and rotational constants determined in this context have been tabulated in Table 4.5.

Table 4.5: *Values of the band centre and rotational constants from our experiment for e and f sub-states of β-N_2O in the (11^10)←(01^10) transition. All values are in cm^{-1}.*

Branch & sub-state	ν_o	B'_v	B''_v
Pe(11^10)←(01^10)	1277.441(5)	0.40345	0.40501
Pf(11^10)←(01^10)	1277.437(8)	0.40362	0.40518
Re(11^10)←(01^10)	1277.438(3)	0.40407	0.40572
Rf(11^10)←(01^10)	1277.439(9)	0.40455	0.40599

The values of the band centres determined in our study was consistent with and of comparable accuracy to the values of 1277.45496 cm^{-1} predicted by Robert A. Toth [20]. Moreover, we used the centrifugal distortion constant of lower state (i.e. 01^10(e)

& 01^10(f)) from the earlier study [11] and subsequently we evaluated the new values of the centrifugal distortion constants for the upper states, that were found to be 1.81×10^{-7} cm^{-1}, 1.68×10^{-7} cm^{-1}, 1.56×10^{-7} cm^{-1} and $1.53\times10^{-7}cm^{-1}$ for the Pe(11^10), Pf(11^10), Re(11^10) and Rf(11^10), respectively. Taken together, our findings on *l*-type doubling of $^{15}N^{\beta}$ isotopomer provide fundamental spectroscopic information that will help for better understanding of site-specific isotopomers of several other linear polyatomic molecules.

Table 4.6: *Comparison of the rotational and centrifugal distortion constants between present and previous works on the spectroscopic study of (11^10)←(01^10) transition band of $^{15}N^{14}N^{16}O$.*

v_1, v_2, *l*, v_3	Constants	Wang et al.[11]	Present Work
(01^10)e	B_v (cm^{-1})	0.405037265	0.40501
(01^10)f	Bv (cm^{-1})	0.405781109	0.40518
(11^10)e	B_v (cm^{-1})	0.403489655	0.40345
	Dv (cm^{-1})	1.609708×10^{-7}	1.81×10^{-7}
(11^10)f	Bv (cm^{-1})	0.404358647	0.40362
	Dv (cm^{-1})	1.575290×10^{-7}	1.68×10^{-7}

Table 4.7: *Comparison of the band centre as obtained from present and previous works on the spectroscopic study of (11^10)←(01^10) transition band of $^{15}N^{14}N^{16}O$.*

	Band	Robert A. Toth[20]	Present work
Band Centre (cm^{-1})	(11^10)←(01^10)(e)	1277.45496	1277.441(5)
	(11^10)←(01^10)(f)	1277.45496	1277.437(8)

4.4 Conclusion

High-resolution spectroscopic investigation of *l*-type doubling of β-site isotopomer of N_2O, so- called $^{15}N^{\beta}$ was performed in the ν_1 fundamental vibration band at 7.8 μm

using the *cw* EC-QCL based ultra-sensitive CRDS technique. We probed 32 *l*-type doublet spectral lines between e and f sub-states corresponding to the P- and R-branches in the $(11^10)\leftarrow(01^10)$ transition. Various new spectroscopic parameters such as rotational constants, centrifugal distortion constants, *l*-type doubling constants and Coriolis constants of $^{15}N^{\beta}$ isotopomer were determined in the Π vibrational state (l=1) in the mid-IR "fingerprint" spectral region which were not explored earlier. Furthermore, pressure broadening coefficients of the probed doublets of $^{15}N^{\beta}$ were determined. The incorporation of the newly acquired experimental data will enhance our comprehension of the site-specific β-site isotopomer of N_2O and intramolecular distribution of ^{15}N isotopes in linear polyatomic molecules.

.

4.5 References

[1] G. Herzberg, "*l*-type doubling in linear polyatomic molecules." *Reviews of Modern Physics*, 14, 219 (1942).

[2] H. H. Nielsen and W. H. Shaffer, "A Note Concerning *l*-Type Doubling in Linear Polyatomic Molecules." *The Journal of Chemical Physics*, 11, 140 (1943).

[3] C. H. Townes and A. L. Schawlow, "Microwave spectroscopy," *New York: Dover Publications*, (1975).

[4] J. Mohn, B. Tuzson, A. Manninen, N. Yoshida, S. Toyoda, W. A. Brand and L. Emmenegger, "Site selective real-time measurements of atmospheric N_2O isotopomers by laser spectroscopy." *Atmospheric Measurement Techniques*, 5, 1601 (2012).

[5] E. Ibraim, B. Wolf, E. Harris, R. Gasche, J. Wei, L. Yu, R. Kiese, S. Eggleston, K. B. Bahl, M. Zeeman, B. Tuzson, L. Emmenegger, J. Six, S. Henne, and J. Mohn, "Attribution of N_2O sources in a grassland soil with laser spectroscopy based isotopocule analysis." *Biogeosciences*, 16, 3247 (2019).

[6] A. N. Hayhurst and A. D. Lawrence, "Emissions of nitrous oxide from combustion sources." *Progress in Energy and Combustion Science*, 18, 529 (1992).

[7] A. Maity, M. Pal, G. D. Banik, S. Maithani and M. Pradhan, "Cavity ring-down spectroscopy using an EC-QCL operating at 7.5 μm for direct monitoring of methane isotopes in air." *Laser Physics Letters*, 14, 115701 (2017).

[8] R. A. Toth, "Frequencies of N_2O in the 1100-to 1440 cm^{-1} region." *JOSA B*, 3, 1263 (1986).

[9] R. A. Toth, "Line positions and strengths of N_2O between 3515 and 7800 cm^{-1}." *Journal of Molecular Spectroscopy*, 197, 158 (1999).

[10] R. A. Toth, "Line strengths of N_2O in the 1120–1440 cm^{-1} region." *Applied Optics*, 23, 1825 (1984).

[11] C. Y. Wang, A. W. Liu, V. I. Perevalov, S. A. Tashkun, K. F. Song and S. M. Hu, "High-resolution infrared spectroscopy of $^{14}N^{15}N^{16}O$ and $^{15}N^{14}N^{16}O$ in the 1200–3500 cm^{-1} region." *Journal of Molecular Spectroscopy*, 257, 94 (2009).

[12] A. W. Liu, C. L. Hu, J. Wang, V. I. Perevalov and S. M. Hu, "Cavity ring-down spectroscopy of ^{15}N enriched N_2O near 1.56 μm." *Journal of Quantitative Spectroscopy and Radiative Transfer*, 232, 1 (2019).

[13] K. F. Song, B. Gao, A. W. Liu, V. I. Perevalov, S. A. Tashkun and S. M. Hu, "Cavity ring-down spectroscopy of the $6\nu_3$ bands of ^{15}N substituted N_2O." *Journal of Quantitative Spectroscopy and Radiative Transfer*, 111, 2370 (2010).

[14] E. Es-sebbar, M. Deli and A. Farooq, "Quantum Cascade Laser Measurements of Line Intensities, N_2-, O_2-and Ar-Collisional Broadening Coefficients of N2O in the ν_3 Band Near 4.5 μm." *Applied Spectroscopy*, 70, 972 (2016).

[15] J. N. Shearer, T. A. Wiggins, A. H. Guenther, and D. H. Rank, "*l*-Type Doubling in N_2O." *The Journal of Chemical Physics*, 25, 724 (1956).

[16] C. Amiot. "Vibration-rotation bands of $^{14}N^{15}N^{16}O$ - $^{15}N^{14}N^{16}O$: 1.6–5.7 μm region." *Journal of Molecular Spectroscopy*, 59, 191 (1976).

[17] L. S. Rothman, D. Jacquemart, A. Barbe, D. Chris Benner, M. Birk, L. R. Brown, M. R. Carleer, C. Chackerian, K. Chance, L. H. Coudert, V. Dana, V. M. Devi, J. M.

Flaud, R. R. Gamache, A. Goldman, J. M. Hartmann, K. W. Jucks, A. G. Maki, J. Y. Mandin, S. T. Massie, J. Orphal, A. Perrin, C. P. Rinsland, M. A. H. Smith, J. Tennyson, R. N. Tolchenov, R. A. Toth, J. Vander Auwera, P. Varanasi, G. Wagner, "The HITRAN 2004 molecular spectroscopic database." *Journal of Quantitative Spectroscopy and Radiative Transfer*, 96, 139 (2005).

[18] L. S. Rothman, I. E. Gordon, Y. Babikov, A. Barbe, D. Chris Benner, P. F. Bernath, M. Birk, L. Bizzocchi, V. Boudon, L. R. Brown, A. Campargue, K. Chance, E. A. Cohen, L. H. Coudert, V. M. Devi, B. J. Drouin, A. Fayt, J. M. Flaud, R. R. Gamache, J. J. Harrison, J. M. Hartmann, C. Hill, J. T. Hodges, D. Jacquemart, A. Jolly, J. Lamouroux, R. J. Le Roy, G. Li, D. A. Long, O. M. Lyulin, C. J. Mackie, S. T. Massie, S. Mikhailenko, H. S. P. Müller, O. V. Naumenko, A. V. Nikitin, J. Orphal, V. Perevalov, A. Perrin, E. R. Polovtseva, C. Richard, M. A. H. Smith, E. Starikova, K. Sung, S. Tashkun, J. Tennyson, G. C. Toon, V. G. Tyuterev and G. Wagne, "The HITRAN 2012 molecular spectroscopic database." *Journal of Quantitative Spectroscopy and Radiative Transfer*, 130, 4 (2013).

[19] G. D. Banik, S. Som, A. Maity and M. Pradhan, "Cavity ring-down spectroscopy measurements of *l*-type doubling of hot bands in Δ vibrational states of OCS near 5.2 μm." *Journal of Physics Communications*, 2, 045014 (2018).

[20] Rob. A. Toth, "Line strengths (900–3600 cm^{-1}), self-broadened linewidths, and frequency shifts (1800–2360 cm^{-1}) of N_2O." *Applied Optics*, 32, 7326 (1993).

Chapter: 5

Study of doublet splittings in Δ vibrational state of $^{15}N^{14}N^{16}O$ using QCL based CRDS system

5.1 Introduction

The *l*-type doubling of linear polyatomic molecules is an important aspect in molecular spectroscopy. This concept was introduced by Herzberg [1] and subsequently its theoretical framework was demonstrated by Neilsen and Shaffer [2]. It is known that the bending or perpendicular vibrations of linear polyatomic molecules are doubly degenerate when the molecules are not rotating. But when molecular rotation is introduced, there is an interaction between rotational and vibrational motion which induces the splittings of the degenerate energy levels and removes the degeneracy. This phenomenon is known as *l*-type doubling, where *l* is the vibrational angular momentum quantum number and this doubling is mainly due to Coriolis-type interaction between perpendicular vibration and rotation. High-resolution spectroscopic measurements of *l*-type doubling can provide several important information of molecular properties such as doubling constants, Coriolis constants, Coriolis interaction, rotational constants, and centrifugal distortion constants. The *l*-doubling effect is usually significant in the lower states for which l =1 (i.e. Π state) but the *l*-doublet splittings are extremely small for l = 2 (i.e. Δ state) or higher states. Therefore it is a great challenge to measure the *l*-doubling effects in Δ state involving the parity doublet e and f sub-states. It is noteworthy to mention that if we have to observe such small splittings in Δ vibrational state, then usually high rotational states need to be probed [3].

Nitrous oxide is a linear polyatomic molecule having two nitrogen atoms and one oxygen atom ($^{14}N^{14}N^{16}O$). Two stable isotopes of nitrogen (^{14}N and ^{15}N) and three isotopes of oxygen (^{16}O, ^{17}O, and ^{18}O) combine to form a total of

twelve isotopic molecules of nitrous oxide. Among all the isotopes, the site-specific alpha-nitrous oxide (α-N_2O) ($^{14}N^{15}N^{16}O$) and beta-nitrous oxide (β-N_2O) ($^{15}N^{14}N^{16}O$) depending on the centre and end position of ^{15}N within the linear NNO molecule are the most natural abundant species of nitrous oxide isotope. N_2O is an important trace molecule and active greenhouse gas in the atmosphere. It plays a significant role in global warming and stratospheric ozone depletion [4-6]. High-resolution spectroscopic investigation of N_2O and its site-specific isotopomers is an interesting field to be explored for better fundamental understanding of linear polyatomic molecular properties. We have explored the β-N_2O isotopomer and its fine *l*-doublet splittings arising from the $(12^20)\leftarrow(02^20)$ ro-vibrational transition near 7.8 μm mid-infrared wavelength region using an ultra-sensitive optical cavity-enhanced absorption technique such as CRDS coupled with a continuous-wave (cw) EC-QCL.

Over the past studies mainly focused on the detection of N_2O sample concentration along with spectroscopic measurements of line strength, line positions, pressure induced frequency shift for N_2O using Fourier transform infrared spectroscopy (FTIR) [7-9]. But only few studies were performed related to *l*-type doubling of N_2O and its isotopes [10-12]. However, few studies have been performed so far to explore the fine *l*-doublet splittings for l = 2 or Δ vibrational states of α-N_2O or β-N_2O isotopomer. Our study was focused to determine the characteristics of the doublet spectral lines in the (02^20) to (12^20) band. Robert A. Toth in his paper has reported several bands of nitrous oxide and its isotopomers, where the author discussed band centres and different rotational constants. A.W.Liu et al. in their few papers studied several spectroscopic properties of N_2O and its isotopes using cavity ring-down spectroscopy but they have different spectral regions of working compared to this present work. A table of comparison is depicted below clearly to visualize the difference of the present work with the previous work (Table 5.1).

In this study, we first report the experimental observation of *l*-type doublets of β-N_2O for l = 2 in the $(12^20)\leftarrow(02^20)$ ro-vibrational transition. We employed the EC-QCL based CRDS technique to study the fine structure lines of *l*-doublet splittings between the parity doublet e and f sub-states corresponding to P-branch of β-N_2O in

the region 1341-1257 cm^{-1}. We probed the doublets with relatively high J values and the corresponding doublet splittings were utilized to evaluate Coriolis constants, band centres, rotational constants and centrifugal distortion constants. Pressure broadening effect was also studied for e and f sub-states of these doublets. This investigation provides novel experimental evidence, contributing to an enhanced fundamental understanding of the properties of linear polyatomic molecules.

Table 5.1: *Comparison of the present and previous works on the spectroscopic study of* $(12^20) \leftarrow (02^20)$ *transition band of* $^{15}N^{14}N^{16}O$.

Features	**Robert A. Toth**	**AlSaif et al.**	**Wang et al.**	**Present Work**
Spectral Range	1100 – 1440 cm^{-1}	1240-1310 cm^{-1}	1250 – 1650 cm^{-1}	1245 – 1313 cm^{-1}
Resolution	0.005 cm^{-1}	-	0.005 cm^{-1}	0.001 cm^{-1}
Method used	Fourier transform spectroscopy	Frequency locking of an EC-QCL	Fourier transform spectroscopy	CRDS
Path length	73 m	-	15 m	2500 m
Molecule	N_2O and its isotopes	$^{14}N^{14}N^{16}O$	N_2O and its isotopes	$^{15}N^{14}N^{16}O$
Features determined	Line positions of ro-vibrational transitions, band centres, rotational constants, distortion constants	Line positions of ro-vibrational transitions, few spectroscopic parameters	Line positions and assignment of ro-vibrational transitions, rotational constants, distortion	Line positions of the ro-vibrational transitions, rotational constants, distortion constants, l-type doubling constants, Coriolis constants, Pressure

			constants	broadening coefficients

5.2 Experimental technique

We have used a continuous wave (cw) external-cavity (EC) quantum cascade laser (QCL) (MHF-41078; Daylight Solutions, USA) based cavity ring-down spectroscopy (CRDS) setup to perform this current work. Here we have briefly described the experimental setup and its detailed description has been given elsewhere [13,14]. The EC-QCL light source in the mid infrared region operates at the centre wavelength ~7.8 μm. This water cooled EC-QCL has a specified mode-hop-free (MHF) tuning range of 7.5 μm-8 μm (1341 cm^{-1}-1257 cm^{-1}) with a linewidth of 0.0003 cm^{-1} and high output power of > 80 mW. Initially, a highly intense and adequately collimated laser beam underwent passage through an optical isolator (FIO-5-7.8; Innovation Photonics) designed to inhibit the back reflection of laser light. An acousto-optic-modulator (AOM) (AGM406B11M; IntraAction Corp; USA) which acts as an optical switch diffracts the laser beam into zeroth order and first order. The zeroth order beam was directed towards the wavemeter (621B-MIR; Bristol Instruments) for continuous and real-time monitoring of the wavenumber of the laser beam with an accuracy of ± 0.001 cm^{-1}. The first order beam was coupled with the ring-down cell (RDC) and was precisely aligned along the central axis of the optical cavity. The cavity consists of 50 cm long quartz-coated RDC and two highly reflective mirrors (CRD Optics Inc.;USA) were fixed at the two ends of RDC. The light transmitting from the cavity was detected with a thermoelectrically cooled mid-IR mercury cadmium telluride (MCT) detector (PVI-4TE-8-1X1, Vigo Systems S.A.).

The modulation of the cavity length was achieved by utilizing three piezoelectric transducers (PZT, Thorlabs PE4) which were attached to one of the mirror mounts of RDC. This helped to attain the periodic resonance between laser mode and cavity

mode. This periodic coupling between the laser mode and cavity mode was obtained by applying the triangular voltage simultaneously to the three PZTs as well as to modulate the cavity length over one free spectral range (FSR). When the cavity mode and the laser mode came into resonance, the intra-cavity light is built up and the decay of this signal is captured using a high-speed data acquisition card (PCI 5122, 14-bit, 100 MHz bandwidth, National Instruments) and further it was analysed by a custom written LabVIEW program.

We have achieved an empty cavity ring-down time of τ_o = 8.6 μs which is inverse of decay rate (i.e. k = $1/\tau$) with standard deviation (1σ) of 1.53%, by averaging twenty successive ring down events for the current experimental measurements. The limiting sensitivity which is minimum absorption coefficient (α_{min}) was estimated to be 5.93 x 10^{-8} cm^{-1} using the following equation 5.1:

$$\alpha_{min} = \frac{\Delta\tau_{min}}{c\tau_0^2} \quad \textbf{(5.1)}$$

Where c is the speed of light, τ_o is empty cavity ring down time, $\Delta\tau_{min}$ is the minimum detectable change in τ when an absorbing molecular species is placed inside the cavity. This absorption coefficient corresponds to a noise equivalent absorption coefficient (NEA) of 8.38 x 10^{-9} cm^{-1} $Hz^{-1/2}$ for 100 Hz data acquisition rate. To evaluate the minimum detection limit in terms of mixing ratio, we have utilized P(22) spectral line in the $(12^20)\leftarrow(02^20)$ transition of β-N_2O at 1265.2489 cm^{-1} with the absorption cross-section of 4.18x10^{-22} cm^2 $molecule^{-1}cm^{-1}$. The minimum detection limit of β-N_2O for this spectral line with a cavity pressure of 20 Torr was determined to be 509 ppbv (parts by billion by volume, 1 part in 10^9). If the pressure inside the optical cavity is increased further to 1 atm pressure (760 Torr) this detection limit would correspond to 13 ppbv.

5.3 Results and discussions

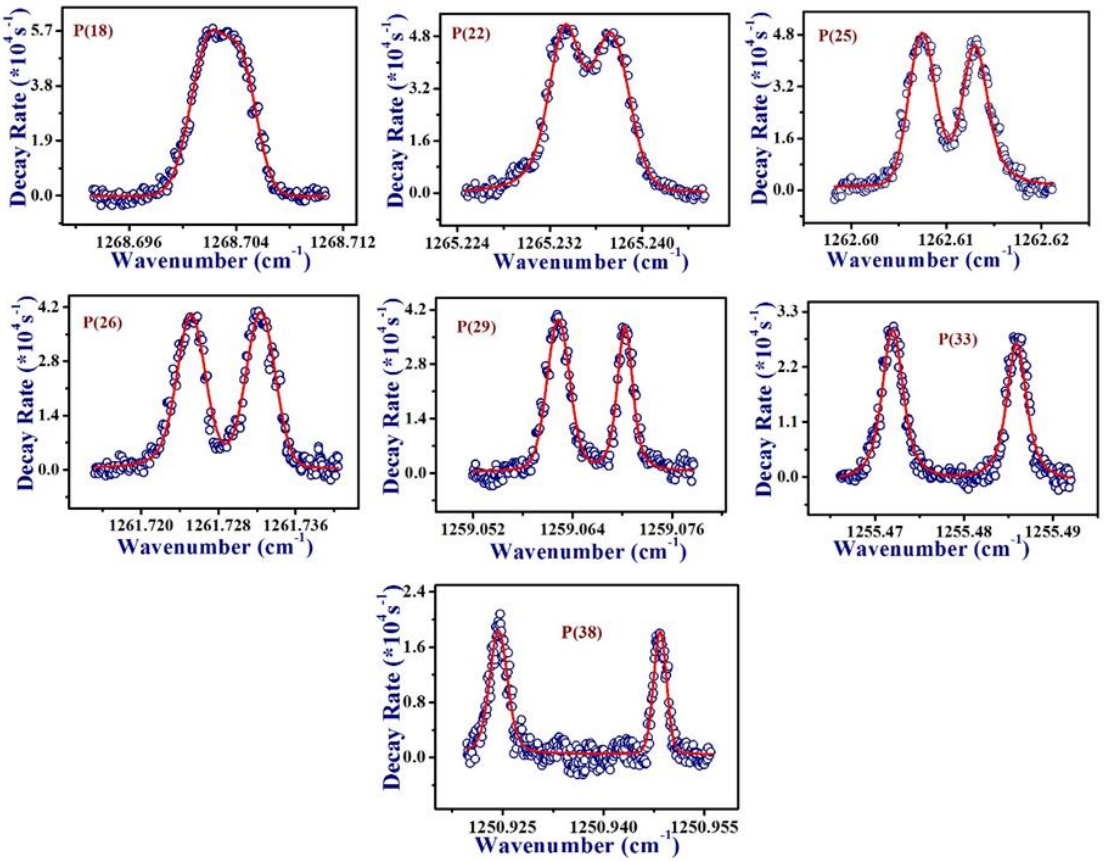

Figure 5.1: *CRDS spectra of l-type doubling of β-N2O in P branch for different J values of* $(12^20)\leftarrow(02^20)$ *transition, where first peak represents the e sub-state and second peak represents the f sub-state for each plot. Spectra were fitted with the Voigt line-shape function.*

The fine structure lines of the spectral doublets of β-N_2O acquired in the present study have very low absorption cross-sections (~10^{-22}). The high-resolution and ultra-high sensitive CRDS technique coupled with cw EC-QCL enabled us to capture those fine spectral lines. A certified calibration gas mixture of (230.0 ± 6.0) ppm of β-nitrous oxide gas (Cambridge Isotope Laboratories. Inc.) with zero-air (Air Liquid, UK) was used for this study. The high-resolution CRDS spectra were recorded with a resolution of 0.001 cm^{-1} by maintaining the cavity pressure around 1.5 Torr. We have acquired seven rotationally resolved *l*-type spectral doublets belonging to the P-branch in the $(12^20)\leftarrow(02^20)$ ro-vibrational transition in the spectral region ranging from 1250 cm^{-1} to 1269 cm^{-1}. Figure 5.1 depicts the rotational doublets of β-N_2O for

different rotational quantum numbers (J). It was clearly observed that e and f sub-states of each doublet are well-resolved except for the doublet with rotational quantum number J=18. Here, the ring-down decay rates (in s^{-1}) were plotted against wavenumbers (in cm^{-1}) to represent the CRDS spectra of l-type doublets and the spectra were fitted with the Voigt line-shape profiles. It was observed that with an increase in J value of the doublets, the spectral separation between the e and f sub-states also increased gradually. It was mentioned earlier that the l-doublet splittings with l=2 or higher are usually observed for considerably higher values of the rotational quantum numbers and this is clearly observed in our experimental findings for higher J states. We have represented all the experimentally obtained peak centres of e and f sub-states of the l-doublets and their spectral separation in Table 5.2 and subsequently the values were compared with the values obtained from the HITRAN simulation [15,16]. We found that our experimental CRDS data are in good agreement with the HITRAN simulated data.

Table 5.2: *Line positions of e and f sub-states and spectral difference between the sub-states for P branch in the $(12^20)\leftarrow(02^20)$ transition.*

J	CRDS experimental			HITRAN simulation		
	Peak Center (cm^{-1}) (Pe)	Peak Center (cm^{-1}) (Pf)	(Pf)-(Pe) (cm^{-1})	Peak Center (cm^{-1}) (Pe)	Peak Center (cm^{-1}) (Pf)	(Pf)-(Pe) (cm^{-1})
18	1268.702(1)	1268.704(5)	0.002(4)	1268.71621	1268.71846	0.00225
22	1265.233(3)	1265.237(5)	0.004(2)	1265.24895	1265.25324	0.00429
25	1262.606(2)	1262.611(9)	0.005(7)	1262.61915	1262.5820	0.00667
26	1261.725(0)	1261.732(3)	0.007(3)	1261.73696	1261.74464	0.00768
29	1259.062(2)	1259.070(4)	0.008(2)	1259.07361	1259.08505	0.01144
33	1255.470(5)	1255.486(5)	0.016(0)	1255.4832	1255.50188	0.01868
34	1254.571(0)	1254.583(7)	0.012(7)	1254.57855	1254.59953	0.02098
38	1250.924(5)	1250.948(4)	0.023(9)	1250.93162	1250.96425	0.03263

Then we plotted the doublet spacing (i.e. the spectral separation between e and f sub-states of each doublet in cm^{-1}) with the rotational quantum numbers (J) as shown in Figure 5.2. The results were then fitted with the equation 5.2 [10] to evaluate the l-type doubling constants for the chosen ro-vibrational level of β-N_2O.

$$\Delta\nu = (q' + q'')m + (q' - q'')(m^2 - 1) \quad \textbf{(5.2)}$$

Where, q' and q" are the *l*-type doubling constants for the upper and lower states, Δv is the separation between the doublets, m = -*J* for the P-branch doublets. The *l*-type doubling constants for l = 2 (Δ state) vibrational state in the $(12^20)\leftarrow(02^20)$ transition involving P-branch were found to be 2.41 x 10^{-4} cm^{-1} and 2.13 x 10^{-4} cm^{-1} for upper and lower states, respectively and these values are almost three times smaller than the values of doubling constants for the Π state (i.e. *l*=1) as shown in Table 5.3**.**

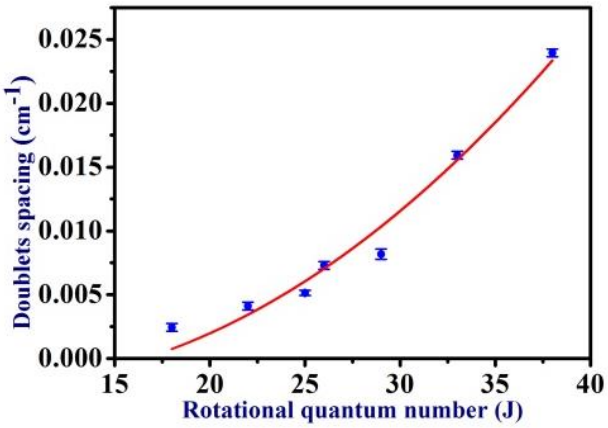

Figure 5.2: *Measurement of l-type doubling constant for l = 2 state probing ro-vibrational spectral lines of P branch in the* $(12^20)\leftarrow(02^20)$ *transition from doublet separation vs rotational quantum number plot and fitted with Eqn 5.2.*

Table 5.3: *Values of (q'+q") and (q'-q") obtained from the fitting.*

Lower state (v_1,v_2,l,v_3)	Upper state (v_1,v_2,l,v_3)	Branch	(q'+q") cm^{-1}	(q'-q") cm^{-1}
(0220)	(1220)	$P(02^20)\rightarrow(12^20)$	4.54×10^{-4}	0.28×10^{-4}
(0110)	(1110)	$P(01^10)\rightarrow(11^10)$	15.4×10^{-4}	1.26×10^{-4}

We next determined the Coriolis constants using the equation 5.3 [10].

$$q_\nu = Q_1(\nu_1 + 1) + Q_2(\nu_2 + 1) + Q_3(\nu_3 + 1) \quad \textbf{(5.3)}$$

Where Q_i are Coriolis constants, q_v is doubling constant, v_1 , v_2 , v_3 are vibrational quantum numbers of the state. We evaluated these constants from the experimentally obtained data as well as from the fitted values. From our study, the Q_i values were determined to be

$Q_1 = 0.28 \times 10^{-4}$ cm^{-1}

$Q_2 = -3.97 \times 10^{-4}$ and

$Q_3 = 1.38 \times 10^{-4}$ cm^{-1}

Next, we have evaluated the band centres, rotational constants and centrifugal distortion constants of e and f sub-states separately for the (12^20) and (02^20) vibrational levels. For this purpose, we utilized the experimentally obtained peak centres of e and f sub-states of the doublets, the rotational quantum number for upper and lower states and the angular momentum quantum number of this state. Further, we used the centrifugal distortion constant of (02^20)e & (02^20)f states from the earlier study [17]. Then we have fitted these parameters with equation 5.4 [18] to obtain the desired parameters.

$$\nu = \nu_o + B'_v[J'(J'+1) - l^2] - D'_v[J'(J'+1) - l^2]^2 - B''_v[J''(J''+1) - l^2] + D''_v[J''(J''+1) - l^2]^2 \quad \textbf{(5.4)}$$

Where, v is the peak centre, ν_o is the band centre, B'_v and B''_v are rotational constants of higher and lower states, respectively, D'_v and D''_v are centrifugal distortion constants of higher and lower states, respectively, J' and J'' are rotational quantum number for upper and lower states, respectively. The values of band centres, rotational constants and centrifugal distortion constants for the *l*-type doublets of β-N_2O are tabulated in Table 5.4**.**

Table 5.4: *Band centre, rotational constants and centrifugal distortion constants for e and f sub-states in the P-branch for $(12^20)\leftarrow(02^20)$ transition of β-N_2O. All values are given in cm^{-1}.*

Band	ν_o	B'_v	B''_v	D'_v
P $(02^20 - 12^20)$e	1283.753(9)	0.4050	0.4064	1.31×10^{-7}
P $(02^20 - 12^20)$f	1283.735(0)	0.4039	0.4064	1.48×10^{-7}

Additionally, we have performed the pressure broadening effect on the *l*-type doublets of β-N_2O at room temperature by varying the cavity pressure from 0.5-30 Torr. Initially the calibrated gas mixture was introduced into the optical cavity and then gradually the pressure of the cavity was increased by introducing zero-air upon it. Figure 5.3 illustrates a representative example of the pressure broadening effect for both e and f sub-states of P(29) doublet with a cavity pressure up to 20 Torr.

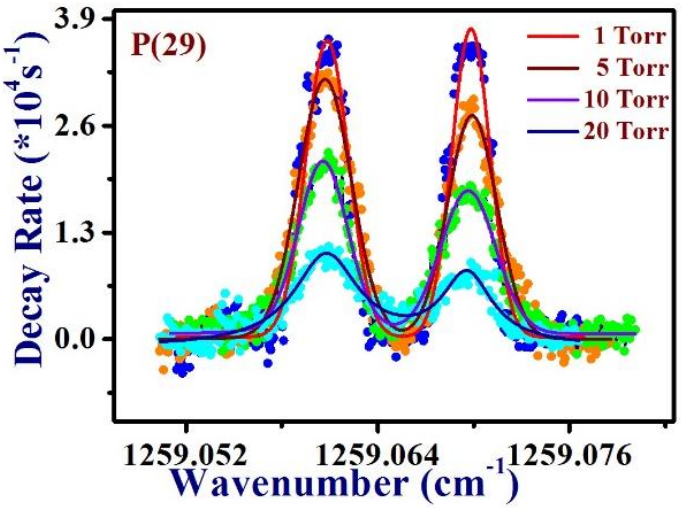

Figure 5.3: *Pressure broadening effect on P(29) spectral doublet of β-N_2O, fitted with the Voigt line-shape function.*

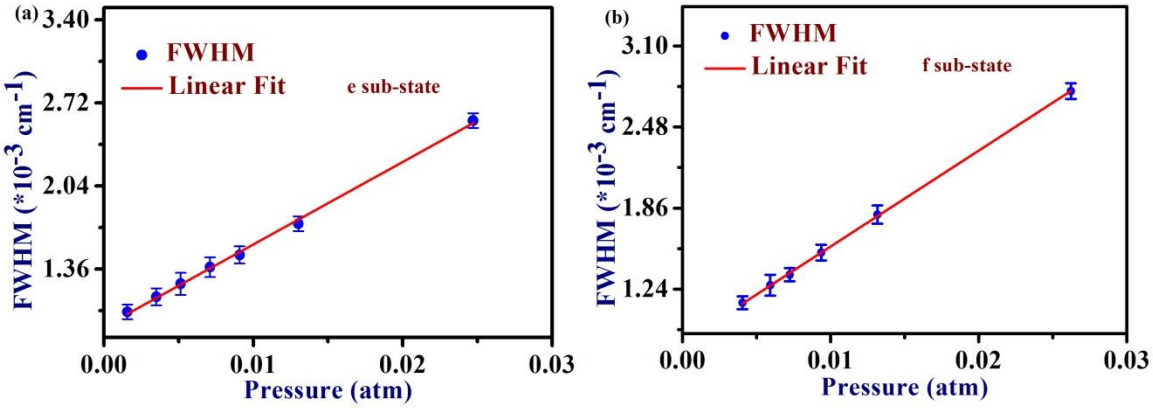

Figure 5.4: (a) and **(b)** *Linear plot between FWHM of absorption spectra and cavity pressure for e and f sub-states of* ^{15}N *β-*N_2O*, respectively, which is used to find out the pressure broadening coefficient for the respective sub-state.*

We observed that with the increase in pressure, the peak heights of the absorption features decreased gradually and spectral lines became wider. These observations suggest that the spectral measurements should be carried out at low pressure in order to obtain well-resolved *l*-doublet splittings between the e and f sub-states. Figures 5.4a and 5.4b indicate the plots between the Lorentzian full-width at half-maximum (FWHM) and cavity pressure, and it was observed that FWHM varies linearly with pressure. From the linear fits, the pressure broadening coefficients of the doublets for e and f sub-states of P(29) were determined to be γ=(0.067 ± 0.002) cm^{-1} atm^{-1} and γ=(0.075 ± 0.002) cm^{-1} atm^{-1}, respectively. We have also represented the pressure broadening coefficients of e and f sub-states for few other doublets in Table 5.5**.** The experimental values of the pressure broadening coefficients obtained by the CRDS measurements are in good agreement with the HITRAN simulated values. The values in the HITRAN database exhibit an uncertainty ranging from 5% to 10% [16]. Henceforth, we explored whether there was any dependency of pressure broadening coefficients with rotational quantum number (*J*). Figure 5.5 depicts a plot of the variation of the pressure broadening coefficients with the rotational quantum number and it was observed that the broadening coefficients decreased with the increase in J values. Upward trend of pressure broadening for e sub-state for J = 33 may be due to the slight overlapping with the spectral line (P(40)) of $^{14}N^{14}N^{16}O$ having peak centre at 1255.4736 cm^{-1} and very slight overlapping with the spectral

line (P(26)) of $^{14}N^{15}N^{16}O$ having peak centre at 1255.4453 cm^{-1} which is clearly seen from HITRAN simulated spectra. This overlapping will be more effective as we increase the pressure inside the cavity. At low pressure there will be no or very negligible overlap with the other spectral transitions. Taken together, all the new spectroscopic parameters obtained in this study by high-resolution CRDS measurements will improve our fundamental understanding of the molecular properties of β-N_2O isotopomer.

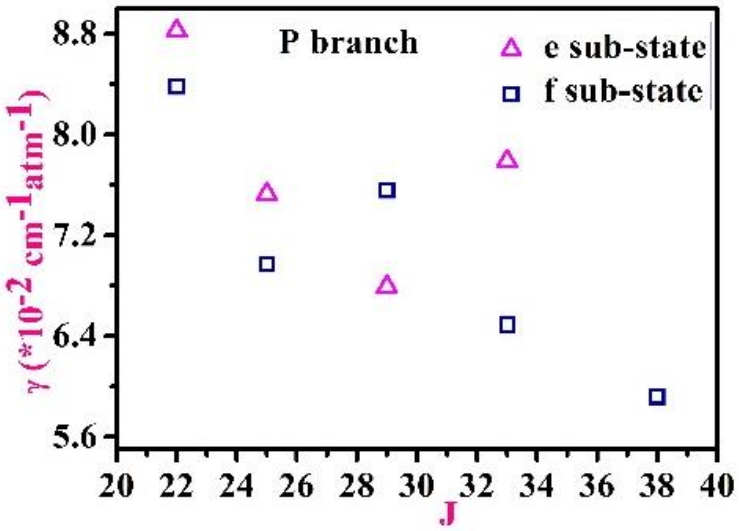

Figure 5.5: *Variation of pressure broadening coefficients with rotational quantum number for e and f sub-states.*

Table 5.5: *Represents the comparison between pressure broadening coefficients obtained from CRDS experiments and HITRAN simulation.*

Transition	Wavenumber (cm^{-1})	*J*	Pressure Broadening coefficient (cm^{-1} atm^{-1})	
			Experimental CRDS	Simulated HITRAN
P(02^20 – 12^20)e	1265.234(9)	22	0.088 ± 0.003	0.0738
	1262.604(5)	25	0.075 ± 0.002	0.0726
	1259.059(8)	29	0.067 ± 0.002	0.0713
	1255.471(6)	33	0.077 ± 0.002	0.0705
	1265.238(9)	22	0.083 ± 0.005	0.0738
	1262.610(9)	25	0.069 ± 0.005	0.0726

P(02^20 – 12^20)f	1259.069(8)	29	0.075 ± 0.002	0.0713
	1255.486(8)	33	0.064 ± 0.001	0.0705
	1250.947(2)	38	0.059 ± 0.001	0.0698

5.4 Conclusion

In summary, we have utilized the high-resolution *cw*-CRDS technique coupled with an EC-QCL light source for the measurements of *l*-type doubling of β-N_2O isotopomer for Δ state (i.e. l = 2) vibrational state. We probed the (12^20)←(02^20) ro-vibrational transition of β-N_2O to observe the fine structure splittings between the e and f sub-states in Δ vibrational state. We determined several new spectroscopic parameters of β-N_2O such as Coriolis constants, band centres, rotational constants and centrifugal distortion constants. We also performed the pressure broadening effects on the doublets at room temperature and subsequently determined the broadening coefficients of e and f sub-states to understand the pressure-induced spectral features. This investigation thus provides various new spectroscopic information of *l*-type doubling of β-N_2O leading to better fundamental understanding of the linear polyatomic molecular property.

5.5 References

[1] G. Herzberg, "*l*-type doubling in linear polyatomic molecules." *Reviews of Modern Physics*, 14.2-3, 219 (1942).

[2] H. H. Nielsen and W. H. Shaffer, "A Note Concerning *l*-Type Doubling in Linear Polyatomic Molecules." *The Journal of Chemical Physics*, 11(3), 140 (1943).

[3] C. H. Townes and A. L. Schawlow, "Microwave spectroscopy," *New York: Dover Publications*, (1975).

[4] J. Audet, D. Bastviken, M. Bundschuh, I. Buffam, A. Feckler, L. Klemedtsson, H. Laudon, S. Löfgren, S. Natchimuthu, M. Öquist, M. Peacock and M. B. Wallin,

"Forest streams are important sources for nitrous oxide emissions." *Global change biology*, 26(2), 629 (2020).

[5] M. A. K. Khalil and R. A. Rasmussen, "The global sources of nitrous oxide." *Journal of Geophysical Research: Atmospheres*, 97(D13), 14651 (1992).

[6] A. R. Ravishankara, J. S. Daniel and R. W. Portmann, "Nitrous oxide (N_2O): the dominant ozone-depleting substance emitted in the 21st century." *Science*, 326(5949), 123 (2009).

[7] R. A. Toth, "Frequencies of N_2O in the 1100 to 1440 cm^{-1} region." *JOSA B*, 3.10, 1263 (1986).

[8] R. A. Toth, "N_2O vibration–rotation parameters derived from measurements in the 900–1090-and 1580–2380-cm^{-1} regions." *JOSA B*, 4.3, 357 (1987).

[9] R. A. Toth, "Line strengths (900–3600 cm^{-1}), self-broadened linewidths, and frequency shifts (1800–2360 cm^{-1}) of N_2O." *Applied Optics*, 32.36, 7326 (1993).

[10] J. N. Shearer, T. A. Wiggins, A. H. Guenther and D. H. Rank, "*l*-Type Doubling in N_2O." *The Journal of Chemical Physics*, 25.4, 724 (1956).

[11] A. W. Mantz, K. N. Rao, L. H. Jones and R. M. Potter, "Vibration rotation bands of $^{15}N_2{}^{18}O$ effects of Fermi resonance and *l*-type doubling." *Journal of Molecular Spectroscopy*, 30.1-3, 513 (1969).

[12] B. Fabricant and J. S. Muenter, "*l*-type doubling transitions in Δ states of OCS." *Journal of Molecular Spectroscopy*, 53.1, 57 (1974).

[13] A. Maity, M. Pal, G. D. Banik, S. Maithani and M. Pradhan, "Cavity ring-down spectroscopy using an EC-QCL operating at 7.5 μm for direct monitoring of methane isotopes in air." *Laser Physics Letters,* 14.11, 115701 (2017).

[14] S. Maithani, S. Mandal, A. Maity , M. Pal and M. Pradhan, "High-resolution spectral analysis of ammonia near 6.2 μm using a cw EC-QCL coupled with cavity ring-down spectroscopy." *Analyst*, 143.9, 2109 (2018).

[15] I. E. Gordon and et al. "The HITRAN2016 molecular spectroscopic database." *Journal of Quantitative Spectroscopy and Radiative Transfer*, 203, 3 (2017).

[16] L. S. Rothman and et al "The HITRAN 2004 molecular spectroscopic database." *Journal of Quantitative Spectroscopy and Radiative Transfer*, 96, 139 (2005).

[17] C. Y. Wanga, A. W. Liua, V. I. Perevalovb, S. A. Tashkun, K. F. Songa and S. M. Hua, "High-resolution infrared spectroscopy of $^{14}N^{15}N^{16}O$ and $^{15}N^{14}N^{16}O$ in the 1200–3500 cm^{-1} region." *Journal of Molecular Spectroscopy*, 257.1, 94 (2009).

[18] G. D. Banik, S. Som, A. Maity and M. Pradhan, "Cavity ring-down spectroscopy measurements of *l*-type doubling of hot bands in Δ vibrational states of OCS near 5.2 μm." *Journal of Physics Communications,* 2.4, 045014, (2018).

Chapter: 6

Λ-doublet splittings of NO in $^2\Pi_{3/2}$ and $^2\Pi_{1/2}$ spin-split sub-bands at mid-IR

6.1 Introduction

Nitric oxide (NO) is a linear stable paramagnetic molecule as well as an important atmospheric constituent because it plays a vital role in tropospheric and stratospheric ozone chemistry [1]. This diatomic molecule has also a major role in the NO_x cycle of the lower atmosphere and interstellar chemistry [2-3]. Some major sources of NO are burning of fossil fuel, combustion of biomass and emission from agricultural lands and plants. Furthermore, NO has an important role in medical science, where it is considered as an important biomarker for monitoring inflammatory diseases of the airways like asthma and chronic obstructive pulmonary disease [4]. In view of these, an accurate knowledge of various spectroscopic properties of NO is crucial.

The ro-vibrational spectroscopy of NO presents a particularly intriguing theoretical aspect due to the presence of an unpaired electron and a non-zero nuclear spin in the nitrogen nucleus. The ground electronic state of NO is $^2\Pi$, which splits into $^2\Pi_{1/2}$ and $^2\Pi_{3/2}$ states by the spin-orbit interaction. This splitting is appearing due to two-fold degeneracy of the electronic orbital angular momentum ($\Lambda = \pm 1$) and two-fold degeneracy of the electronic spin ($\Sigma = \pm 1/2$). Finally, the projection of total angular momentum along the inter-nuclear axis is given by Ω ($\Omega = |\Sigma + \Lambda|$) which can have the values of $\Omega = 1/2$ and $\Omega = 3/2$. This is the reason that the ground state of NO splits into two states. Further, these $^2\Pi_{1/2}$ and $^2\Pi_{3/2}$ states individually get split into two sub-states with e and f components. This phenomenon is known as Λ-type doubling in the linear diatomic molecule arising due to interaction between the rotational motion and the unpaired electronic motion of the molecule [5-6]. The total parity for this e and f sub-states is represented as $+(-1)^{J-1/2}$ and $-(-1)^{J-1/2}$, respectively

[7]. However, probing the Λ-doublet splittings between e and f components in the $^2\prod_{1/2}$ and $^2\prod_{3/2}$ allowed sub-bands of NO is extremely challenging because the splitting is as low as 0.001 cm^{-1} depending on the vibrational state. This work is mainly focused on the study of Λ-type doublets in NO near 5.2 μm mid-IR region. Moreover, the recent advancements of the widely-tunable mid-infrared continuous-wave (cw) external-cavity quantum cascade lasers (EC-QCLs) with an extremely narrow line-width (~0.0001 cm^{-1}) working in the room temperature have enormous measurement capability for high-resolution spectroscopic applications [8-9]. Furthermore, when an EC-QCL is coupled with an optical cavity-enhanced absorption technique such as CRDS, it will provide ultra-sensitivity due to quantitative measurements with high-temporal and spatial-resolutions [10-11]. CRDS has already been demonstrated to be a powerful method for high-precision optical measurement of molecular absorption transitions by measuring the ring-down decay rate (rather than changes in light intensity) when light moves back and forth in a high-finesse optical cavity.

Over the past decades some experimental and theoretical spectroscopic studies have been performed on NO mostly to investigate the absolute line positions, line intensities, frequency and shape parameters of the ro-vibrational lines, Λ-type doubling and differential broadening in various overtone, combination and hot bands exploiting mainly Fourier transform infrared spectroscopy (FTIR) and photo-acoustic spectroscopy (PAS) [12-15]. But, the high-resolution experimental investigations of fine Λ-splittings between e and f components in the allowed $^2\prod_{1/2}$ and $^2\prod_{3/2}$ sub-bands of the $1 \leftarrow 0$ fundamental vibrational bands near 5.2 μm have not yet been explored in details, to the best of our knowledge. Comparisons between the present and previous works have been provided in Table 6.1. Moreover, how the fine splittings are affected in collision with various perturbing gases along with their dependence on the rotational quantum number J that are poorly understood in ro-vibrational spectra of a paramagnetic linear NO molecule in the gas-phase. Further, the high-precision measurements of the transition dipole moment and the molecular parameter such as Herman-Wallis Factor involving rotational-vibrational coupling between the e and f Λ-doublet components of NO would be interesting aspects to

gain valuable insights into the fundamental knowledge of NO spectroscopic parameters in view of various applications.

In this work, we have utilized a high-sensitive cavity ring-down spectroscopy (CRDS) technique coupled with a high-resolution cw-EC-QCL radiation source to study the fine spectroscopic properties of Λ-type doublets of NO molecule in the allowed $(^2\prod_{1/2}, 1)\leftarrow(^2\prod_{1/2}, 0)$ and $(^2\prod_{3/2}, 1)\leftarrow(^2\prod_{3/2}, 0)$ vibrational sub-band transitions in the mid-IR spectral region ranging from 1880 cm^{-1} to 1950 cm^{-1}. Exploiting the EC-QCL coupled CRDS we have measured the fine splittings between the e and f Λ-components in the R branch of the $^2\prod_{1/2}$ and $^2\prod_{3/2}$ sub-bands. The transition dipole moments, Herman-Wallis coefficients, Λ-doubling constants and their J-dependence were determined from the fine-resolved Λ splitting for both the spin-split $^2\prod_{1/2}$ and $^2\prod_{3/2}$ sub-bands of NO. Finally, we investigated the pressure broadening effects on these Λ-type doublets using zero-air (mainly O_2 + N_2), argon (Ar) and helium (He) gases as collision partners and subsequently explored how these collision-induced broadening coefficients and collisional cross-sections depend on the rotational quantum number, J.

Table 6.1: *Comparison of the present and previous works on the spectroscopic study of Λ-doublet transition of $^{14}N^{16}O$.*

Features	**C. A. Almodover et al. [17]**	**L. H. Coudert et al. [16]**	**Present Work**
Spectral Range	1887 – 1990 cm^{-1}	1700 – 2100 cm^{-1}	1880 – 1950 cm^{-1}
Method used	High-pressure, high-temperature optical cell for mid-infrared spectroscopy	Fourier transform spectroscopy	Cavity ring-down spectroscopy
Path length	21.3 cm	36.18 m	1740 m
Parameters measured	Line positions, line intensities,	Line positions, line intensities	Line positions of the ro-vibrational

	pressure induced shift and pressure broadening effect using Nitrogen and Argon	and Herman-Wallis coefficients	transitions, doublet separation, Λ-type doubling constants, transition dipole moments, Herman-Wallis coefficients, investigated pressure broadening effects on these Λ-type doublets using Zero-air, Argon (Ar) and Helium (He) gases as collision partners, collisional cross-sections and their dependence on the rotational quantum number, J.

6.2 Experimental section

All the high-resolution spectra of Λ-type doublets of NO are recorded using a high-sensitive CRDS technique coupled with an EC-QCL in the mid-IR region. The detailed experimental set-up and its optical arrangement have been described elsewhere [18-20]. In a nutshell, we have employed an EC-QCL as an optical source operating at the center wavelength λ = 5.2 μm (1923.07 cm^{-1}). This QCL is a water-cooled system emitting continuous wave (cw) light in the range of 1832 cm^{-1} - 1974

cm^{-1} with mode-hop free (MHF) tuning. It is a highly collimated laser source with high output power (~80 mW) and its extremely narrow linewidth (~0.0001 cm^{-1}) helped to resolve the fine Λ-type splittings in the allowed two sub-bands $^2\prod_{1/2}$ and $^2\prod_{3/2}$ of NO. A piezoelectric transducer (PZT) was attached to the tunable diffraction grating of the EC-QCL system for extremely fine tuning over ~ 1 cm^{-1} to acquire the fine spectral lines. The real-time wavenumber of the light emitted from the EC-QCL was continuously monitored by a wavemeter (621B-MIR; Bristol Instruments) with an accuracy of 0.002 cm^{-1}. The first order beam from an acousto-optic modulator (AOM) (IntraActionCorp; AGM-406B11M) was collimated into the high-finesse optical cavity for ring-down measurements, whereas the zeroth order beam was directed towards the wavemeter for wavelength monitoring. This high-finesse closed optical cavity was constructed with two highly reflective (HR) mirrors (R > 99.98%, CRD Optics Inc.; USA) placed 50 cm apart. The optical signal transmitted out from the cavity was detected utilizing a thermoelectrically-cooled photovoltaic mercury cadmium telluride (MCT) detector (VIGO, PVI-3TE-6). The output signal from the detector was then connected to a low-noise voltage preamplifier (SR560; Stanford Research Systems) for further amplification and filtering. Finally, the data was acquired with the help of a high-speed data acquisition card (PCI 5122, 14-bit, 100 MHz bandwidth, National Instruments) and further analysis was carried out using a custom written LabVIEW program.

6.3 Results and discussions

6.3.1 Setup parameters

We achieved an empty cavity ring-down time (RDT) τ_o = 5.8 μs with a standard deviation (1σ) of 0.68% for an averaging of 15 successive ring-down events for the present experimental conditions. Utilizing this RDT, a minimum absorption coefficient α_{min} = 3.91 X 10^{-8} cm^{-1} was achieved and subsequently the noise equivalent absorption coefficient (NEA) was determined to be 5.53 X 10^{-9} cm^{-1} $Hz^{-1/2}$. A standard calibrated NO gas (MESA Specialty Gases & Equipment, US) was used in

diluted form (40 ± 0.5) ppm for recording the high- resolution spectra of the target molecule. Signal to noise ratio depends on the empty cavity ring-down we can achieve. The higher the empty cavity ring-down time higher will the signal-to-noise ratio we obtain. In the present setup, we have obtained the empty cavity ring-down time ~ 5.8 μs. Corresponding to this ring-down time, the concentration of the sample we have used is the optimum concentration to achieve the maximum signal-to-noise ratio. Further, increasing the concentration above it will lead to saturation.

6.3.2 Λ doublet spectral lines of NO

We probed numerous Λ-type doublet spectral lines of nitric oxide belonging to the R-branch arising from the $(^2\prod_{1/2}, 1)\leftarrow(^2\prod_{1/2}, 0)$ and $(^2\prod_{3/2}, 1)\leftarrow(^2\prod_{3/2}, 0)$ vibrational transitions. The fine ro-vibrational CRDS spectra were recorded for the rotational levels J = 0.5 to J = 19.5 and J = 7.5 to J = 23.5, in the $^2\prod_{1/2}$ and $^2\prod_{3/2}$ sub-states, respectively with known sample concentrations inside the ring-down cell. The pressure inside the optical cavity was maintained at 1.0 to 5.0 Torr (1 atm = 760 Torr) depending on the experimental conditions. Few representative spectral transitions of these rotationally-resolved Λ-type doublets have been shown in Figure-1. Here, we have plotted ring-down decay-rate (k in s^{-1}) vs wavenumber (in cm^{-1}) for both the $^2\prod_{1/2}$ and $^2\prod_{3/2}$ sub-band and the spectra were fitted with the Voigt line-shape functions. Line positions of e and f sub-states in R branch for the $(^2\prod_{1/2}, 1)\leftarrow(^2\prod_{1/2}, 0)$ and $(^2\prod_{3/2}, 1)\leftarrow(^2\prod_{3/2}, 0)$ vibrational transitions obtained experimentally are represented in Table 6.2 and Table 6.3.

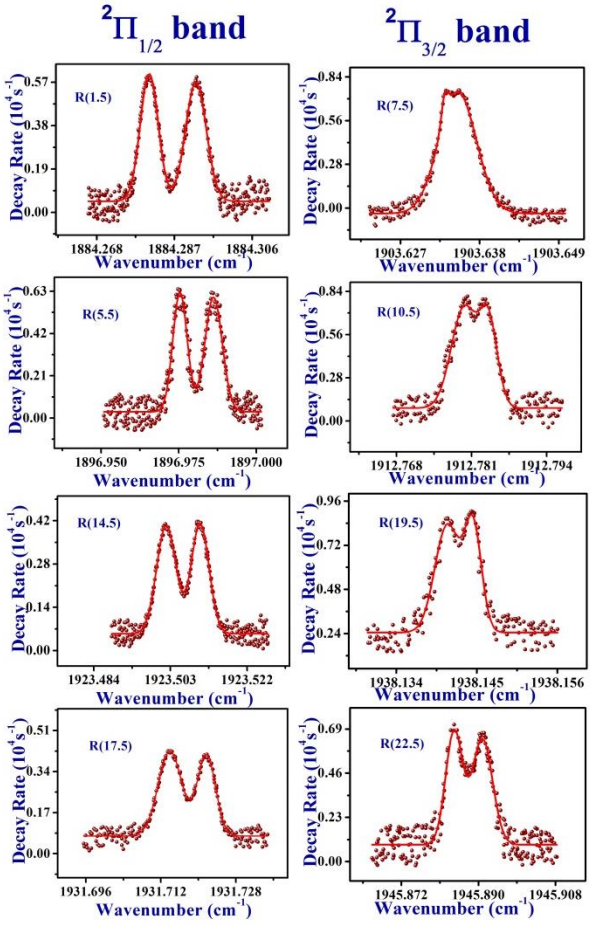

Figure 6.1: *CRDS spectra of Λ-type doublet in R-branch for* $^2\prod_{1/2}$ *and* $^2\prod_{3/2}$ *states.*

An interesting feature was observed from the recorded high-resolution R-branch spectra as depicted in Figure 6.1. We found that Λ-type doublet splittings between e and f sub-states of NO gradually decreased with increase in rotational quantum number (J) for the $^2\prod_{1/2}$ sub-band, whereas the splittings appeared to increase gradually with J for the $^2\prod_{3/2}$ sub-band. The different spin-orbit interaction results in variation of the Λ-doublet splittings with J for the two individual spin-split sub-bands where for the $^2\prod_{3/2}$ state ($\Omega = 3/2$), the electronic orbital angular momentum (Λ) and electronic spin (Σ) are in the same parity, but for the $^2\prod_{1/2}$ state ($\Omega = 1/2$) they are in opposite parity. We then measured the separations between the e and f sub-states with respective J values for the ($^2\prod_{1/2}$, 1)←($^2\prod_{1/2}$, 0) and ($^2\prod_{3/2}$, 1)←($^2\prod_{3/2}$, 0) vibrational transitions. Figure 6.2 (a,b) shows the variation of the experimentally obtained doublet separation with the corresponding J value for both the $^2\prod_{1/2}$ and $^2\prod_{3/2}$ sub-bands. The uncertainty value in the HITRAN database for line positions of

NO corresponding to these transitions varies from 0.0001 cm^{-1} to 0.001 cm^{-1} (code 4) [21]. There is a difference in the line positions observed between the present work and the HITRAN database. As in the present work, we mainly focused on the spectral difference between the e and f sub-states of the Λ-doublets and it is well matched with the HITRAN simulated value. We think this arises because we change the wavelength of the light coming out of the quantum cascade laser with the help of piezo by changing the voltage given from the piezo to the QCL. This difference observed in the absolute frequency is due to the experimental error occurring during the time of the experiment while changing the wavelength with the help of piezo.

Table 6.2: *Experimental and HITRAN simulated line positions of e and f sub-states in R branch for the* $^2\prod_{1/2}$ *band. J is the ground state rotational quantum number.*

J	$(^2\prod_{1/2}, 1) \leftarrow (^2\prod_{1/2}, 0)$			
	CRDS Experimental		HITRAN	
	Central Wavenumber (cm^{-1}) (R_e)	Central Wavenumber (cm^{-1}) (R_f)	Central Wavenumber (cm^{-1}) (R_e)	Central Wavenumber (cm^{-1}) (R_f)
0.5	1881.026(5)	1881.038(4)	1881.03403	1881.04634
1.5	1884.280(8)	1884.292(3)	1884.29279	1884.30474
2.5	1887.507(5)	1887.518(8)	1887.51705	1887.52880
3.5	1890.697(7)	1890.708(4)	1890.70696	1890.71853
4.5	1893.852(6)	1893.863(7)	1893.86252	1893.87400
5.5	1896.975(4)	1896.986(2)	1896.98369	1896.99490
6.5	1900.060(6)	1900.071(0)	1900.07042	1900.08142
7.5	1903.113(1)	1903.124(2)	1903.12265	1903.13343
8.5	1906.129(3)	1906.139(5)	1906.14029	1906.15083
9.5	1909.114(6)	1909.124(9)	1909.12324	1909.13354

10.5	1912.060(2)	1912.061(0)	1912.07141	1912.08145
11.5	1914.977(6)	1914.987(6)	1914.98468	1914.99445
13.5	1920.694(6)	1920.703(8)	1920.70601	1920.71522
14.5	1923.501(9)	1923.510(3)	1923.51379	1923.52271
15.5	1926.273(4)	1926.282(2)	1926.28611	1926.29474
16.5	1929.011(4)	1929.020(2)	1929.02281	1929.03115
17.5	1931.713(9)	1931.721(8)	1931.72373	1931.73178
18.5	1934.379(2)	1934.386(8)	1934.38869	1934.39645
19.5	1937.006(4)	1937.014(3)	1937.01752	1937.02522

Table 6.3: *Experimental and HITRAN simulated line positions of e and f sub-states in R branch for the* $^2\prod_{3/2}$ *band. J is the ground state rotational quantum number.*

J	$(^2\prod_{3/2}, 1)\leftarrow(^2\prod_{3/2}, 0)$			
	CRDS Experimental		HITRAN	
	Central Wavenumber (cm^{-1}) (R_e)	Central Wavenumber (cm^{-1}) (R_f)	Central Wavenumber (cm^{-1}) (R_e)	Central Wavenumber (cm^{-1}) (R_f)
7.5	1903.633(2)	1903.634(6)	1903.64323	1903.64421
8.5	1906.723(6)	1906.725(3)	1906.73158	1906.73277
9.5	1909.768(5)	1909.770(5)	1909.78178	1909.78321
10.5	1912.780(3)	1912.782(5)	1912.79368	1912.79353
12.5	1918.690(4)	1918.693(2)	1918.70195	1918.70413
13.5	1912.583(5)	1921.586(5)	1921.59802	1921.60048
14.5	1924.442(9)	1924.446(1)	1924.45523	1924.45796
16.5	1930.045(7)	1930.049(6)	1930.05253	1930.05581
18.5	1935.484(9)	1935.489(2)	1935.49294	1935.49677

19.5	1938.141(0)	1938.145(4)	1938.15405	1938.15816
20.5	1940.767(8)	1940.772(7)	1940.77578	1940.78016
22.5	1945.884(3)	1945.889(7)	1945.89998	1945.90489
23.5	1948.392(9)	1948.398(6)	1948.40242	1948.40759

It is observed from Table 6.2 and Table 6.3 there is a constant difference of 0.01 cm^{-1} between the peak centre obtained experimentally and that of the HITRAN peak centre. This arises because we change the wavelength of the light coming out of the quantum cascade laser with the help of piezo by changing the voltage given from the piezo to the QCL. We can calibrate the experimentally obtained line centre and we will find experimental values are overlapping with HITRAN database values upto three to four decimal places. But as we are working with the doublet spectral line so this calibration is not our major concern as it will get automatically eliminated when we take the difference of the line centres to find the separation between the doublets.

6.3.3 Variation of doublet separation with rotational quantum number

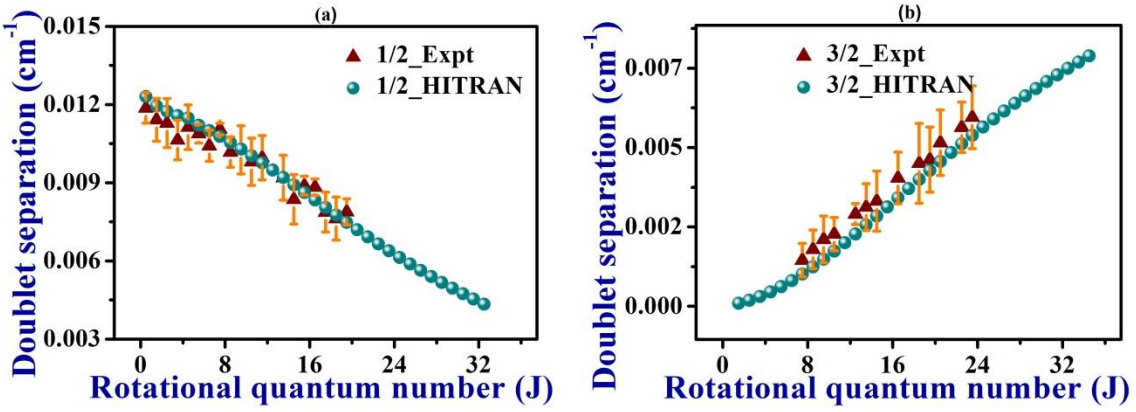

Figure 6.2: (a) & **(b)** *Plot between Λ-type doublet separation vs J for experimentally obtained and HITRAN, respectively for* $^2\prod_{1/2}$ *and* $^2\prod_{3/2}$ *states.*

The experimentally obtained doublet separations were in good agreement with the predicted values found in the HITRAN database. Subsequently, we determined the

Λ-type doubling constant using the following equation 6.1 [22] and the variations of doubling constants with respective J values have been depicted in Figure 6.3.

$$\Delta\nu = \frac{q_\Lambda}{2}\left(J+\frac{1}{2}\right)\left[\left(2+\frac{A}{B}\right)\left(1+\frac{\left(2-\frac{A}{B}\right)}{X}\right)+\frac{4\left(J+\frac{3}{2}\right)\left(J+\frac{1}{2}\right)}{X}\right] \quad \textbf{(6.1)}$$

$$X = \pm\left[\frac{A}{B}\left(\frac{A}{B}-4\right)+4\left(J+\frac{1}{2}\right)^2\right]^{\frac{1}{2}}$$

where, Δν = doublet separation, q_Λ= doubling constant, J = rotational quantum number, A = interaction constant between Λ and Σ, B = rotational constant.

It is well observed that the variation of doubling constant with respective J values has a non-linear nature (Figure 6.3). In our study, the doubling constants for the $^2\prod_{1/2}$ state vary widely in the range 10^{-6} to 10^{-4} orders with J values from 0.5 to 19.5, whereas for the $^2\prod_{3/2}$ state, the doubling constants are of the order of 10^{-5} with J values from 7.5 to 23.5. A noticeable difference in the nature of variation of the doubling constants with J values for the $^2\prod_{1/2}$ and $^2\prod_{3/2}$ states is clearly observed in our findings.

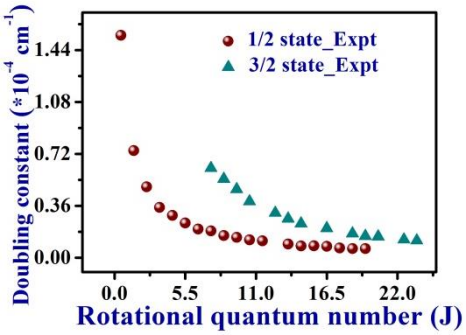

Figure 6.3: *Variation of doubling constant q_Λ with the rotational quantum number (J) for $^2\prod_{1/2}$ and $^2\prod_{3/2}$ states.*

6.3.4 Transition Dipole Moment and Herman-Wallis coefficients

Next, we have attempted to determine the vibrational transition dipole moment from the line intensities of the experimentally probed ro-vibrational spectral lines. It

is noteworthy to mention that diatomic molecules having a permanent electric dipole show variation of moment of inertia with vibrational motion of the molecule. This is known to be the major cause for the ro-vibrational perturbation of line intensity. Therefore, ro-vibrational interaction existing in molecules is capable of affecting the intensities of the absorption lines. By adopting the Herman-Wallis considerations, the influence of ro-vibrational interaction on the ro-vibrational line intensities of the molecular absorption spectra can be represented with the Herman-Wallis coefficients [23-25]. The line intensities of the individual ro-vibrational transitions were estimated from the integrated area under the curve of the respective Λ-doublets belonging to the $(^2\prod_{1/2},1)\leftarrow(^2\prod_{1/2},0)$ and $(^2\prod_{3/2},1)\leftarrow(^2\prod_{3/2},0)$ vibrational transitions. The individual absolute line strength S_{if} can be expressed by the following equation 6.2 [12].

$$S_{if} = \left(\frac{8\pi^3}{3hc}\right)\left(\frac{\nu_{if}}{Z_v Z_R}\right) 10^{-36}\mu_v^2 \, F \, S_R \exp\left(-\frac{E''}{KT}\right)\left[1 - \exp\left(-\frac{hc\nu_{if}}{KT}\right)\right] \quad \textbf{(6.2)}$$

where, ν_{if} is the central wavenumber for respective transitions in cm^{-1}, E'' is the energy of the lower state, T is the temperature, K is Boltzmann constant, S_R is the Hönl-London factor, F is the Herman-Wallis factor, μ_v is the vibrational transition dipole moment in Debye, Z_R and Z_v are the rotational and vibrational partition functions, respectively.

In the present study, all the experiments were performed at room temperature T = 296 K. The product of these two partition functions ($Z_v Z_R$) was set to 380.36 at 296 K. The energy values for each transition in Equation 6.2 were taken from the HITRAN database. The Hönl-London factor is given by $S_R = \frac{m^2 - \Omega^2}{|m|}$ where, m = J + 1 for the R-branch and m = -J for the P-branch.[2] The product of the Herman-Wallis factor and square of vibrational transition dipole moment can be re-written from the Equation 6.2 which is as follows:

$$\mu_v^2 \, F = \frac{S_{if}}{\left(\frac{8\pi^3}{3hc}\right)\left(\frac{\nu_{if}}{Z_v Z_R}\right)10^{-36} S_R \, exp\left(-\frac{E''}{KT}\right)\left[1 - exp\left(-\frac{hc\nu_{if}}{KT}\right)\right]} \quad \textbf{(6.3)}$$

Herman-Wallis factor can be expressed as a function of m as [26]:

$$\mu_v^2 \; F(m) = \; \mu_v^2 \; (1 + a * m + b * m^2 + c * m^3) \qquad \textbf{(6.4)}$$

where, a, b, c are the so-called Herman-Wallis coefficients.

Henceforth, we have utilized the Equation 6.3 to determine the product of Herman-Wallis factor and square of vibrational transition dipole moment from the observed line intensities of individual sub-states of Λ-doublet spectral lines. Subsequently, we have plotted the product of Herman-Wallis factor and square of vibrational transition dipole moment against m for the $^2\prod_{1/2}$ and $^2\prod_{3/2}$ states as shown in Figure 6.4. We have fitted the plots in Figure 6.4 with the Equation 6.4 to obtain vibrational transition dipole moment and Herman-Wallis coefficients for the $^2\prod_{1/2}$ and $^2\prod_{3/2}$ states. The values of transition dipole moments and Herman-Wallis coefficients obtained from the least-square fittings are represented in Table 6.4. We have not observed any significant difference in the values of vibrational transition dipole moment and Herman-Wallis coefficients among the two sub-bands $^2\prod_{1/2}$ and $^2\prod_{3/2}$.

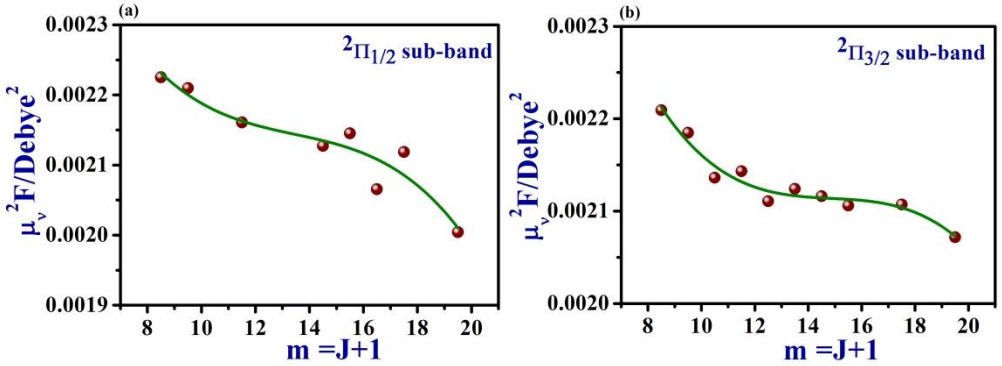

Figure 6.4: (a) & (b) *The variations of* $\mu_v^2 F$ *with m for* ($^2\prod_{1/2}$, 1)←($^2\prod_{1/2}$, 0) *and* ($^2\prod_{3/2}$, 1)←($^2\prod_{3/2}$, 0) *vibrational transitions, respectively and fitted with polynomial function (equation-6.4) to obtain the Herman-Wallis coefficients.*

Table 6.4: *Transition dipole moments and Herman-Wallis coefficients for the $^2\prod_{1/2}$ and $^2\prod_{3/2}$ states.*

Transitions	Transition Dipole Moment (μ_v/Debye)	Herman-Wallis coefficients	
		a	b
$(^2\prod_{1/2}, 1) \leftarrow (^2\prod_{1/2}, 0)$	(5.64 ± 0.11) x 10^{-2}	-0.0677	4.84 x 10^{-3}
$(^2\prod_{3/2}, 1) \leftarrow (^2\prod_{3/2}, 0)$	(5.71 ± 0.26) x 10^{-2}	-0.0706	4.72 x 10^{-3}

6.3.5 Pressure broadening coefficients and its variation with rotational quantum number

We next investigated the pressure broadening effect on the ro-vibrational lines of Λ-type doublets for the $^2\prod_{1/2}$ state in presence of various perturbing gases at room temperature. We have used zero-air, argon (Ar) and helium (He) as collision partners to understand the pressure broadening effect on the NO doublets and subsequently determined the pressure broadening coefficient, γ (in cm^{-1} atm^{-1}) for each of these perturbing gases. To study the pressure broadening effect, ro-vibrational lines of the $^2\prod_{1/2}$ state were probed at different pressures maintaining the same number of NO molecules inside the optical cavity. A specific concentration of NO molecule (40 ppm) was introduced into the cavity and then the cavity-pressure was increased gradually (from 1 to 50 Torr) by injecting the perturbing gas over it. As represented in Figure 6.5, it was observed that with increase in cavity-pressure the spectral lines corresponding to e and f sub-states of the doublet were gradually broadened and at the same time, the peak heights were observed to decrease gradually. It was found that with further increase in cavity-pressure, when an optimum pressure (~80 Torr) is reached, it would not be possible to resolve the e and f sub-states of the Λ-doublets in NO. This suggests that to observe the resolved e and

f Λ-components it is better to work at low pressures (typically 60 Torr <) for the high-resolution spectroscopic analysis of NO doublets. However, the spectra were fitted with the Voigt-line shape function. Next, from the Voigt-fitted individual spectral doublets, the Lorentzian FWHM (full width at half maximum) for e and f sub-states were determined and subsequently FWHM was plotted against the cavity-pressure from where the pressure broadening coefficients (γ) were determined for each perturbing gases. The pressure broadening coefficients (γ_e & γ_f) for different gases (zero air, Ar & He) are summarized in Table 6.5 & 6.6. We have compared the pressure broadening coefficient of NO molecule we have obtained for the perturbing gas argon with the previous work represented in Table 6.7 and Figure 6.6.

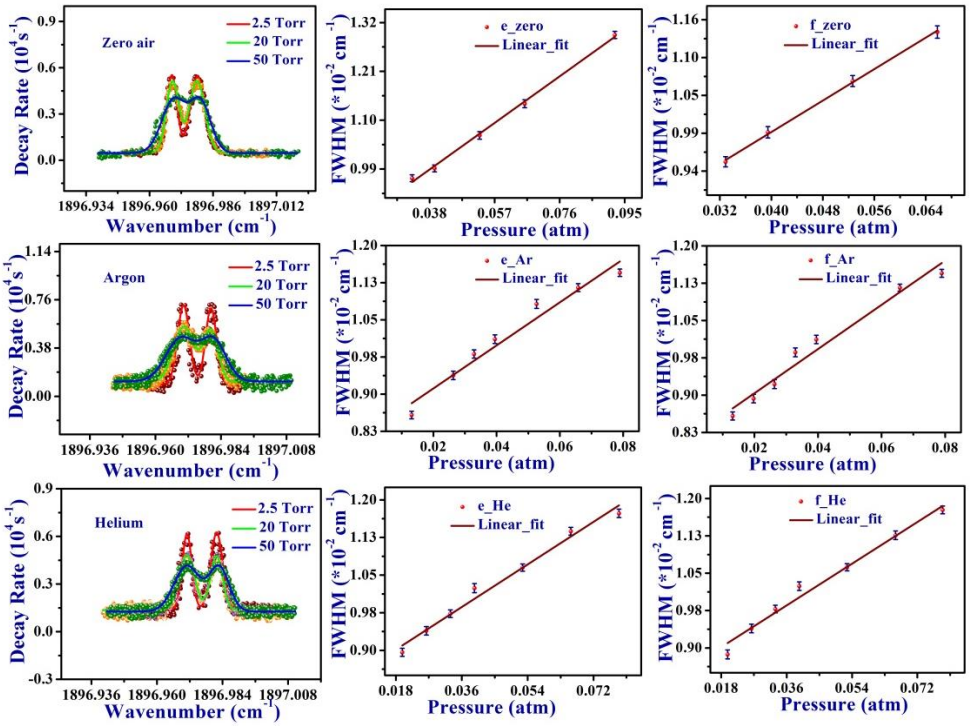

Figure 6.5: *Variation of spectral line width of R(5.5) rotational line of nitric oxide doublet for different perturbing gases (zero-air, argon and helium). Lorentzian FWHM was plotted against cavity-pressure and fitted linearly to evaluate pressure broadening coefficients (γ_e & γ_f) for e and f sub-states in the $^2\prod_{1/2}$ state.*

Table 6.5: *Experimentally obtained pressure broadening coefficients (γ_e) of NO for the e component in the $^2\prod_{1/2}$ sub-band.*

J	$(^2\prod_{1/2}, 1)\leftarrow(^2\prod_{1/2}, 0)^e$			
	Experimental peak centre (cm^{-1})	Pressure broadening coefficient (γ_e) ($cm^{-1}atm^{-1}$)		
		Zero-air	Argon	Helium
0.5	1881.026(5)	0.067 ± 0.001	0.050 ± 0.003	0.052 ± 0.001
2.5	1887.507(5)	0.065 ± 0.003	0.049 ± 0.002	0.050 ± 0.001
3.5	1890.697(7)	0.062 ± 0.002	0.047 ± 0.002	0.048 ± 0.002
4.5	1893.852(6)	0.061 ± 0.001	0.045 ± 0.002	0.047 ± 0.001
5.5	1896.975(4)	0.055 ± 0.002	0.043 ± 0.001	0.046 ± 0.001
6.5	1900.060(6)	0.056 ± 0.002	0.042 ± 0.001	0.045 ± 0.001
7.5	1903.113(1)	0.057 ± 0.002	0.042 ± 0.002	0.044 ± 0.002
8.5	1906.129(3)	0.052 ± 0.001	0.040 ± 0.001	0.043 ± 0.002

Table 6.6: *Experimentally obtained pressure broadening coefficients (γ_f) of NO for the f component in the $^2\prod_{1/2}$ sub-band.*

J	$(^2\prod_{1/2}, 1)\leftarrow(^2\prod_{1/2}, 0)^f$			
	Experimental peak centre (cm^{-1})	Pressure broadening coefficient (γ_f) ($cm^{-1}atm^{-1}$)		
		Zero-air	Argon	Helium
0.5	1881.038(4)	0.068 ± 0.003	0.050 ± 0.002	0.051 ± 0.003
2.5	1887.518(8)	0.065 ± 0.001	0.050 ± 0.002	0.050 ± 0.001
3.5	1890.708(4)	0.062 ± 0.003	0.047 ± 0.003	0.049 ± 0.002

4.5	1893.863(7)	0.060 ± 0.001	0.045 ± 0.002	0.048 ± 0.001
5.5	1896.986(2)	0.057 ± 0.001	0.044 ± 0.001	0.046 ± 0.001
6.5	1900.071(0)	0.058 ± 0.002	0.043 ± 0.002	0.045 ± 0.001
7.5	1903.124(2)	0.057 ± 0.001	0.042 ± 0.001	0.044 ± 0.002
8.5	1906.139(5)	0.055 ± 0.001	0.040 ± 0.001	0.043 ± 0.002

Table 6.7: *Comparison of pressure broadening coefficient using argon as perturbing gas between present and past work.*

J	$(^2\Pi_{1/2}, 1)\leftarrow(^2\Pi_{1/2}, 0)$			
	Pressure broadening coefficient ($cm^{-1}atm^{-1}$)			
	Argon			
	Present Work		*C. A. Almodover et al.*	
	(γ_e)	(γ_f)	($2\gamma_e$)	($2\gamma_f$)
0.5	0.050 ± 0.003	0.050 ± 0.002	-	-
2.5	0.049 ± 0.002	0.050 ± 0.002	0.0967(2.6%)	0.0991(7.9%)
3.5	0.047 ± 0.002	0.047 ± 0.003	0.0915(3.0%)	0.0924(7.8%)
4.5	0.045 ± 0.002	0.045 ± 0.002	0.0897(0.6%)	0.0904(2.8%)
5.5	0.043 ± 0.001	0.044 ± 0.001	0.0879(1.7%)	0.0884(6.5%)
6.5	0.042 ± 0.001	0.043 ± 0.002	0.0843(1.7%)	0.0852(1.9%)
7.5	0.042 ± 0.002	0.042 ± 0.001	0.0836(2.4%)	0.0848(10.9%)
8.5	0.040 ± 0.001	0.040 ± 0.001	0.0821(1.4%)	0.0838(5.3%)

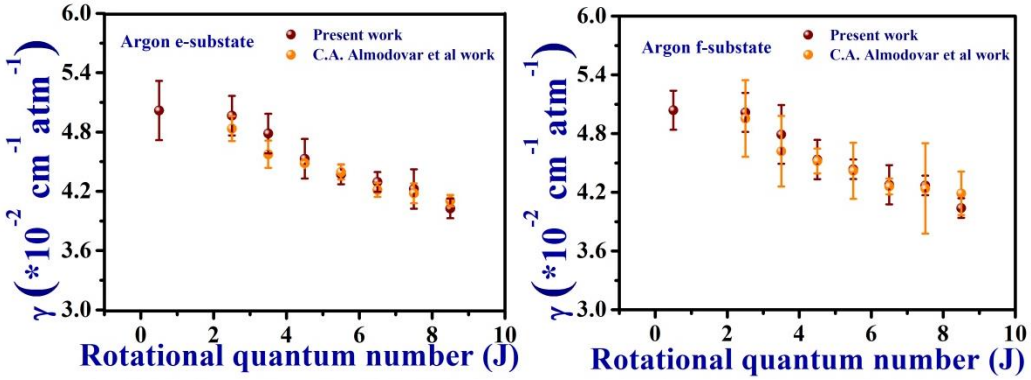

Figure 6.6: *Graphical representation for comparison of pressure broadening coefficients using argon as perturbing gas between present and past work.*

We thus investigated whether the pressure broadening coefficients (γ_e & γ_f) of the perturbing gases have any dependence on the rotational quantum number J. In order to identify this effect, we plotted the pressure broadening coefficients as a function of J and the results were shown in Figure 6.7. It was clearly observed that with increase in rotational quantum number, the pressure broadening coefficients gradually decreased irrespective of the perturbing gas used as the collision partner with NO, indicating strong dependence of γ_e and γ_f on J. This behaviour is possibly attributed to the decrease of non-adiabatic transition probability which leads to decrease in collision line-width with increasing rotational energy of absorbing molecules [27-29]. It is also noted that we observed the similar broadening coefficient for both e and f component in the studied $^2\prod_{1/2}$ sub-band within the experimental uncertainties.

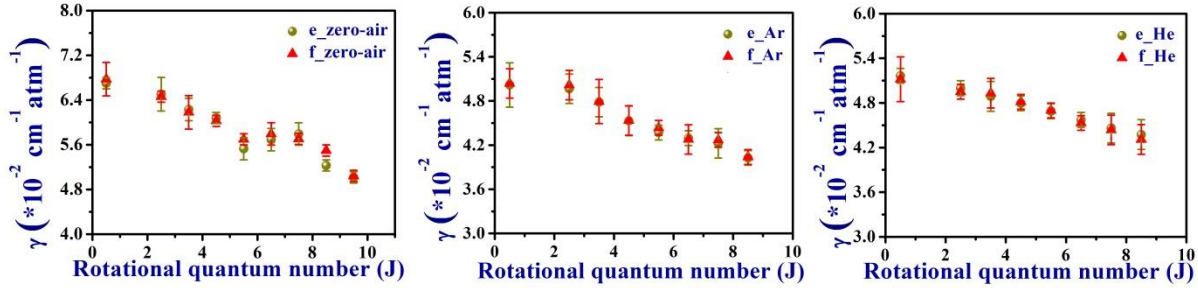

Figure 6.7: *Variation of pressure broadening coefficients (γ_e & γ_f) of e and f components of nitric oxide (NO) in the $^2\prod_{1/2}$ state with respective J value for different perturbing gases (zero-air, Argon (Ar) and Helium (He)).*

6.3.6 Variation of collisional cross-sections with rotational quantum number

Finally, to gain a deeper understanding of the rotational J-dependence of the collision-induced broadening coefficients associated with the inelastic collision mechanism in the system, we determined the collisional cross-sections (σ) for different perturbing gases using the following relation 6.5 [1]:

$$\sigma = \frac{\gamma c \pi K_B T}{<v>} \qquad \textbf{(6.5)}$$

where, γ is the pressure broadening coefficient, c the speed of light, K_B the Boltzman constant, T the temperature and <v> the average speed of the two collision partners.

The results of collision cross-section (σ) vs rotational quantum number (J) for different collision partners have been shown in Figure-8. Here, we observed a relatively weak dependence of cross-sections on the rotational quantum number for He, whereas the cross-section for Ar and zero-air exhibited strong dependence on J. These observations suggest that the mass of the perturbing molecule is one important parameter to cause various effects on the gas molecule with which we are working. These observations suggest that the lighter gas molecule (He) has no significant effect to markedly change the angular momentum of NO in contrast to the heavier gases involved in the inelastic collision mechanism because the angular momentum in the collision depends on the reduced mass of the colliding molecule pair.

Taken together, all these high-resolution spectroscopic parameters along with the fundamental information of the rotationally inelastic collisional cross-sections for the $^2\prod_{1/2}$ spin-split sub-band of NO in the mid-IR region for the v = 1 ← 0 fundamental vibrational band near 5.2 μm at room temperature laboratory conditions are important for better understanding of the molecular properties of the target molecule.

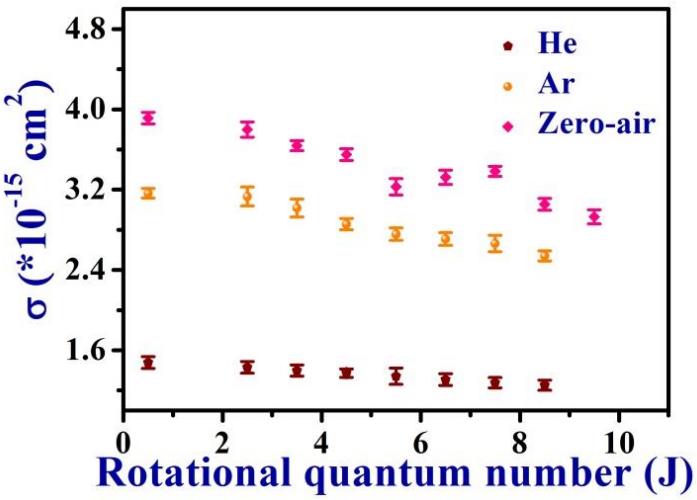

Figure 6.8: *Variation of pressure broadening collisional cross-sections (σ) vs rotational quantum number (J) for different perturbing gases.*

6.4 Conclusions

In summary, we have utilized the highly-sensitive CRDS technique coupled with the EC-QCL radiation source for studying the Λ-doublets of nitric oxide (NO) in the ($^2\prod_{1/2}$, 1)←($^2\prod_{1/2}$, 0) and ($^2\prod_{3/2}$, 1)←($^2\prod_{3/2}$, 0) vibrational transitions near 5.2 μm. We have measured the Λ-doublet splittings between the e and f sub-states of 33 ro-vibrational spectral lines in the R-branch belonging to the above mentioned transitions. The Λ-type doubling constants, Herman-Wallis coefficients and vibrational transition dipole moments were determined. Furthermore, the pressure broadening effects on the Λ-doublets of NO in collision with zero air, He and Ar as perturbing gases and their J-dependence were investigated. This is a detailed high-resolution spectroscopic study on the Λ-type doublets of NO in the fundamental ro-vibrational band via QCL coupled with CRDS. These new and high-resoluion measurements will help for better fundamental understanding of NO molecular properties and to utilize these data for various future applications in the future.

6.5 References

[1] Robert S. Pope, and Paul J. Wolf. "Rare gas pressure broadening of the NO fundamental vibrational band." *Journal of Molecular Spectroscopy,* 208, 153 (2001).

[2] M. N. Spencer, C. Chackerian, L. P. Giver, and L. R. Brown. "The nitric oxide fundamental band: frequency and shape parameters for rovibrational lines." *Journal of Molecular Spectroscopy,* 165, 506 (1994).

[3] F. Lique, F. F. S. Van Der Tak, J. Kłos, J. Bulthuis, and M. H. Alexander. "The importance of non-LTE models for the interpretation of observations of interstellar NO." *Astronomy & Astrophysics,* 493, 557 (2009).

[4] Christoph Mitscherling, Christof Maul, and Karl-Heinz Gericke. "Ultra-sensitive detection of nitric oxide isotopologues." *Physica Scripta,* 80, 048122 (2009).

[5] R. K. Hinkley, J. A. Hall, T. E. H. Walker, and W. G. Richards. "Λ doubling in 2Π states of diatomic molecules." *Journal of Physics B: Atomic and Molecular Physics (1968-1987)* 5, 204 (1972).

[6] T. E. H. Walker and W. G. Richards. "The assignment of molecular orbital configurations on the basis of Lambda-type doubling." *Journal of Physics B: Atomic and Molecular Physics,* 3, 271 (1970).

[7] F. H. Geuzebroek, M. G. Tenner, A. W. Kleyn, H. Zacharias, and S. Stotle. "Parity assignment of Λ-doublets in NO X 2Π12." *Chemical physics letters,* 187, 520 (1991).

[8] Miriam Serena Vitiello, Giacomo Scalari, Benjamin Williams, and Paolo De Natale. "Quantum cascade lasers: 20 years of challenges." *Optics express,* 23, 5167 (2015).

[9] Sanchi Maithani, Abhijit Maity, and Manik Pradhan. "Quantum cascade laser spectroscopy for atmospheric sensing and biomedical diagnostics." *Advances in Spectroscopy: Molecules to Materials*, 67 (2019).

[10] Abhijit Maity, Mithun Pal, and Manik Pradhan. “Cavity Ring-Down Spectroscopy.” *Modern Techniques of Spectroscopy*, 287 (2021).

[11] Abhijit Maity, Sanchi Maithani, and Manik Pradhan. “Cavity ring-down spectroscopy: recent technological advancements, techniques, and applications.” *Analytical Chemistry*, 93, 388 (2020)

[12] V. Dana, J. Y. Mandin, L. H. Coudert, M. Badaoui, F. Leroy, G. Guelachvili, and L. S. Rothman. “Λ-splittings and line intensities in the 2← 1 hot band of nitric oxide.” *Journal of Molecular Spectroscopy,* 165, 525 (1994).

[13] J-Y. Mandin, V. Dana, L. Régalia, A. Barbe, and X. Thomas. “Λ-splittings and line intensities in the first overtone of nitric oxide.” *Journal of molecular spectroscopy,* 185, 347 (1997).

[14] A. S Pine. “Photoacoustic measurement of differential broadening of the Λ doublets in NO (X 2Π1/2, v= 2–0) by Ar.” *The Journal of chemical physics,* 91, 2002 (1989).

[15] Thomas D. Varberg, Fred Stroh, and Kenneth M. Evenson. “Far-Infrared Rotational and Fine-Structure Transition Frequencies and Molecular Constants of 14NO and 15NO in the X2Π (v= 0) State.” *Journal of molecular spectroscopy,* 196, 5 (1999).

[16] L. H. Coudert, V. Dana, J. Y. Mandin, M. Morillonchapey, and R. Farrenq. "The spectrum of nitric oxide between 1700 and 2100 cm− 1." *Journal of Molecular Spectroscopy,* 172, 435 (1995).

[17] Christopher A. Almodovar, Wey-Wey Su, Christopher L. Strand, and Ronald K. Hanson. "R-branch line intensities and temperature-dependent line broadening and shift coefficients of the nitric oxide fundamental rovibrational band." *Journal of Quantitative Spectroscopy and Radiative Transfer,* 239, 106612 (2019).

[18] Gourab Dutta Banik, Suman Som, Abhijit Maity, Mithun Pal, Sanchi Maithani, Santanu Mandal, and Manik Pradhan. “An EC-QCL based N 2 O sensor at 5.2 µm

using cavity ring-down spectroscopy for environmental applications." *Analytical Methods,* 9, 2315 (2017).

[19] Gourab Dutta Banik, Abhijit Maity, Suman Som, Mithun Pal, and Manik Pradhan. "An external-cavity quantum cascade laser operating near 5.2 μm combined with cavity ring-down spectroscopy for multi-component chemical sensing." *Laser Physics,* 28, 045701 (2018).

[20] Abhijit Maity, Mithun Pal, Gourab Dutta Banik, Sanchi Maithani, and Manik Pradhan. "Cavity ring-down spectroscopy using an EC-QCL operating at 7.5 μm for direct monitoring of methane isotopes in air." *Laser Physics Letters,* 14, 115701 (2017).

[21] L.S. Rothman, André Barbe, D. Chris Benner, L. R. Brown, Claude Camy-Peyret, M. R. Carleer, K. Chance et al. "The HITRAN molecular spectroscopic database: edition of 2000 including updates through 2001." *Journal of Quantitative Spectroscopy and Radiative Transfer,* 82, 5 (2003).

[22] C. H. Townes and A. L. Schawlow, *Microwave spectroscopy*, (New York: Dover Publications, 1975).

[23] K. V. Kazakov, and M. A. Gorbacheva. "Calculation of higher-order approximations of the coefficients of the Herman-Wallis factor. Test for hydrogen halides." *Optics and Spectroscopy,* 106, 475 (2009).

[24] Daniele Romanini, and Kevin K. Lehmann. "Calculation of the Herman–Wallis effect in Π–Σ vibrational overtone transitions in a linear molecule: Comparison with HCN experimental results." *The Journal of chemical physics,* 105, 68 (1996).

[25] Konstantin V. Kazakov, and Andrey A. Vigasin. "Herman-Wallis factor for a molecule of type HCN." *Journal of Quantitative Spectroscopy and Radiative Transfer,* 108274 (2022).

[26] Gourab Dutta Banik, Suman Som, Abhijit Maity, and Manik Pradhan. "Cavity ring-down spectroscopy measurements of l-type doubling of hot bands in Δ

vibrational states of OCS near 5.2 μm." *Journal of Physics Communications,* 2, 045014 (2018).

[27] Stuart M. Newman, Andrew J. Orr-Ewing, David A. Newnham, and John Ballard. "Temperature and Pressure Dependence of Line Widths and Integrated Absorption Intensities for the O_2 aΔg− X3Σg-(0, 0) Transition." *The Journal of Physical Chemistry A,* 104, 9467 (2000).

[28] Robert S. Pope, Paul J. Wolf, and Glen P. Perram. "Collision broadening of rotational transitions in the O2A band by molecular perturbers." *Journal of Quantitative Spectroscopy and Radiative Transfer,* 64, 363 (2000).

[29] A. Kissel, B. Sumpf, H-D. Kronfeldt, B. A. Tikhomirov, and Yu N. Ponomarev. "Noble gas induced line-shift and line-broadening in the v_2 band of H_2S." *Journal of Molecular Structure,* 517, 477 (2000).

Chapter: 7

Development of a diode laser-based cavity-enhanced spectrometer for the detection of NO_2 levels in exhaust gas

7.1 Introduction

Nitrogen dioxide (NO_2) is an emerging pollutant in the troposphere and plays a critical role in atmospheric chemistry, contributing to tropospheric ozone layer formation, photochemical smog, and secondary aerosol production [1-3]. It is a highly reactive gas and has an active role in the production of nitrous acid (HONO) and nitric acid (HNO_3) in the atmosphere through gas-phase reactions [4-6]. Moreover, exposure to high concentrations of NO_2 can cause respiratory irritation, and long-time NO_2 exposure could also increase the risk of acute diseases, including asthma and breast cancer [7-9]. Thus, NO_2 is a key air pollutant that plays a significant role in determining the air quality and has several adverse effects on public health [8]. Anthropogenic activities like vehicular emission, fossil fuel burning, industrial and power plant emission, and biogenic activities of denitrifying bacteria are some main sources of NO_2 released into the atmosphere [10-12].

Due to its atmospheric and environmental interests and severe public health impacts, measuring actual NO_2 concentration in different locations of ambient air, such as roadside pavements, urban areas, rural areas, and indoor environments, is essential for better air quality management [13-15]. Environmental protection agencies like United State Environmental Protection Agency (USEPA) and World Health Organization (WHO) have set a 24-hour and annual permissible limit of NO_2 in ambient air are 100 ppb and 10 $\mu g/m^3$, respectively [16-18]. In addition, National Clean Air Policy (NCAP) in India was laid down in 2019 by the Ministry of Environment Forest and Climate Change (MoEF&CC) in order to set a permissible

limit for several air pollutants, which is known as National Ambient Air Quality Standard (NAAQS) [19]. According to NCAP, the maximum permissible limit for NO_2 on a 24-hour average basis is 80 $\mu g/m^3$. In this context, to maintain the permissible limits of NO_2, controlling NO_2 emissions from primary sources like vehicular emissions and power plant emissions is crucial.

Over the past decades, several methods have been developed exploiting mass spectrometry, spectroscopy and measurement using sensors in order to monitor NO_2 concentration [20-22]. Optical spectroscopic methods are believed to be more accurate over the others. Since, NO_2 remains in the atmosphere in the order of few tens of ppb levels, the highly-sensitive methods like cavity ring-down spectroscopy (CRDS), [21,23,24] Differential optical absorption spectroscopy (DOAS) [25,26] and newly-developed Incoherent broadband cavity-enhanced absorption spectroscopy (IBBCEAS) [27,28] are usually used for the measurement of NO_2. All the methods have their own advantages and disadvantages, and the methods are usually chosen as per need to the measurements as sensitivity, portability, robustness, cost of the instrument etc.

The long-path techniques for measuring NO_2 can be broadly classified into free-space and cavity-based measurements. Free space measurement technique includes DOAS, tunable diode-laser absorption spectroscopy (TDLAS) [29] and differential absorption lidar (DIAL) [30].

The most popular method among these free space measurement techniques is DOAS which uses a distant artificial continuum light source such as a high-pressure xenon lamp as a light source. The DOAS uses an open path which is efficient to detect the average concentration of the species in the atmosphere. This methodology can detect the species which have narrow absorption features. [26] However, DOAS also cannot accurately measure emitted trace gases directly from the source. In addition, the optical alignment of the apparatus is complex.

Another widely used free space measurement is TDLAS, where the long optical path length is achieved by the introduction of multipass cells like White cell, Herriot cell,

and Astigmatic cells, which usually gives optical path lengths ranging from a few meters to a few hundred of meters whereas cavity-based techniques can give path length in the order of kilometer.

CRDS method is a well-established optical method based on cavity based measurement for the detection of trace gases. Although it can accurately detect trace quantities at ppb to ppt levels with high accuracy, but its data acquisition and optical alignment are critical. Moreover, some measurements use mid-IR quantum cascade lasers (QCLs) as a light source which has narrow band-width, but at the same time, these lasers are expensive, the optical alignment in the mid-IR region is difficult and requires several high-cost optical components to develop the optical set-up [23,24].

The IBBCEAS method by Fiedler et.al [27] is another cavity-based measurement uses a broadband light source like a xenon lamp or LED, which is useful in recent times to detect trace species in the atmosphere. In this technique, the source selection plays a potential role in monitoring the type of atmospheric constituents to be measured and their limit of detection (LOD). The arrangement using a lamp requires a more significant number of optical components as well as difficult optical alignment, whereas the arrangement using LED uses a lesser number of optical components, and the setup is comparatively easy to operate. In view of these, all the optical setups require a high-acquisition time to get a proper data set, thus the methods are mostly suitable for the measurement of average concentration of the species. A simple and cost-effective measurement technique is required to capture the gas emission directly from the source and quickly measure its mixing ratios accurately. Relatively cheap and compact diode lasers with narrow bandwidth are now easily available at the visible spectral region, where NO_2 usually exhibits structured electronic transition absorption features. This kind of diode laser would be an ideal source for the development of a simple detection method for sensitive and selective measurement of NO_2 levels.

The detection limit of an instrument depends both on optical pathlength as well as absorption cross-section. Specifically, the detection limit of NO_2 for most of these

technique lies between a few tens to a few hundreds of ppb. It was noticed that in most of the cases researchers have used the continuous gas flow method through the sample cell which requires a particular accumulation time to capture the data. However, in our case, it is purely a static system and the data can be captured instantaneously. U Platt in his work stated that a detection limit of 80 ppt could be achieved with a 5 km optical pathlength in DOAS technique. Y. Yamamoto et al., utilized the cavity ring-down spectroscopy and reported the minimum detection limit of 9 ppb for 30 s integration time and subsequently measured the concentration of real samples in ppm order.

We have provided a detailed comparison between Bian et al. work [31] and the present work in Table 7.1. In the work of Bian et al., it is mentioned that the concentration is sensitive to the gas flow rates, whereas the present work is free from this effect as here the gas is in static condition inside the cavity. Our system is more flexible as we can collect the gas from any place with our gas collection system and insert that gas sample inside the cavity to detect the concentration of NO_2 present in the collected gas sample.

Table 7.1: *Comparison of the present and previous work on the cavity-enhanced spectroscopy for the detection of NO_2 molecule.*

Features	**Bian et al.** [31]	**Present Work**
Optical source	LED	Diode Laser
Wavelength region	430 nm to 450 nm	Centre at 406.5 nm with 1.2 nm linewidth
Cavity pressure	300 Torr	100 Torr
Path length	-	180 m

System type	Dynamic flow of gas through the cavity	Static
Detection limit from Allan variance at 20 s integration	6.3 ppb	1.2 ppb
Minimum concentration of NO_2 measured in a sample	35 ppm	1.9 ppm (calibrated gas mixture) 2.8 ppm (real gas sample)

In this study, we have developed a simple, robust, and precise optical method based on cavity-enhanced absorption spectroscopy. A diode laser of comparatively smaller bandwidth (~1.2 nm) operating at 406 nm was coupled to an optical cavity made of two high-reflective mirrors for high-sensitive and selective detection of NO_2 mixing ratios. We have selected an interference-free narrow absorption region for NO_2 measurement where the absorption cross-section of NO_2 is maximum. We have optically characterized the spectrometer in detail, checked the stability, and optimized, and calibrated this developed system for real sample analysis. Finally, we have utilized this developed system to measure the real-time NO_2 emissions from some vehicles and diesel generators.

7.2 Experimental setup

A schematic diagram representing our experimental setup based on cavity-enhanced absorption spectroscopy (CEAS) is depicted in Figure 7.1. We have utilized a highly collimated (< 1 mrad) diode laser (19057001-CNI Optoelectronics Tech. Co., Ltd) with a centre wavelength ~ 406.5 nm and output power of ~ 90 mW as an optical

light source. Here, a DC regulated power supply was used to operate the laser in continuous mode. The laser light was primarily passed through a combination of the polarizer (LPVISE 100-A, Thorlabs) and a quarter wave plate (QWP)(AQWP05M-600, Thorlabs) which were oriented in such a way so that it can act as an optical isolator to prevent the back reflection of light towards the laser. Then the laser beam was passed through a plano-convex lens (LA1484-A, Thorlabs). Thereafter, the laser light was precisely aligned along the central axis of the quartz coated 50 cm long optical cavity, which was formed by two high-reflective (HR) plano-concave mirrors (149645 Layertec) with manufacturer specified reflectivity of R > 99.98% for 400-800 nm and 1 m radius of curvature (ROC). Further, the transmitted light from the cavity was focused on the metal tip of optical fibre (MF11L1, Thorlabs) with the help of a plano-convex lens. Finally, the output optical signal was detected by a spectrometer (CCS-200, Thorlabs), and data were collected through the spectrometer software on a PC. A high pressure Pirani gauge (CMR 361, Pfeiffer vacuum) was connected to the optical cavity to maintain the optimum pressure inside the cavity.

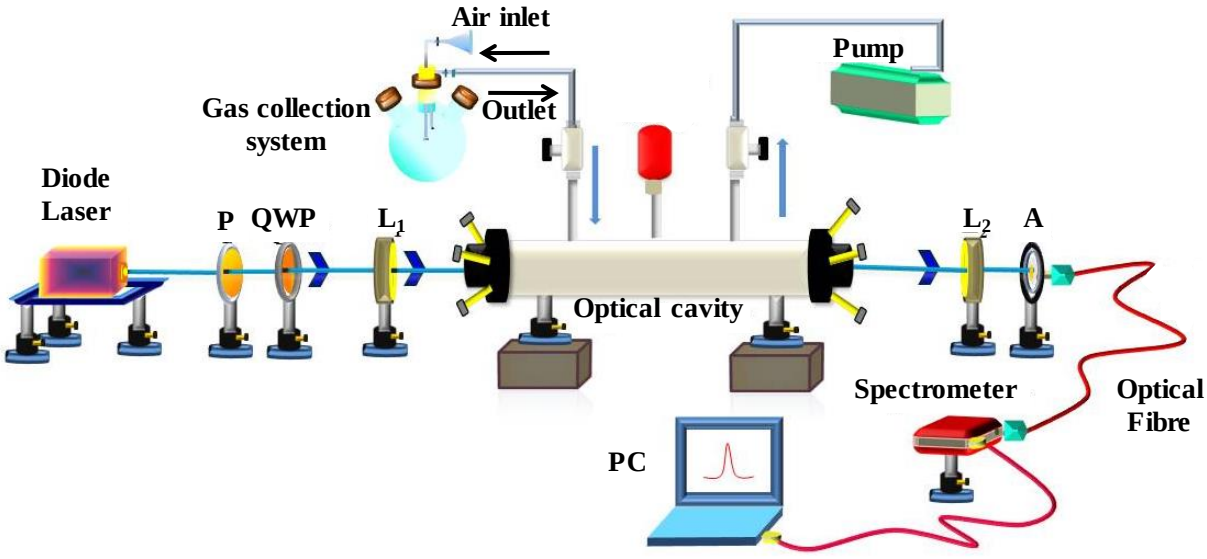

Figure 7.1: *A schematic of the CEAS setup. QWP and P are the quarter wave plate and polarizer, respectively; whereas L_1 and L_2 are the Plano-convex lenses, A is an adapter to attach the optical fibre, and PC is the personal computer.*

As the real gas samples contain particulate matter, therefore in order to remove those particles, we have designed a special gas collection arrangement using a round

bottom flask that is attached to the optical cavity. The actual photograph of the experimental setup, gas collection system, and a representative picture of real sample collection are given in Figure 7.2.

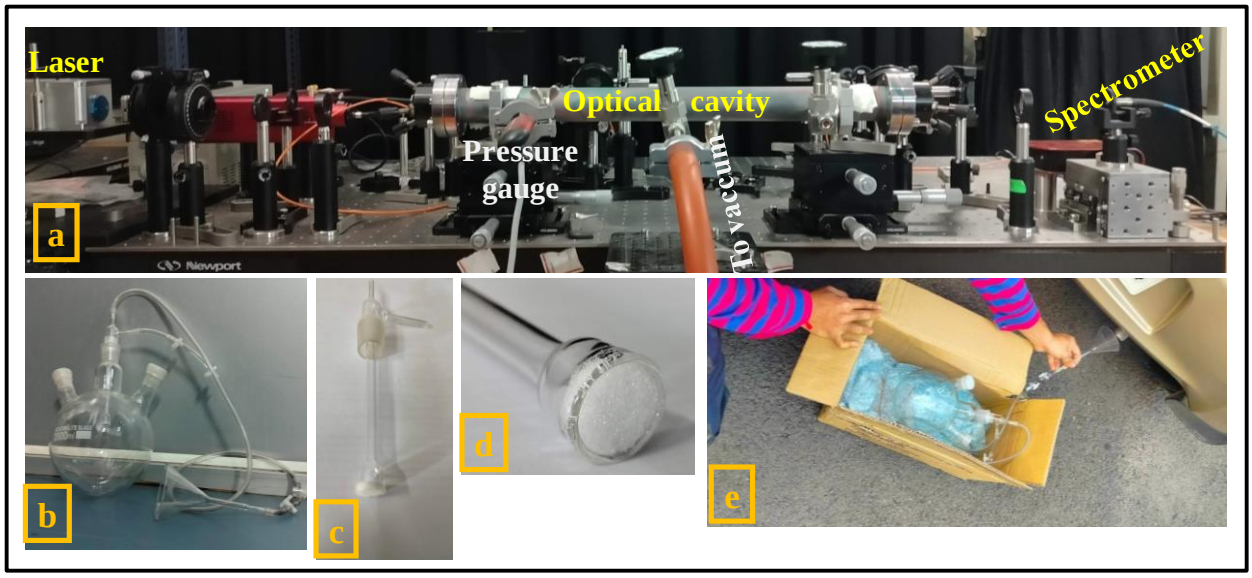

Figure 7.2: (a) *Front view of the experimental measurement setup,* **(b)** *Picture of the gas collection system,* **(c)** *Gas inlet and outlet,* **(d)** *Porcelain disk to eliminate aerosol particles,* **(e)** *Collection of the real air sample.*

7.3 Result and discussions

7.3.1 Selection of interference free spectral region for NO_2 detection

Nitrogen dioxide molecule has significant absorption in the UV-visible region ranging from 250 to 650 nm. Its maximum absorption cross-section occurs in the wavelength region of 400 nm to 410 nm, which is in the order of ~10^{-19} cm^2 $molecule^{-1}$ [32,33]. Low-cost and easily accessible handy and compact size diode lasers are available in the UV-Visible region, and these diode lasers operate in the room temperature. However, the absorption of NO_2 in the UV-visible region is comparatively broad in contrast to other spectral regions, and therefore absorption of other trace gas molecules may be possible during the measurements. We have to choose an interference-free spectral region for selective and accurate measurements

of NO_2 in ambient air. The HITRAN simulated electronic spectra of various molecules (Figure 7.3) show that NO_2 has no overlaps with different important atmospheric trace molecules significantly present in this UV-visible region. From this figure, it has been found that most of the atmospheric abundant trace gas molecules (except chlorine oxide, OClO) do not interfere with NO_2 in the 405-407 nm region. Chlorine oxides are mainly found as a disinfectant in water and dissociate easily. Therefore, the abundance of it mostly in traffic air is negligible [34]. To develop a high-sensitive compact sensor system based on CEAS for the selective and accurate detection of NO_2, we have utilized a diode laser with central wavelength~ 406.5 nm as the optical source with high optical power (90 mW) in our experiment.

Broad electronic spectra of various trace gas molecules are observed in the UV-Visible region. So, here we cannot define the spectrum of the molecule in terms of linewidth. In the UV-Visible region, we mostly know the spectral feature of the molecule in terms of variation of absorption cross-section along with the wavelength. The variation of absorption cross-section with wavelength, which we have represented in Figure 7.3 for several trace gas molecules in this UV-Visible region, clearly reflects that the spectra are broad in this region. In the mid-IR region, we observe the molecular finger prints of several trace molecules. There we obtain the sharp ro-vibrational spectral lines of individual molecules. So, in the mid-IR region we can define the absorption peak of different molecules in terms of linewidth as well as absorption cross-section. In UV-Visible region, researchers mostly work with broadband light sources like LED, Xenon lamp, supercontinuum light source etc. which has a broad range of coverage greater than or equal to 30 nm compared to those sources the diode laser which we have used as an optical source has a linewidth of 1.2 nm is very small.

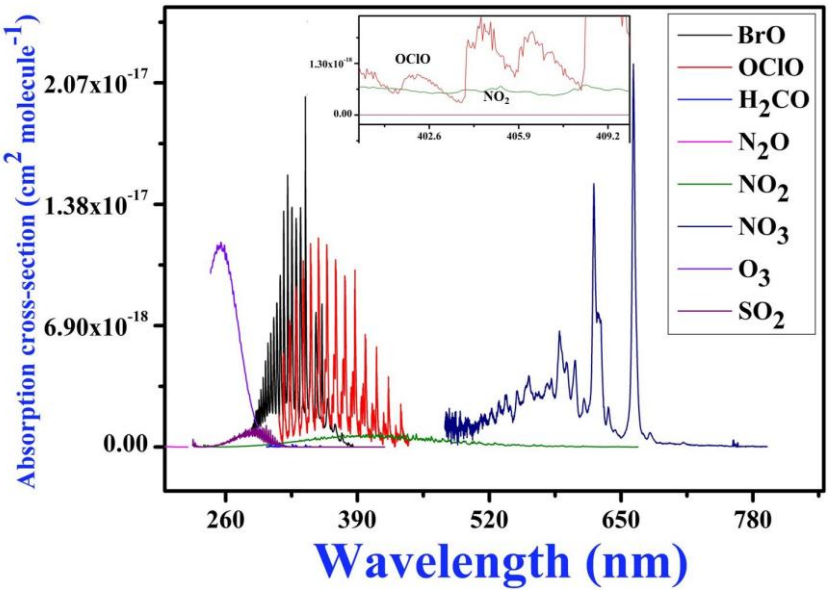

Figure 7.3: *HITRAN simulated spectra at 298 K of various trace gas molecules in the UV-Visible region.*

7.3.2 Laser profile and Allan variance analysis

We have accumulated the diode laser profile with the spectrometer, as shown in Figure 7.4a, and fitted it with a Gaussian line profile. We obtained the FWHM of the laser line ~1.2 nm. This narrow spectral feature of the laser light makes it feasible for sensitive and selective detection of NO_2 in the visible region without any interfering absorption. The precision of any optical system is usually determined using Allan variance analysis [35,36]. Here, we have employed the following equation to investigate the Allan variance:

$$\sigma^2(NO_2) = \frac{1}{2(n-1)} \sum_{i=1}^{i=n-1} (C_{NO_2}(i+1)(t) - C_{NO_2}(i)(t))^2 \quad \textbf{(7.1)}$$

where, n is the number of measurements taken, t is integration time, C_{NO_2} is the concentration of the NO_2 to be measured and $\sigma^2(NO_2)$ is the Allan variance. The square root of it yields Allan precision. Figure 7.4b shows the plot of the Allan variance versus integration time. It was observed that on successive averaging of the data, the Allan variance decreased linearly signifying the white noise region. We achieved an optimum integration time of ~240 s which corresponds to an empty

cavity light intensity for 3.9 s acquisition time. After this optimum time, further data averaging did not yield better signal-to-noise ratios because of various fluctuations. The Allan variance analysis also allows us to determine how precisely we can measure the concentration with our developed cavity-enhanced sensor system. From the Allan variance plot, the precision estimated to be ~ 0.5 ppb, suggesting that the developed system is highly capable to distinguish between two samples having concentration difference of NO_2 0.5 ppb.

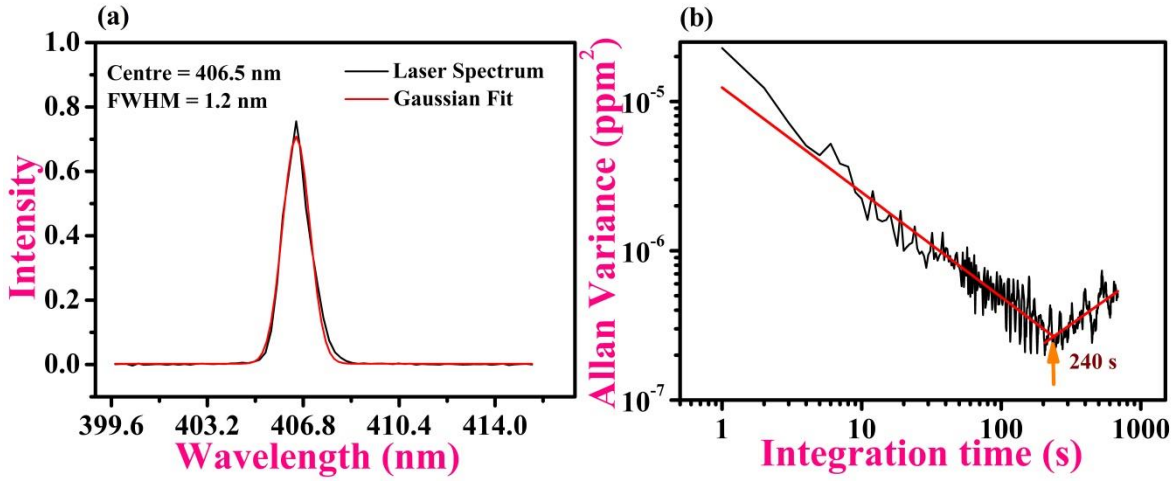

Figure 7.4: (a) *Diode laser spectra fitted with Gaussian profile depicts the centre wavelength and line width.* **(b)** *Allan variance analysis to find the stability of the developed sensor system.*

7.3.3 Measurement principle in CEAS

In this present work, we have utilized the fundamental aspect of cavity-enhanced absorption spectroscopy and coupled the diode laser radiation into a stable optical cavity. Two high- reflective mirrors were used to construct the cavity to increase the effective path length which subsequently increases the sensitivity of the sensor system. The transmitted signal was primarily captured in the absence of absorbing sample inside the cavity, and thereafter the spectra were captured introducing the absorbing sample inside the cavity. It is noteworthy to mention that with absorptions of molecular species, the scattering also plays a crucial role in the extinction of the transmitted optical signal. Two types of scattering might be relevant

in this scenario: Rayleigh and Mie. Incorporating the effects of absorption and scattering, the total absorption coefficient can be written as follows:

$$\alpha(\lambda) = \left(\frac{1-R(\lambda)}{d} + \alpha_{Ray}(\lambda) + \alpha_{Mie}(\lambda)\right) X \left(\frac{Io(\lambda)}{I(\lambda)} - 1\right) \quad \textbf{(7.2)}$$

where, d is the actual length of the cavity, $\alpha_{Ray}(\lambda)$ is the absorption coefficient for Rayleigh scattering, $\alpha_{Mie}(\lambda)$ is the absorption coefficient for Mie scattering, $I_o(\lambda)$ is the intensity when the cavity is empty and $I(\lambda)$ is the intensity when the cavity is filled with an absorbing sample. Unlike most incoherent broadband cavity-enhanced methods, which usually work under flowing conditions and thus require accumulation time, our current measurement is of static type which is focused on quick and robust measurement of the NO_2 released from primary sources. The measurement of real sample follows two steps: first, the collection of gas samples from the sources followed by measurement in a high sensitive optical cavity. During the collection of the gas samples from the sources, the emitted gas has been channelized through the porcelain disc having pore size ~5 µm in order to eliminate the particulate matters and aerosol particles from the collected gas sample which mainly gives the Mie scattering. Hence, we can drop the scattering effect coming from the Mie scattering. In our sensor system for all the measurements, we have maintained 100 Torr cavity pressure. Since the Raleigh scattering cross-section for most of the gases lies in the order of ~10^{-27} to 10^{-26} $cm^2 molecule^{-1,}$ the Raleigh scattering loss at this pressure lies in the range of ~10^{-9} to 10^{-8} cm^{-1}, whereas the cavity loss normalized by cavity length is in the order of 10^{-7} cm^{-1} [37]. Therefore, the Raleigh scattering is negligible with respect to absorption. Further, to verify it experimentally, we have captured the empty cavity spectra and spectra by introducing 99.99% pure nitrogen inside the cavity at 100 Torr cavity pressure which can tell us the effect of Rayleigh scattering in our measurement. In Figure 7.5, we have given two traces measured by our instrument, where the black trace represents the output intensity of the laser after passing through an empty cavity, and the red trace represents the output intensity of the same when the cavity is filled up by 99.99% pure nitrogen. The plots are zoomed in for better clarity, and we have not observed any significant change in intensity between an empty cavity and a cavity

filled with nitrogen gas. As nitrogen has no absorption feature in the laser region 406.5 nm, therefore we can say that there is no significant effect of Rayleigh scattering present in our experiment. Thus, the expression for the absorption coefficient in Equation 7.2 can be modified to Equation 7.3 by dropping the terms representing two types of scattering.

$$\alpha(\lambda) = \left(\frac{1-R(\lambda)}{d}\right) X \left(\frac{Io(\lambda)}{I(\lambda)} - 1\right) \quad \textbf{(7.3)}$$

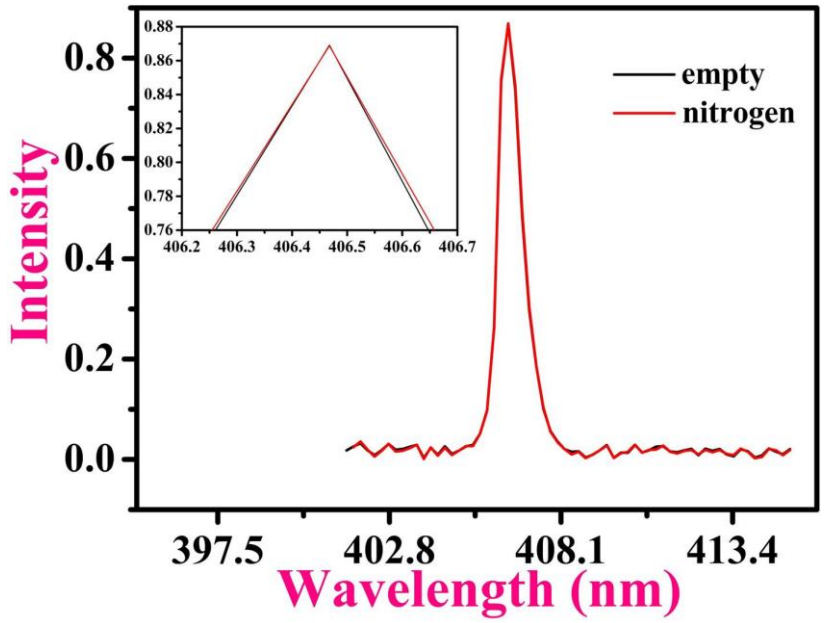

Figure 7.5: *Spectra for 100 Torr pure nitrogen inside the optical cavity.*

It is correct that particles size slightly smaller than 5 micrometers can give Mie scattering. We have used a porcelain disc with a pore size of 5 micrometers as a filter, which states that this type of filter reduces the chance of Mie scattering. However, to check interference from particulate matter below 5 micrometers, we have measured the change in intensity by inserting atmospheric air passing through the porcelain disk to the cavity maintaining 100 Torr cavity pressure, which is already shown in Figure 7.7, and the figure shows that there is no change in intensity after inserting atmospheric air sample. Also, according to the data of the live monitoring station of Central Pollution Control Board situated within 1 kilometer radius of our measurement place shows that the concentration of PM 10 is in the range of 50-100 $\mu g/m^3$ and concentration of PM 2.5 is in the range of 20-50 $\mu g/m^3$ at

the time of our measurement. Thus, it could be said that whatever the absorption we have found is mainly due to the absorption of NO_2, and the chance of Mie scattering is negligible. Another important point we want to highlight, that Mie scattering plays a significant role for the system that captures the measurement in continuous gas flow mode whereas our system works in purely static mode.

7.3.4 Minimum detection limit of nitrogen dioxide measured from the developed setup

According to the principle of cavity-enhanced detection method, every optical system must be calibrated before any measurement. The calibration of the instrument can be done either by introducing known concentration of samples thereby noting the path length and reflectivity of the mirrors or by introducing inert gases to the cavity and by noting their Rayleigh cross-section. Since, our sensor system is insensitive to Rayleigh scattering, we have calibrated our system by noting the absorption corresponding to the known samples according to the method described by previous studies [38]. We have measured the absorption of calibrated NO_2 samples which are standardized by our previously reported method [39] and subsequently, the effective optical path-length of the current setup has been measured by using the Beer-Lambert law:

$$I(\lambda) = I_o(\lambda) \exp(-\alpha L) \quad \textbf{(7.4)}$$

where, $I_o(\lambda)$ is the intensity when the cavity is empty, $I(\lambda)$ is the intensity when the cavity is filled with sample, α is the absorption coefficient, and L is the effective path length through the sample. The absorption coefficient α is related to the concentration [X] of the molecular species and absorption cross-section σ_λ as follows:

$$[X] = \frac{\alpha}{\sigma_\lambda} \quad \textbf{(7.5)}$$

The absorption cross-section of NO_2 in the laser region is 5.214×10^{-19} cm^2 $molecule^{-1}$ [32,33]. Based on these parameters, the effective path length of the present setup is found to be ~180 m and the mirror reflectivity for this laser region determined to be

~99.72%. The limiting sensitivity, i.e., the minimum absorption coefficient of the present setup, was estimated to be α_{min}= 5.57×10^{-7} cm^{-1}. A typical detection limit for NO_2 in terms of mixing ratio corresponding to this absorption cross-section at a cavity pressure of 100 Torr was determined to be ~ 327 ppb (parts per billion, 1 part in 10^9).

The detection limit of the system is limited to 327 ppb as we have mentioned above. This detection limit depends on various factors such as the reflectivity of the mirrors used to construct the cavity, optical pathlength, actual length of the cavity used, and the sensitivity of the detector. If the mirror with higher reflectivity and the cavity with greater than the actual length can be used to construct the cavity, which in turn will increase the effective optical pathlength and subsequently, we can detect the sample with a much lower concentration than 327 ppb.

7.3.5 Calibration of the developed experimental technique

As mentioned earlier, we first measured the effective optical path length of the set up. Then, we performed the calibration and determined an optimum pressure inside the cavity at which all the real samples can be accurately measured. This is done by noting the change of intensity due to the absorption of the samples with respect to mixing ratio.

We have utilized pure NO_2 gas (INTERGAS, Newfield Industrial Estate, 99.5% Grade) in diluted form to calibrate the sensor system. We first utilized a diluted NO_2 gas of 12 ppm and measured it by varying the cavity pressure from 5 to 100 Torr, as shown in Figure 7.6a. It was observed that with an increase in cavity pressure, the difference between the empty-cavity intensity and the intensity with gas sample inside the cavity gradually increases. It is observed that for the 100 Torr cavity-pressure, the intensity difference between empty cavity and the cavity filled with NO_2 gas is significant and distinguishably away from the error limit. Therefore, we optimized the developed system and subsequently performed all the experiments maintaining the cavity pressure at 100 Torr.

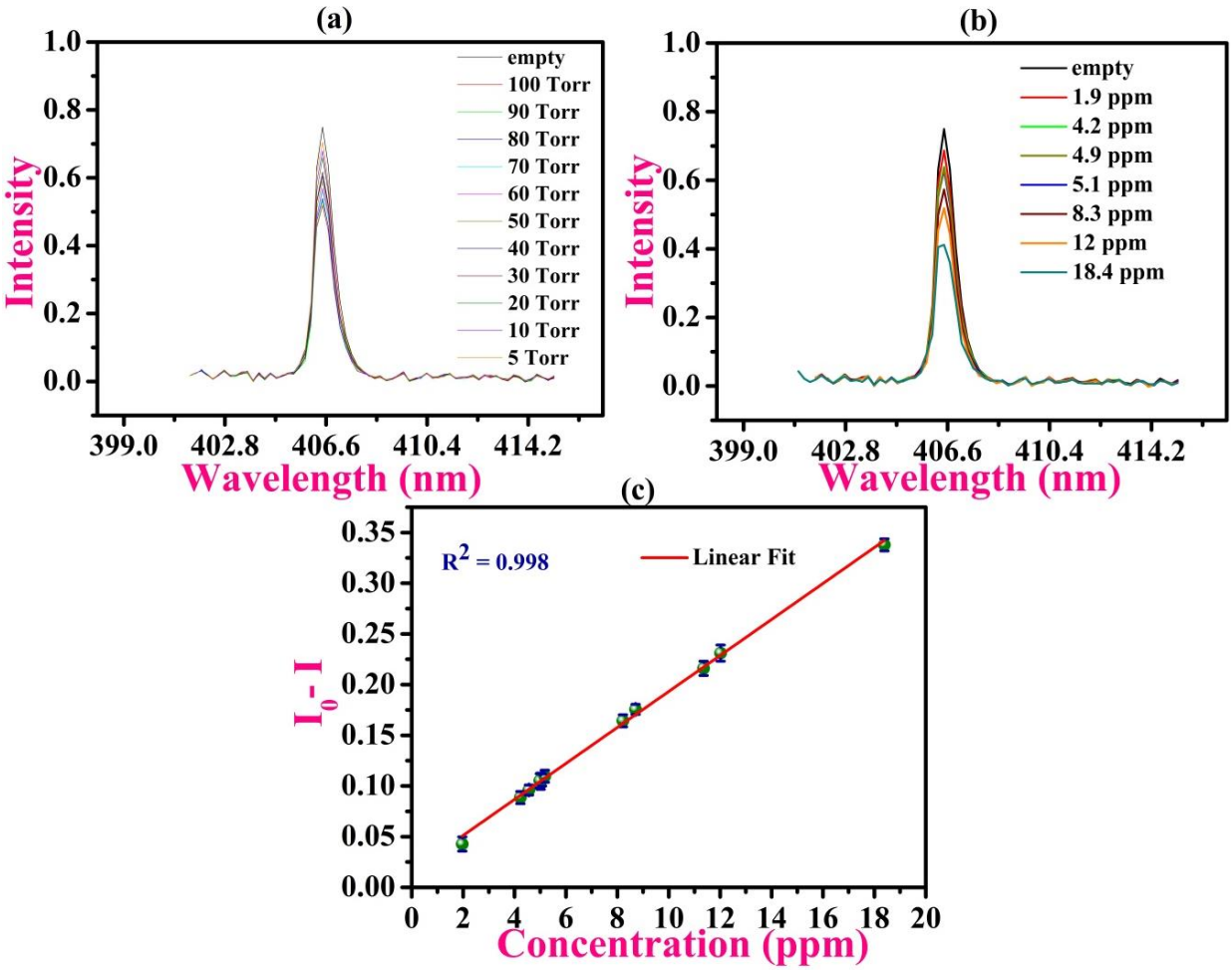

Figure 7.6: (a) *Intensity variation due to absorption at different pressure for known NO_2 gas concentration.* **(b)** *Variation of the intensity of laser spectra due to absorption for different known concentrations of NO_2 gas.* **(c)** *Calibration curve representing a linear nature between intensity differences versus different mixing ratios.*

Next, we prepared various gas mixtures of different concentrations of NO_2 and measured the change in intensity of the transmitted laser light for the respective mixtures, as shown in Figure 7.6b. Then, we have plotted the change in intensity (intensity difference between empty-cavity and filled cavity) vs concentration of NO_2, and the linear nature of the fitted curve will act as the calibration curve in our setup, as depicted in Figure 7.6c. From this curve, knowing the intensity difference of any unknown gas sample experimentally, we can accurately and quantitatively determine the trace amount of NO_2 mixing ratios present in the sample.

7.3.6 Detection of nitrogen dioxide concentration in different exhaust air samples

We have collected gas samples from various sources with the help of our specially designed gas-collection system. Then, we measured the traces of NO_2 in each sample, as shown in Figure 7.7, inside the optical cavity maintaining the 100 Torr cavity pressure. It was observed that no trace of NO_2 was detected in lab air, air from the open atmosphere, exhaled breath, and air from bike exhaust. However, within our experimental detection limit, quite a significant trace of NO_2 14 ppm was observed in the gas sample collected from car exhaust.

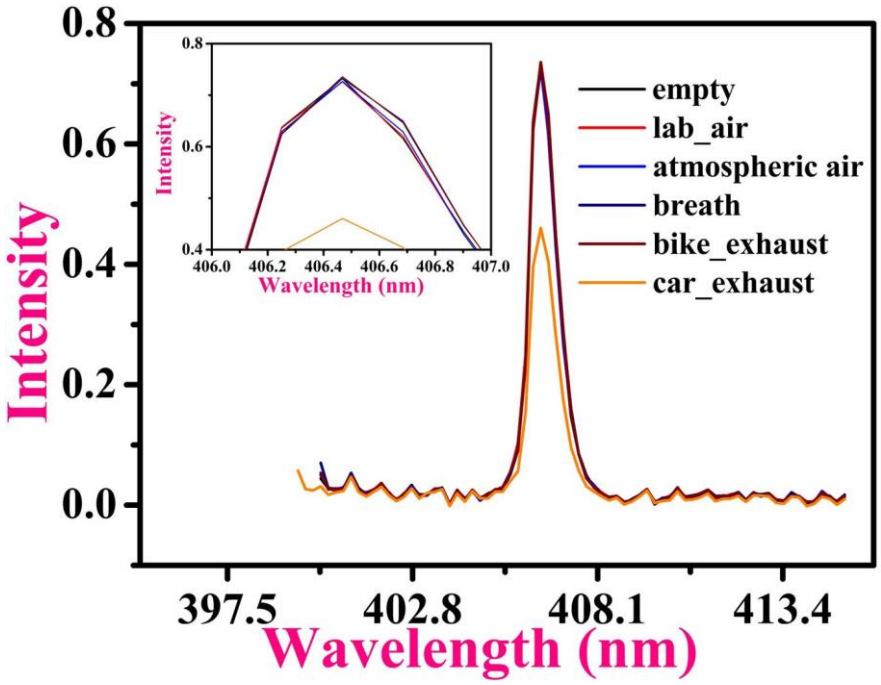

Figure 7.7: *Variation of intensity for different gas samples.*

Finally, we collected samples from vehicular emissions, i.e. (petrol and diesel vehicles) and power generator exhaust by the specially designed gas-collection system. We measured the concentration of NO_2 present in these respective gas samples by exploiting our developed sensor system, as shown in Figure 7.8. NO_2 concentrations in the exhaust gases emitted from the power generator, petrol car, and diesel car were determined to be 2.8 ppm, 10 ppm, and 14 ppm, respectively, at the heavy levels. Taken together, these studies suggest that regular monitoring of NO_2 levels coming primarily from these sources is highly desirable because people

near this type of source of NO_2 are highly exposed to the emission without knowing the concentrations.

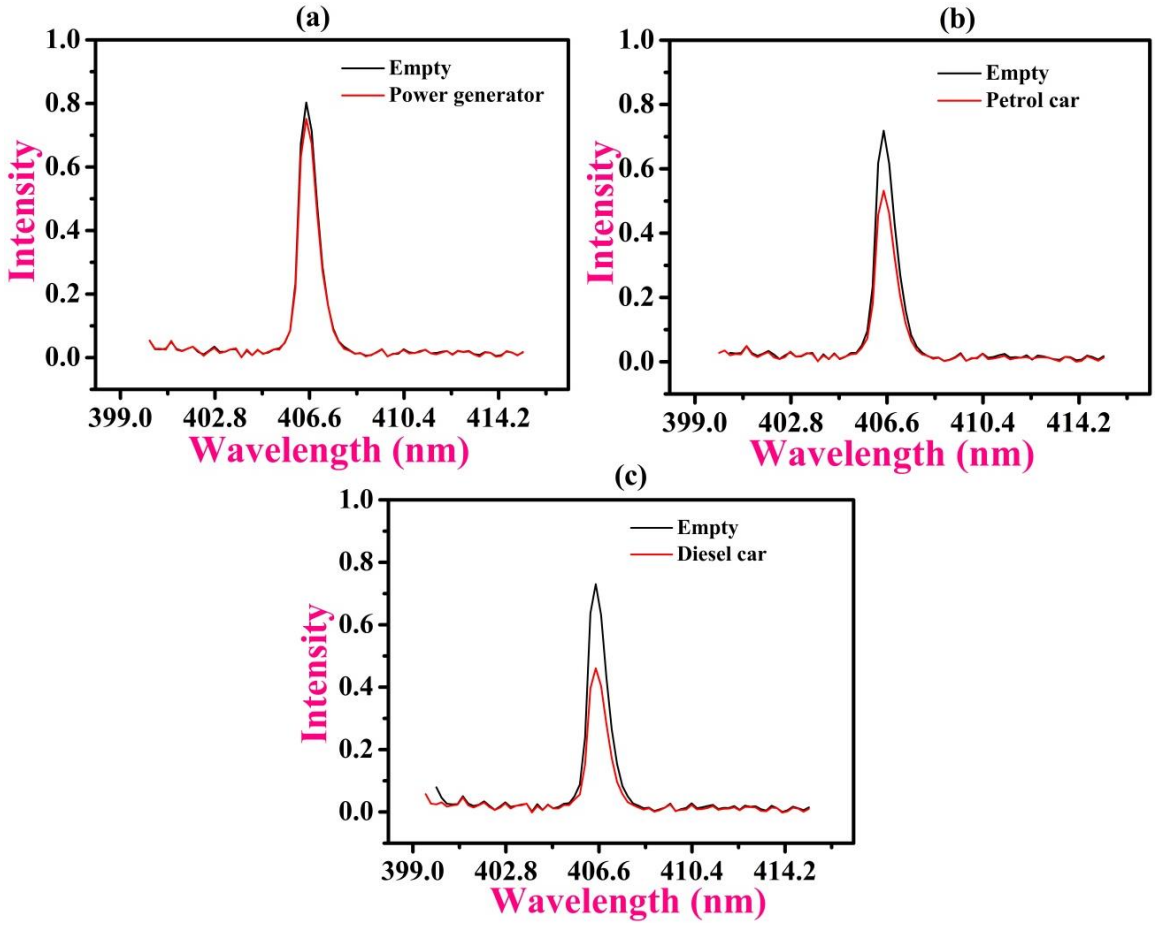

Figure 7.8: (a), (b) & (c) *Drop in intensity for gas samples collected from the power generator, petrol car, and diesel car exhaust, respectively.*

7.4 Conclusion

In summary, we have designed and developed a simple and compact optical sensor system at 406 nm vis-region for sensitive detection of NO_2 based on an optical cavity-enhanced absorption spectroscopy technique. The detection limit of 330 ppb for NO_2 was achieved with a data acquisition time of ~ 3.9 s. An effective optical path-length of 180 m was achieved within the high-finesse optical cavity. High-sensitive and selective measurement of NO_2 was demonstrated in an interference-free absorptive region and free of aerosol, indeed Rayleigh and Mie scatterings. To

check the performance of the instrument, we have utilized developed sensor for the detection of NO_2 levels in the vehicular exhaust gases. This setup can be further employed to detect several other important trace air pollutants by changing the diode laser source to other specific wavelengths of absorptions. Our observations clearly suggest that the concentration of NO_2 released from primary emission sources is higher as compared to the average permissible limits as laid down by environmental protection agencies. Consequently, a strict rule needs to be implemented so that exposure to high NO_2 concentration by people near the sources like roadside pavement and under traffic can be avoided.

7.5 References

[1] M. A. G. Demetillo, A. Navarro, K. K. Knowles, K. P. Fields, J. A. Geddes, C. R. Nowlan, S. J. Janz, L. M. Judd, J. Al-Saadi, K. Sun, B. C. McDonald, G. S. Diskin and S. E. Pusede, "Observing Nitrogen Dioxide Air Pollution Inequality Using High-Spatial-Resolution Remote Sensing Measurements in Houston, Texas." *Environmental Science & Technology,* 54, 9882 (2020).

[2] M. L. Brusseau, A. D. Matthias, A. C. Comrie and S. A. Musil, "Atmospheric Pollution." *Environmental and Pollution Science, 3rd ed.Academic Press,* Chapter 17, 293 (2019).

[3] B. J. Finlayson-Pitts and J. N. Pitts, "Applications of Atmospheric Chemistry: Air Pollution Control Strategies and Risk Assessments for Tropospheric Ozone and Associated Photochemical Oxidants, Acids, Particles, and Hazardous Air Pollutants." *Chemistry of the Upper and Lower Atmosphere, Academic Press,* Chapter 16, 871 (2000).

[4] Y. Miller, B. J. Finlayson-Pitts and R. B. Gerber, "Ionization of N_2O_4 in Contact with Water: Mechanism, Time Scales and Atmospheric Implications." *Journal of the American Chemical Society,* 131(34), 12180 (2009).

[5] H. Niki, P. D. Maker, C. M. Savage and L. P. Breitenbach, "An FTIR Study of the Reaction between Nitrogen Dioxide and Alcohols." *The International Journal of Chemical Kinetics,* 14(11), 1199 (1982).

[6] K. Mondal, S. Biswas, A. Chattopadhyay, P. Chatterjee and T. Chakraborty,"Gas-Phase Oxidation of NO_2 to HNO_3 by Phenol: Atmospheric Implications." *ACS Earth and Space Chemistry,* 5(8), 2131 (2021).

[7] E. Petersen and Z. A. Memish, "Transmission of Respiratory Tract Infections at Mass Gathering Events." *Current Opinion in Pulmonary Medicine,* 26(3), 197, (2020).

[8] H. A. Shahriyari, Y. Nikmanesh, S. Jalali, N. Tahery, A. ZhianiFard, N. Hatamzadeh, K. Zarea, M. Cheraghi and M. J. Mohammadi, "Air Pollution and Human Health Risks: Mechanisms and Clinical Manifestations of Cardiovascular and Respiratory Diseases." *Toxin Reviews,* 41(2), 606 (2022).

[9] A. Amadou, D. Praud, T. Coudon, F. Deygas, L. Grassot, M. Dubuis, E. Faure, F. Couvidat, J. Caudeville, B. Bessagnet, P. Salizzoni, K. Leffondré, J. Gulliver, G. Severi, F. R. Mancini and B. Fervers, "Long-Term Exposure to Nitrogen Dioxide Air Pollution and Breast Cancer Risk: A Nested Case-Control within the French E3N Cohort Study." *Environmental Pollution,* 317, 120719 (2023).

[10] O. V. Lozhkina and V. N. Lozhkin, "Estimation of Nitrogen Oxides Emissions from Petrol and Diesel Passenger Cars by Means of On-Board Monitoring: Effect of Vehicle Speed, Vehicle Technology,Engine Type on Emission Rates." *Transportation Research Part D: Transport and Environment,* 47, 251 (2016).

[11] H. Tian, K. Liu, J. Hao, Y. Wang, J. Gao, P. Qiu and C. Zhu, "Nitrogen Oxides Emissions from Thermal Power Plants in China: Current Status and Future Predictions." *Environmental Science & Technology,* 47, 11350 (2013).

[12] S. J. Ferguson, "Denitrification and Its Control." *Antonie van Leeuwenhoek,* 66, 89 (1994).

[13] X. Wu, T. V. Vu, R. M. Harrison, J. Yan, X. Hu, Y. Cui, A. Shi, X. Liu, Y. Shen, G. Zhang and Y. Xue, "Long-Term Characterization of Roadside Air Pollutants in Urban Beijing and Associated Public Health Implications." *Environmental Research,* 212, 113277 (2022).

[14] S. Sa, C. Clerbaux, M. George, D. Hurtmans, P. Coheur, C. Wespes, D. Loyola, P. Valks and N. Hao, "Tropospheric Ozone and Nitrogen Dioxide Measurements in Urban and Rural Regions as Seen by IASI and GOME-2." *Journal of Geophysical Research: Atmospheres,* 118, 555 (2013).

[15] H. Salonen, T. Salthammer and L. Morawska, "Human Exposure to NO_2 in School and Office Indoor Environments." *Environment International,* 130, 104887 (2019).

[16] United States Environmental Protection Agency National Ambient Air Quality Standard (NAAQS).

[17] J. A. Casquero-Vera, H. Lyamani, G. Titos, E. Borrás, F. J. Olmo, and L. Alados-Arboledas, "Impact of Primary NO_2 Emissions at Different Urban Sites Exceeding the European NO_2 Standard Limit." *Science of the Total Environment,* 646, 1117 (2019).

[18] World Health Organization (WHO) Air Quality Guideline (AQG).

[19] National Clean Air Programme (NCAP). Central Pollution Control Board. Ministryof Environmental Forests and Climate Change, The Government of India (2019).

[20] G. A. Novak, M. P. Vermeuel and T. H. Bertram, "Simultaneous Detection of Ozone and Nitrogen Dioxide by Oxygen Anion Chemical Ionization Mass Spectrometry : A Fast-Time-Response Sensor Suitable for Eddy Covariance Measurements." *Atmospheric Measurement Techniques,* 13, 1887 (2020).

[21] R. J. Wild, W. P. Dubé, K. C. Aikin, S. J. Eilerman, J. A. Neuman, J. Peischl, T. B. Ryerson and S. S. Brown, "On-Road Measurements of Vehicle NO_2/NO_xEmission Ratios in Denver, Colorado, USA." *Atmospheric Environment,* 148, 182 (2017).

[22] T. S. Singh, U. Rajak, T. N. Verma, P. Nashine, H. Mehboob, A. M. Manokar and A. Afzal, "Exhaust Emission Characteristics Study of Light and Heavy-Duty Diesel Vehicles in India." *Case Studies in Thermal Engineering,* 29**,** 101709 (2022).

[23] Y. Yamamoto, H. Sumizawa, H. Yamada and K. Tonokura, "Real-time measurement of nitrogen dioxide in vehicle exhaust gas by mid-infrared cavity ring-down spectroscopy." *Applied Physics B,* 105, 923 (2011).

[24] S. Zhou, L. Zhang, Y. Wang, N. Liu, B. Yu, and J. Li, "Measurements of Line Strengths for NO_2 near 6.2 μm Using a Quantum Cascade Laser Spectrometer." *Journal of Quantitative Spectroscopy and Radiative Transfer,* 250, 107047 (2020).

[25] J. Zou and F. Wang, "Simultaneous Measurement of SO_2 and NO_2 Concentration Using an Optical Fiber-Based LP-DOAS System." *Chinese Optics Letters,* 18(2), 1 (2020).

[26] U. Platt, "Differential Optical Absorption Spectroscopy, Air Monitoring" *Encyclopedia of Analytical Chemistry* (2006).

[27] S. E. Fiedler, G. Hoheisel, A. A. Ruth and A. Hese, "Incoherent Broad-Band Cavity-Enhanced Absorption Spectroscopy of Azulene in a Supersonic Jet." *Chemical Physics Letters,* 382, 447 (2003).

[28] A. Barbero, C. Blouzon, J. Savarino, N. Caillon, A. Dommergue, and R. Grilli, A compact incoherent broadband cavity-enhanced absorption spectrometer for trace detection of nitrogen oxides, iodine oxide and glyoxal at levels below parts per billion for field application." *Atmospheric Measurement Techniques,* 13, 4317 (2020).

[29] Y. Q. Li, K. L. Demerjian, M. S. Zahniser, D. D. Nelson, J. B. McManus, and S. C. Herndon, "Measurement of formaldehyde, nitrogen dioxide, and sulfur dioxide at Whiteface Mountain using a dual tunable diode laser system." *Journal of Geophysical Research,* 109(D16), (2004).

[30] J. Su, M. P. McCormick, M. S. Johnson, J. T. Sullivan, M. J. Newchurch, T. A. Berkoff, S. Kuang and G. P. Gronoff, "Tropospheric NO_2 measurements using a three-wavelength optical parametric oscillator differential absorption lidar." *Atmospheric Measurement Techniques,* 14, 4069 (2021).

[31] X. Bian, S. Zhou, X. Sun, B. Yu and J. Li, "Continuous measurement of NO_2 in flue gas employing cavity enhanced spectroscopy sensing system." *Measurement*, **201**, 111729 (2022).

[32] K. Moortgat and S. Tyndallt, "Absorption Cross-sections of NO_2 in the UV and Visible Region (200 – 700 nm) at 298 K." *The Journal of Photochemistry and Photobiology, A40, 195 (1987).*

[33] A. C. Vandaele, C. Hermans, S. Fally, M. Carleer, R. Colin, M. F. Merienne, A. Jenouvrier and B. Coquart, "High-resolution Fourier transform measurement of the NO_2 visible and near-infrared absorption cross section: Temperature and pressure effects." *Journal of Geophysical Research,* 107(18), 4348 (2002).

[34] T. Chen, Y. Chen, Y. Zhao and P. Chiang, "Application of Gaseous ClO_2 on Disinfection and Air Pollution Control : A Mini Review." *Aerosol and Air Quality Research,* 20(11), 2289 (2020).

[35] D. W. Allan, "Statistics of Atomic Frequency Standards." *Proceedings of the IEEE,* 54,221 (1966)**.**

[36] A. Maity, M. Pal, G. D. Banik, S. Maithani and M. Pradhan, "Cavity ring-down spectroscopy using an EC-QCL operating at 7.5 μm for direct monitoring of methane isotopes in air." *Laser Physics Letters,* 14, 115701 (2017).

[37] A. P. ShardanandRao, "Absolute Rayleigh scattering cross sectionsof gases and freons of stratospheric interest in the visible and ultraviolet regions." *NASA TN D-8442* (1977).

[38] J. Liu, X. Li, Y. Yang, H. Wang, C. Kuang, Y. Zhu, M. Chen, J. Hu, L. Zeng and Y. Zhang, "Sensitive Detection of Ambient Formaldehyde by Incoherent Broadband Cavity Enhanced Absorption Spectroscopy." *Analytical Chemistry,* 92(3), 2697 (2020).

[39] B. Panda, A. Pal and M. Pradhan, "Direct and 2f-Wavelength Modulation Spectroscopy of NO and OCS Using an Astigmatic Multipass Cell Coupled with a Mid-IR 5.2 MmCw-QCL." *Laser Physics,* 32(3), 35702 (2022).

Chapter: 8

UV-A light-induced low-energy barrier gas phase oxygen isotope exchange between carbon dioxide and nitrogen dioxide

8.1 Introduction

Carbon dioxide (CO_2) is one of the most abundant trace gas molecules in the atmosphere having lifetime of a few hundred years and plays a pivotal role in dynamic balance between anthropogenic activities and natural biogeochemical processes [1]. CO_2 exists in the atmosphere primarily in four isotopologue forms with varied natural abundances: $^{16}O^{12}C^{16}O$ (98.42%), $^{16}O^{13}C^{16}O$ (1.10%), $^{17}O^{12}C^{16}O$ (0.07%) and $^{18}O^{12}C^{16}O$ (0.39%) [2]. The oxygen isotope ratios of CO_2 in the atmosphere (i.e $^{18}O/^{16}O$ and $^{17}O/^{16}O$) are primarily influenced by hydrosphere-biosphere interactions involving the CO_2-H_2O cycles [3-7]. The oxygen isotopic compositions of atmospheric CO_2 are usually used as a powerful tracer for atmospheric monitoring, and climate control studies in addition to oceanographic and paleoclimate research [8-11]. Therefore, the measurement of oxygen isotopic signatures of CO_2 during the exchange of light ^{16}O- and heavy ^{18}O-isotopes with several other key atmospheric species such as nitrogen dioxide (NO_2) may provide important insights into the chemical transformation mechanisms, atmospheric dynamics and isotopic fractionation chemistry in the atmosphere.

In an early study, it was shown that the gas-phase ^{18}O-atom exchange takes place between an oxygen molecule ($^{16}O_2$) and doubly ^{18}O-isotope substituted CO_2 ($^{18}O^{12}C^{18}O$) molecule with an activation energy-barrier of 80 Kcal mole^{-1} in a crossed-molecular-beam-experiment [12]. This study revealed that this O-atom exchange

takes place through a weakly-bound CO_4 transition complex by adiabatic mechanism. Moreover, in the upper troposphere, the heavier ozone (O_3) isotope i.e. $^{18}O^{16}O_2$ undergoes isotopic exchange with $^{16}O^{12}C^{16}O$ to form $^{18}O^{12}C^{16}O$ in the presence of high-energy UV radiation below wavelength 305 nm via the formation of an excited state of the oxygen atom $O(^1D)$ [13].

Nitrogen dioxide (NO_2) is a significant reactive air pollutant with a lifetime of few days, co-emitted with CO_2 from common sources. It is therefore essential to understand the isotope-exchange chemical transformation mechanism occurring under available UV radiation in the troposphere [14]. To date, there is no theoretical or experimental evidences of the gas-phase O-atom isotopic exchange between $^{18}O^{12}C^{16}O$ and $N^{16}O_2$ in the presence of tropospherically available long-wave UV radiation (i.e. near-UV, so-called UV-A band) covering wavelength 320-400 nm. Moreover, the underlying isotope-exchange mechanisms involving ^{18}O-isotopic enrichments or depletions in CO_2 or NO_2 driven by UV-A radiation are presently unknown. It is also not known whether there are any intermediate transition states or what additional processes might occur in the CO_2-NO_2 isotope-exchange reaction. There is therefore a fundamental gap in the understanding of the O-atom exchange of CO_2 by NO_2 photolysis in response to near-UV radiation in the lower atmosphere.

In this study, we provide the first clear-cut experimental evidences on how the heavier ^{18}O-isotope in CO_2 is transmitted to another atmospheric NO_2 species and how these two molecular species communicate isotopically in the gas-phase in response to near-UV radiation, thus evolving an in-depth fundamental insight into the oxygen ^{16}O- and ^{18}O- isotope exchange between CO_2 and NO_2. Here, we employed a combination of high-resolution laser-based isotope-selective integrated cavity output spectroscopy (ICOS) exploiting a near-infrared (near-IR) laser source operating at 2.5 μm for precise monitoring of CO_2 isotopes and the UV-vis cavity-enhanced absorption spectroscopy at 406 nm for detection of $N^{16}O_2$ levels during the UV-A light-induced isotope-exchange experiments.

Quantum chemical calculations at the B3LYP/6311++G (d,p) level using Gaussian 16 followed by reaction modelling study suggest that the ^{18}O-atoms are transferred

from $^{18}O^{12}C^{16}O$ to $N^{16}O_2$ through an intermediate transition (TS1) complex formed by $^{18}O^{12}C^{16}O$, $N^{16}O_3$ and $N^{16}O$. This intermediate overcomes a very low-barrier of 1.67 kcal mol^{-1} transition state (TS2) and subsequently its breakdown occurs in a time scale of ~13 ns which corresponds to a rate constant of dissociation 7.64×10^7 s^{-1}. This study revealed that the near-barrierless second step increases the overall ^{18}O-isotope exchange reaction rate and the transfer of the ^{18}O-isotope from $^{18}O^{12}C^{16}O$ to $N^{16}O_2$ leads to isotopic depletion of ^{18}O in $^{18}O^{12}C^{16}O$. Our investigations mark the first-ever study of ^{18}O-isotopic exchange reaction between $^{18}O^{12}C^{16}O$ and $N^{16}O_2$, shedding a new light on this uncharted area of gas-phase isotopic photochemistry. Taken together, our findings thus open a new gas-phase mechanism driven by near-UV radiation in atmospheric chemistry and oxygen isotopic fractionations which until now has not been explored.

8.2 Experimental method

The concentration and isotope ratios of CO_2 in the gas samples were measured utilizing a CO_2 Isotope Analyzer (Loss Gatos Research, LGR, CCIA 36-EP) that exploits a laser-based high sensitive optical cavity-enhanced absorption spectroscopic method termed as off-axis integrated cavity output spectroscopy (OA-ICOS). The details of the technique have already been described elsewhere [15]. In brief, a temperature-controlled DFB diode laser source operating at ~ 2.05 μm was utilized to trace the isotopes of CO_2. This near-infrared (IR) laser source was coupled with a high-finesse closed optical cavity constructed with two highly reflective (HR) mirrors (R > 99.98%) placed ~ 59 cm apart, providing an effective optical path length of ~ 3 km. The rovibrational absorption features were probed at 4874.178 cm^{-1} and 4874.448 cm^{-1} corresponding to the $P_e(36)$ and $R_e(28)$ spectral lines of $^{18}O^{12}C^{16}O$ and $^{16}O^{12}C^{16}O$, respectively, arising from the $(2,0^0,1) \leftarrow (0,0^0,0)$ vibrational transition. The scan across this wavenumber was done by tuning the laser frequency over 20 GHz. The cavity pressure (~ 30 Torr) was maintained with the help of a diaphragm pump and solenoid valves to analyze the gas samples. The absolute concentrations of $^{16}O^{12}C^{16}O$ and $^{18}O^{12}C^{16}O$ in air samples were determined using the Beer's law by

capturing the real-time absorption spectra and then the spectra were fitted with the Voigt profile line shapes. We measured $\delta^{18}O$ values in per mill (‰) in gas samples with a typical precision of ± 0.25 ‰.

We conducted repeated experiments with air samples containing either CO_2 or mixtures of CO_2 and NO_2 with high-purity (99.99%) dry N_2 in response to the UV-A radiation to measure the isotopic changes. The gas mixtures with varying mixing ratios were taken in a cylindrical reaction chamber composed of glass measuring 15 cm in length and 5 cm in diameter, maintaining 760 Torr (1 bar) chamber pressure. Next, these samples were exposed to the UV-A radiation using three Narva UV-A lamps for 40 mins, which emit light with maximum intensity at ~375 nm. The manufacturer-supplied spectral profile is given in the Figure 8.1.

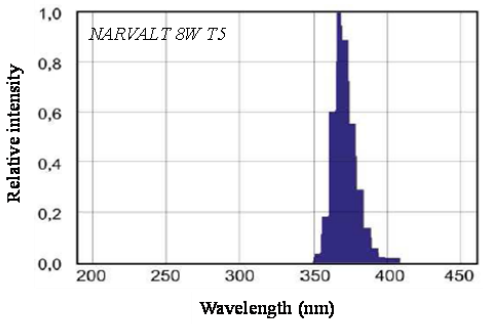

Figure 8.1: *Manufacture supplied intensity profile of the UV lamp NARVALT 8WT5*

To investigate the exchange of oxygen isotopes between $N^{16}O_2$ and $^{18}O^{12}C^{16}O$, we have recorded the concentrations of $^{16}O^{12}C^{16}O$ and $^{18}O^{12}C^{16}O$ by the ICOS technique. The total concentration of NO_2 (sum of $N^{16}O_2$ and $^{18}ON^{16}O$) was measured by our recently developed cavity-enhanced absorption spectroscopy (CEAS) technique, which traces the UV-visible absorption spectra of NO_2 at 406 nm [16]. As both isomers of NO_2 exhibit similar electronic energy levels, they result in analogous UV-visible absorption characteristic features. A snapshot of both ICOS and CEAS measurements has been given in the Figures 8.2 and 8.3 as representative examples.

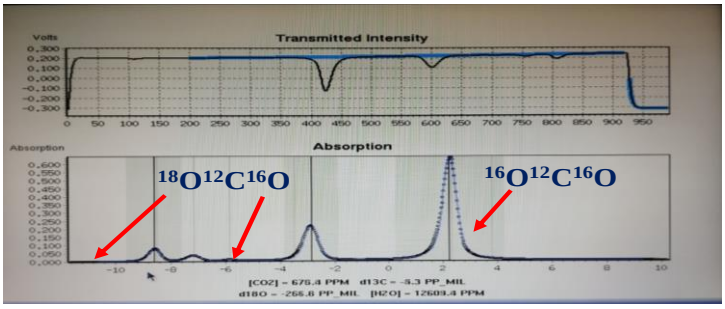

Figure 8.2: *Snapshot of the measurements of oxygen isotopes of CO2 in ICOS technique*

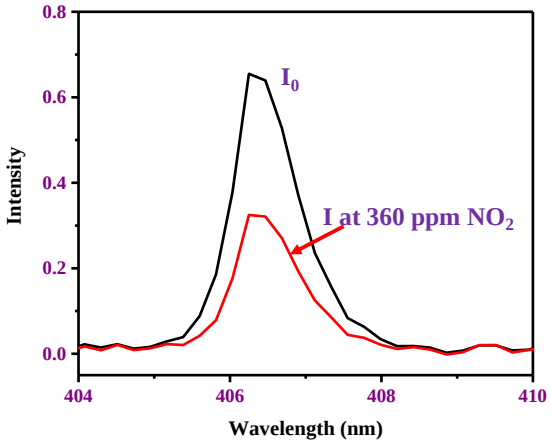

Figure 8.3: *The measurement of NO2 concentration using CEAS technique*

It is noteworthy to mention that concentrations of $^{16}O^{12}C^{16}O$ and $^{18}O^{12}C^{16}O$ are measured at the time of initiation of the reaction as well as upon its completion, whereas NO_2 concentrations are measured throughout the progression of the reaction at regular intervals of time in order to calculate photolysis rate constant of NO_2 under the UV-A irradiation. Our primary focus was to track the changes in $^{18}O^{12}C^{16}O$ and $N^{16}O_2$ concentrations continuously during the course of the experiments.

8.3 Results and discussions

8.3.1 General observation

Our initial step involved irradiating UV-A radiation on a gas mixture containing oxygen isotopes of CO_2 and then precisely monitoring the impact of UV irradiation

on the concentration of ^{16}O and ^{18}O-isotopes of CO_2. We quantified the concentration of $^{16}O^{12}C^{16}O$ in parts per million (ppm), while the concentration of $^{18}O^{12}C^{16}O$ was measured as $\delta^{18}O$ in per mill ($‰$) at the start of the reaction as well as after 40 minutes both in the presence and absence of UV irradiation. We have reported here the change in $^{18}O^{12}C^{16}O$ and $^{16}O^{12}C^{16}O$ concentrations after 40 minutes of UV irradiation. This is because the stable maximum values of $^{18}O^{12}C^{16}O$ and $\delta^{18}O$ were found after the 40 minutes as a result of the isotopic exchange. A plot of % change in $^{18}O^{12}C^{16}O/^{16}O^{12}C^{16}O$ ratio with respect to time of UV irradiation is given in the Figure 8.4**.** Here, $\delta^{18}O$ is defined as the ratio between the concentration of ^{16}O and ^{18}O-isotopes of CO_2, in a sample with respect to the ratio of the same in a standard sample Pee Dee Belemnite (PDB) i.e 0.0020672 as per equation 8.1.

$$\delta^{18}O = \left(\frac{{}^{18}O/{}_{Sample}{}^{16}O}{{}^{18}O/{}_{PDB}{}^{16}O} - 1\right) \times 1000 \qquad \textbf{(8.1)}$$

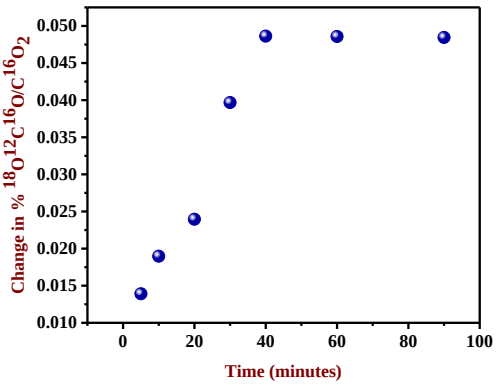

Figure 8.4: *Plot of % change in $^{18}O^{12}C^{16}O/^{16}O^{12}C^{16}O$ ratio with respect to time*

From our experiments as depicted in Figure 8.5, it has been observed that when NO_2 was not present in the mixture, the change in $^{16}O^{12}C^{16}O$ and $^{18}O^{12}C^{16}O$ isotopic concentrations over time in the presence and absence of UV radiation exhibits no significant variations. In this situation, the typical concentrations of ^{16}O and ^{18}O isotopic species of CO_2 were found to be the values in the gas samples ranging from 8-50 ppm (parts per million by volume) and 6-50 ppb (parts per billion by volume), respectively. Next, in order to assess the impact of $N^{16}O_2$ on $^{18}O^{12}C^{16}O$ under UV-A radiation available in the Earth's troposphere, we have performed the same set of experiments with adding 363 ppm of $N^{16}O_2$ to the gas sample containing $^{18}O^{12}C^{16}O$

and $^{16}O^{12}C^{16}O$. We observed a slight increase in the concentration of $^{16}O^{12}C^{16}O$ with time between the UV irradiated and unirradiated samples containing the same amount of NO_2 Figure 8.5a. But, a pronounced decrease in $^{18}O^{12}C^{16}O$ concentration was exhibited in response to UV irradiated sample containing NO_2 Figure 8.5b. This isotopically depleted $^{18}O^{12}C^{16}O$ is likely to be the effect of UV-A radiation induced ^{18}O isotope exchange between the $^{18}O^{12}C^{16}O$ and the $N^{16}O_2$ molecular species. In addition, this observation was contrary to the observed increase in $^{18}O^{12}C^{16}O$ concentration when the air sample containing same NO_2 concentration was kept into dark for same span of time. However, apart from the isotope exchange reaction, other secondary reactions may also occur in the absence of light which might be responsible for the enhancement of $^{16}O^{12}C^{16}O$ concentration more in the dark phase as compare to the UV-A light driven condition. In this context, it is noteworthy to mention here that the initial concentrations of both $^{16}O^{12}C^{16}O$ and $^{18}O^{12}C^{16}O$ in the mixture containing $N^{16}O_2$ are notably higher compared to the air samples without addition of $N^{16}O_2$. The detailed information of the initial and final concentrations of $^{16}O^{12}C^{16}O$ and $^{18}O^{12}C^{16}O$ in the presence and absence of $N^{16}O_2$ are given in the Table 8.1.

Table 8.1: *The initial and final (after 40 minutes) concentrations of $^{16}O^{12}C^{16}O$, $^{18}O^{12}C^{16}O$ and $\delta^{18}O$ values observed in different sets of experiments as N_2, N_2 + UV, N_2 + NO_2, N_2 + NO_2 + UV*

Experiment	N_2		N_2 + UV		N_2 + NO_2		N_2 + NO_2+ UV	
Time(min)	0	40	0	40	0	40	0	40
$C^{16}O_2$ (ppm)	10.83±0.02	19.05±0.01	9.56±0.03	22.82±0.02	241.75±0.02	284.28±0.03	238.23±0.02	263.78±0.03
$\delta^{18}O$ (per mill)	-918.02 ±28.24	-141.59 ±47.69	-678.30 ±45.92	-356.53 ±29.56	518.21±1.96	452.67±1.89	696.56±2.36	247.69±0.87
$^{18}O^{12}C^{16}O$ (ppb)	1.83±0.05	27.8±0.06	6.36±0.06	30.35±0.04	758.71±0.04	853.68±0.06	834.70±0.05	657.70±0.04

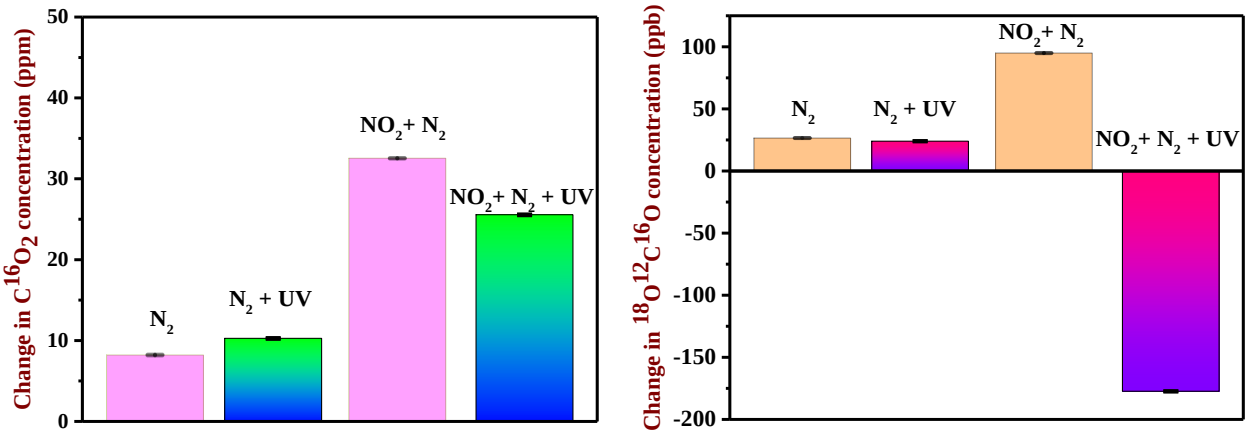

Figure 8.5: (a) *Effects of UV-A radiation in the presence and absence of* $N^{16}O_2$ *on the* ^{16}O*-oxygen isotopic distribution of* CO_2*.* **(b)** *Effects of UV-A radiation in the presence and absence of* $N^{16}O_2$ *on* ^{18}O*-oxygen isotopic distribution of* CO_2*.*

8.3.2 Investigation of the stoichiometry of the reactants in isotopic exchange

To ascertain the stoichiometry of the reactants in the isotopic reaction process, we systematically investigated the actual effect of $N^{16}O_2$ with five different concentrations ranging from100-520 ppm including [$N^{16}O_2$] = 93, 250, 363, 472 and 512 ppm. As we increase the concentration of $N^{16}O_2$, we observed a corresponding increase in the concentrations of the oxygen ^{16}O- and ^{18}O-isotopes of CO_2. It is noted that in the mixtures before subjecting the UV irradiation, the possible exchange of ^{16}O-isotopes in between $N^{16}O_2$ and $^{16}O^{12}C^{16}O$, will not show any change in $N^{16}O_2$ and $^{16}O^{12}C^{16}O$ concentrations. But, when a similar oxygen isotope-exchange reaction occurs between $N^{16}O_2$ and $^{18}O^{12}C^{16}O$, the exchange of ^{18}O remaining in $^{18}O^{12}C^{16}O$ could be replaced by ^{16}O of $N^{16}O_2$. This exchange of ^{18}O and ^{16}O results in an ^{18}O depletion in the measurements of $^{18}O^{12}C^{16}O$ concentration and consequently accounts for an increase in $^{18}ON^{16}O$ concentration.

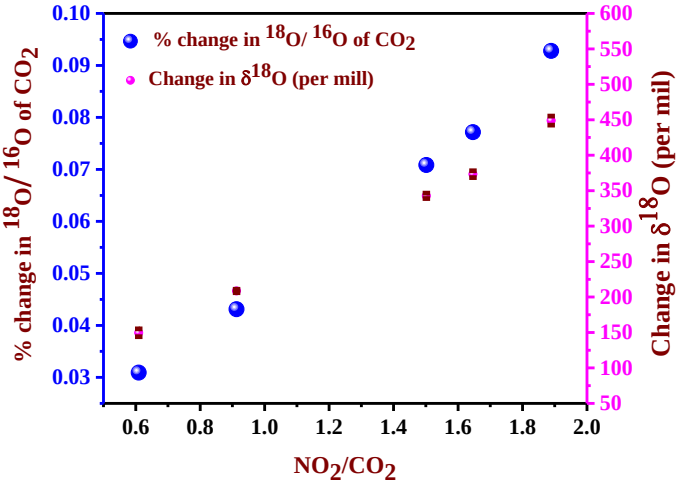

Figure 8.6: *Change in $\delta^{18}O$ values in per mil ($\%_0$) and percentage change in oxygen isotopes of CO_2 with the initial NO_2 and CO_2 ratios.*

Next, to gain more insights into the impacts of the concentration of the reactant species $N^{16}O_2$ in the ^{18}O-isotopic exchange between $^{18}O^{12}C^{16}O$ and $N^{16}O_2$, we thoroughly investigated the variation of $\delta^{18}O\%_0$ and the percentage change in $^{18}O^{12}C^{16}O/^{16}O^{12}C^{16}O$ ratio relative to the ratio of the concentrations of the reactants NO_2/CO_2 prior to the experiments as shown in Figure 8.6. From our experiment, it is clearly evident that the change in $\delta^{18}O$ $\%_0$ value is maximum when the ratio of the initial concentration of NO_2 and CO_2 is 2:1. A similar kind of trend was also observed for the percentage (%) change in $^{18}O^{12}C^{16}O/^{16}O^{12}C^{16}O$ ratios with respect to the ratios of initial concentration of NO_2 and CO_2. These findings suggest that this isotopic exchange driven by UV-A radiation is favourable in the presence of two NO_2 and one CO_2 molecules. Consequently, the stoichiometry of the isotopic exchange reaction can be expressed as $NO_2 : CO_2 = 2:1$.

8.3.3 Assessment of reaction mechanism

To unravel the underlying mechanisms of experimental findings, we next conducted a series of computational and kinetic modelling studies. Initially, we optimized the structures of the reactants, products and transition states by using the Gaussian 16 [17] software package with the density functional theory (DFT) using the B3LYP

functional and 6311++G (d,p) basis set. Following structure optimization, we calculated the rate constant of the probable steps by utilizing the kinetic and statistical thermodynamic package, the so-called KiSThelp [18] software. Subsequently, we employed a simulation package of computer program for modelling complex chemical reaction systems called Acuchem [19] to simulate the concentrations of $^{18}O^{12}C^{16}O$ based on the rate constants derived from our proposed reaction mechanism. The simulated $^{18}O^{12}C^{16}O$ concentrations after the specified reaction time for the sets with different initial concentrations of $^{18}O^{12}C^{16}O$ and $N^{16}O_2$ are then compared with our experimentally observed $^{18}O^{12}C^{16}O$ concentrations.

The crucial reaction steps for the UV-light-driven O-atom isotopic exchange reaction are illustrated in Figure 8.7a. It is well-known that nitrogen dioxide ($N^{16}O_2$) undergoes photolysis in presence of UV-A radiation (λ ~375 nm) resulting in the production of nitric oxide ($N^{16}O$) and triplet oxygen ($^{16}O(^3P)$) which subsequently reacts with $N^{16}O_2$ leading to the formation of $N^{16}O_3$. In the next step, $N^{16}O$ and $N^{16}O_3$ are combined to create a $N^{16}O_3—N^{16}O$ type of complex. We have assumed that this step involving complex formation is barrierless because in this case the overall energy is decreased upon complex formation. The structure of the $N^{16}O_3—N^{16}O$ complex resembles that of the asymmetric dimer of nitrogen dioxide i.e., $ONONO_2$ which is believed to be a key intermediate in most of the reactions between NO_2 and compounds containing O—H group like water, alcohol, phenol etc. [20,21]. In the course of the isotope exchange reaction, the $N^{16}O_3—N^{16}O$ complex first binds with $^{18}O^{12}C^{16}O$ through bond formation between the ^{16}O-atom of $N^{16}O_3$ moiety and the ^{12}C-atom of $^{18}O^{12}C^{16}O$. After the formation of ^{16}ON-^{18}O-$^{12}C(^{16}O)$-^{16}O-$N(^{16}O_2)$ complex, it undergoes dissociation by breaking ^{18}O-^{12}C and ^{16}O-N bonds of the complex to form $^{16}O^{12}C^{16}O$, $N^{16}O_2$ and $^{18}ON^{16}O$.

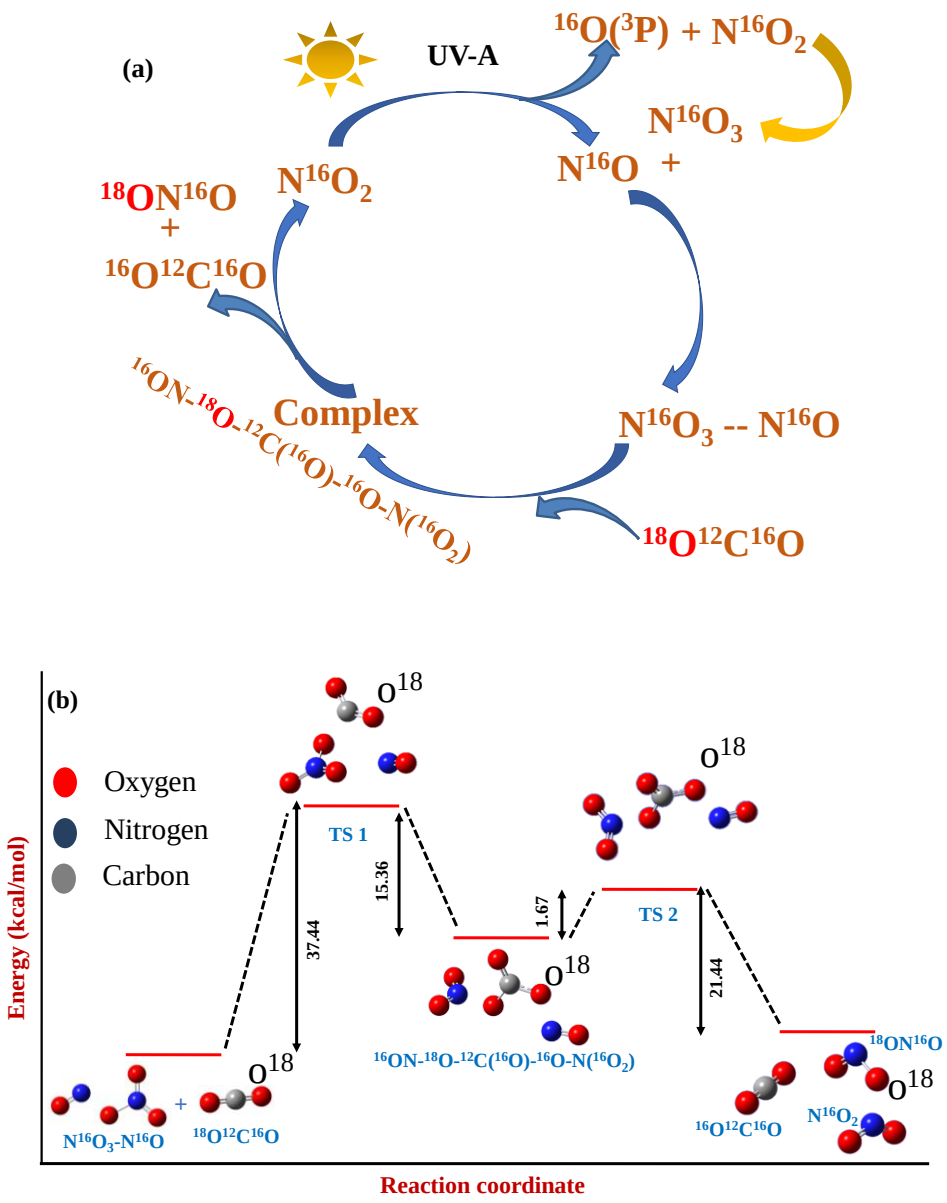

Figure 8.7: (a) *Main reactions involved in oxygen-atom exchange reaction.* **(b)** *Energy barrier between the reactant and products from the initial reactant* $N^{16}O_3 - N^{16}O$ *and* $^{18}O^{12}C^{16}O$ *calculated by DFT at 6311G++ (d,p) basis set using Gaussian 16.*

The energy barrier of the transition states, ^{16}ON-^{18}O-$^{12}C(^{16}O)$-^{16}O-$N(^{16}O_2)$ with respect to the reactant $N^{16}O_3 - N^{16}O$ and $^{18}O^{12}C^{16}O$ for the two steps are given in Figure 8.7b. It is quite evident that the transition state TS1 for the ^{16}ON-^{18}O-$^{12}C(^{16}O)$-^{16}O-$N(^{16}O_2)$ complex formation from $N^{16}O_3 - N^{16}O$ and $^{18}O^{12}C^{16}O$ (first step) has a barrier of 37.44 kcal mol^{-1} which is responsible to make the first step as a rate-determining slowest step with rate constant 1.36×10^{-16} cm^3 $molecule^{-1}$ s^{-1} at 298 K. It

has also been found that once the ^{16}ON-^{18}O-$^{12}C(^{16}O)$-^{16}O-$N(^{16}O_2)$ complex is formed, the dissociation of it to form $^{16}O^{12}C^{16}O$, $N^{16}O_2$ and $^{18}ON^{16}O$ overcomes a very low-barrier of 1.67 kcal mol^{-1}. Due to this near-barrierless, the breakdown of the ^{16}ON-^{18}O-$^{12}C(^{16}O)$-^{16}O-$N(^{16}O_2)$ complex occurs in a time scale ~13 nanosecond which corresponds to a rate constant of dissociation 7.64×10^7 s^{-1}. However, the energy-barrier of the first step is lower as compared to the previously reported barrier for ^{18}O-isotopic exchange between oxygen $^{16}O_2$ and $^{18}O^{12}C^{18}O$ which was 80 kcal mol^{-1}. In addition, the near-barrierless second step increases the overall ^{18}O-exchange reaction rate.

After calculating rate constants, we have utilized these in order to simulate$^{18}O^{12}C^{16}O$ concentration with the time of reaction. The relevant photochemistry and the set of reactions used to simulate the concentrations of $^{18}O^{12}C^{16}O$ are summarized in Table 8.2 along with the rate constants of the reactions. In the first step, $N^{16}O_2$ undergoes photolysis to form $N^{16}O$ and $O(^3P)$. The decay of NO_2 concentration due to photolysis was monitored by the CEAS technique exploiting the UV-Vis absorption spectroscopy as shown in Figure 8.8. The rate constant of the photolysis step has been determined from the slope of the first-order decay plot generated by plotting the logarithm function of the ratio of initial nitrogen dioxide concentration and the concentration of nitrogen dioxide with the time of photolysis ($\ln([NO_2]_0/[NO_2]_t)$) versus time of irradiation Figure 8.9. As both the isotopes of NO_2 ($N^{16}O_2$ and $^{18}ON^{16}O$) exhibit almost similar absorption due to their similar electronic energy level, change in individual concentrations $N^{16}O_2$ and$^{18}ON^{16}O$ isotopes of NO_2 could not be traced by this CEAS method. Moreover, the change in $N^{16}O_2$ and $^{18}ON^{16}O$ concentration due to isotopic exchange is much less compared to the change in NO_2 concentration due to photolysis. Therefore, the change in NO_2 concentration measured by UV visible cavity-enhanced spectroscopy could be considered solely due to photolysis of it. As a result, the photolysis rate constant was calculated from our experimentally measured value using cavity-enhanced absorption spectroscopy. The rate constants of the second step (R_2) and steps R_6-R_{13} are taken from the IUPAC kinetic database.[22]

The rate constants of the third (R_3), fourth (R_4) and fifth (R_5) steps were calculated with the help of KiSThelp software, where the output geometries of reactants, product complexes and transition states obtained from the Gaussian-16 calculation were used as input files for rate constant calculation exploiting the Transition State Theory.

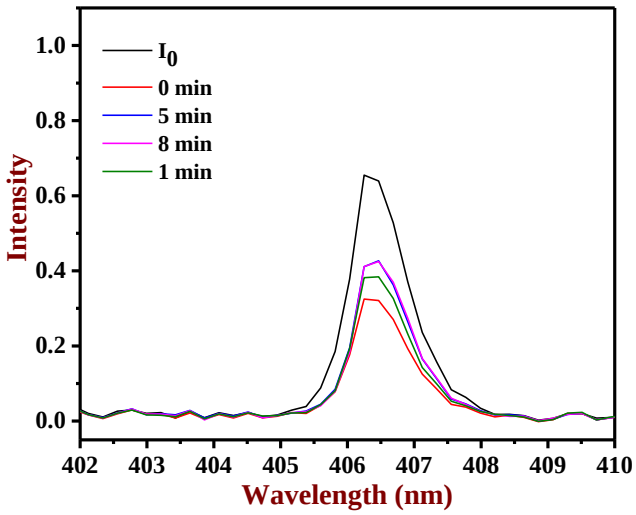

Figure 8.8: *Change of laser intensity in CEAS technique due to absorption of NO_2 and the variation of the intensity with the extent of photolysis.*

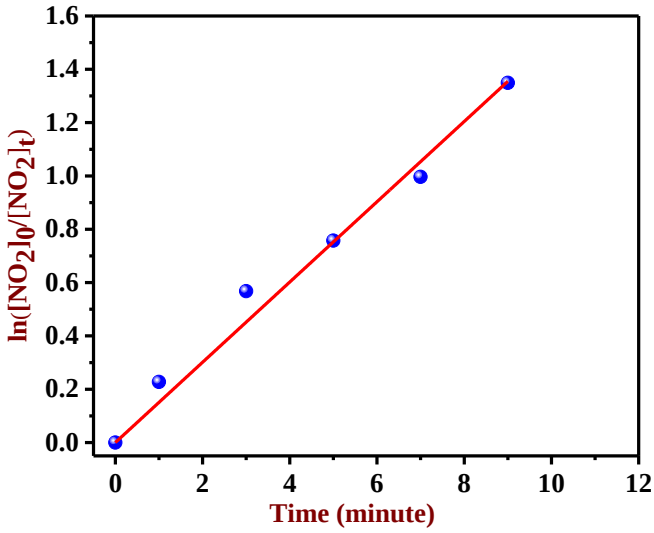

Figure 8.9: *First-order decay plot of $ln([NO_2]_0/[NO_2]_t)$ versus time for the calculation of photolysis rate constant.*

Table 8.2: *The relevant photochemistry and rate constants of the significant reactions involved in the isotopic exchange reaction*

Reactions	Rate constants
R_1. $N^{16}O_2 \rightarrow N^{16}O + O(^3P)$	$k_{photolysis} = 2.5 \times 10^{-3}\ s^{-1}$
R_2. $N^{16}O_2 + {}^{16}O(^3P) = N^{16}O_3$	$k_{NO3} = 2.30 \times 10^{-11}\ cm^3\ molecule^{-1}\ s^{-1}$
R_3. $N^{16}O_3$ -$N^{16}O + {}^{18}O^{12}C^{16}O \rightarrow$ Complex 1	$k_{fwd1} = 1.36 \times 10^{-16}\ cm^3\ molecule^{-1}\ s^{-1}$
R_4. Complex 1 $\rightarrow$ $N^{16}O_3$ -$N^{16}O + {}^{18}O^{12}C^{16}O$	$k_{back1} = 1.1\times10^{7}\ s^{-1}$
R_5. Complex 1$\rightarrow$ $NO^{16}O^{18} + NO_2 + CO_2$	$k_{fwd2} = 7.64\times 10^{7}\ s^{-1}$
R_6. $NO + NO_3 = NO_2 + NO_2$	$2.6\times10^{-11}\ cm^3\ molecule^{-1}\ s^{-1}$
R_7. $NO + O = NO_2$	$5.0\times10^{-11}\ cm^3\ molecule^{-1}\ s^{-1}$
R_8. $O + NO_2 = O_2 + NO$	$9.9\times10^{-12}\ cm^3\ molecule^{-1}\ s^{-1}$
R_9. $O + NO_3 = NO_2 + O_2$	$1.7\times10^{-11}\ cm^3\ molecule^{-1}\ s^{-1}$
R_{10}. $NO_2 + NO = N_2O_3$	$4.0\times10^{-12}\ cm^3\ molecule^{-1}\ s^{-1}$
R_{11}. $N_2O_3 = NO + NO_2$	$3.622\times10^{8}\ s^{-1}$
R_{12}. $NO_2 + NO_3 = N_2O_5$	$2.2\times10^{-12}\ cm^3\ molecule^{-1}\ s^{-1}$
R_{13}. $N_2O_5 = NO_2 + NO_3$	$6.9\times10^{-2}\ cm^3\ molecule^{-1}\ s^{-1}$

The detailed information of the different initial concentrations of the reactants used in the experiment as well as for modelling purposes for different sets of the studies are given in the Table 8.3. The experimental and modelled concentrations of $^{18}O^{12}C^{16}O$ after the same span of reaction time from different sets of studies are shown in Figure 8.10a. It is clearly evident here that our experimental results are in close agreement with that of the modelling studies, thus validating our proposed

reaction kinetics mechanisms underlying underlining pathways involved in the isotope exchange reaction.

Table 8.3: *Different sets having different initial concentrations of the reactants and final concentrations observed through experimental and modeled study with same reaction time.*

Sets	$N^{16}O_2$ (ppm)	$^{18}O^{12}C^{16}O$initial (ppb)	$^{18}O^{12}C^{16}O$final experimental (ppm)	$^{18}O^{12}C^{16}O$final modeling (ppm)
Set-1	512.13±0.35	1150.12±0.05	850.51±0.06	846.67
Set-2	363.45±0.35	671.15±0.07	489.76±0.09	481.67
Set-3	251.33±0.32	517.25±0.04	352.35±0.06	373.28
Set-4	93.14±0.32	275.26±0.06	236.08±0.04	210.25

To further validate and identify the most crucial reactions involved in isotope-exchange process, (listed in Table 8.2) we have done the sensitivity analysis using the reactions depicted in Figure 8.10b. In this analysis to verify the impact of a particular reaction on the product formation, the reaction modelling has been repeated by taking the rate constant of the reaction ten times than the calculated or supplied value. The rate constant of the reactions (given in Table 8.2) which has been increased by ten times, and the impact of change on $^{18}O^{12}C^{16}O$ concentration with respect to the predicted value has been given in Figure 8.10b.

From the analysis in Figure 8.10b, it is clearly evident that reaction the R_3 is the rate-determining step and significantly contributes to the isotopic exchange reaction. It has also been found from the given rate constants in Table 8.2 that the rate constant of reaction R_3 is the lowest among all the rate constants which is in the order of 10^{-16} cm^3 $molecule^{-1}$ s^{-1}. This suggests that the reaction R_3 is the rate-determining slowest step in the isotopic exchange reaction.

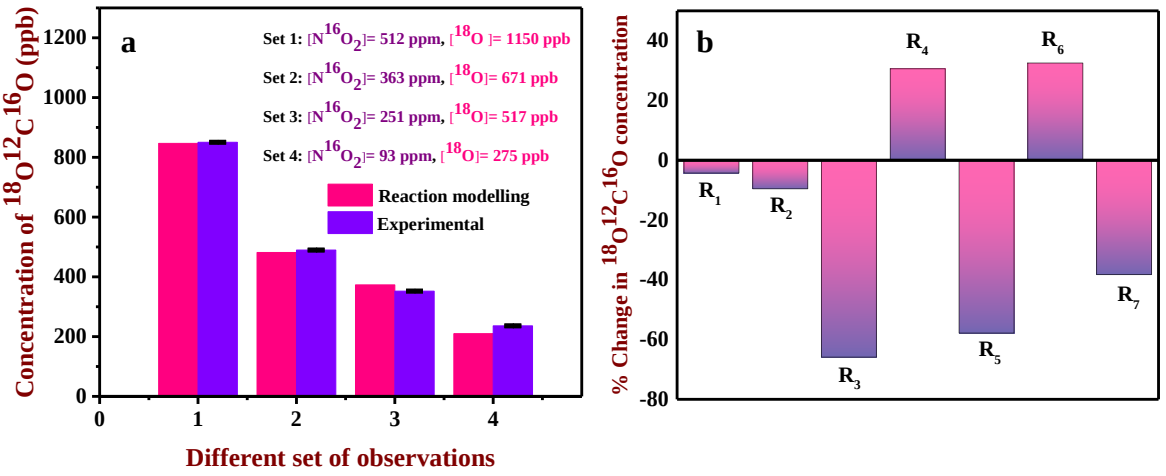

Figure 8.10: (a) *Comparison of experimental and modeled yields of $^{18}O^{12}C^{16}O$ isotope with different initial concentrations of the reactant $N^{16}O_2$ and $^{18}O^{12}C^{16}O$. Initial concentrations of the reactant species are given in the inset of figure.* **(b)** *Assessment of the most effective reaction on $^{18}O^{12}C^{16}O$ production in terms of % change in $^{18}O^{12}C^{16}O$ concentration with increasing rate of the reactions by ten times. The reaction numbers R_1 to R_6 are taken according to Table 8.2.*

8.4 Conclusion

In summary, our investigation gives the first direct experimental evidence of the gas-phase^{18}O-isotope exchange reaction between $^{18}O^{12}C^{16}O$ and $N^{16}O_2$ through a near-barrierless transition from a complex formed between $^{18}O^{12}C^{16}O$ and $N^{16}O_3$-$N^{16}O$. It is well-known that NO_2 and CO_2 are concurrently emitted from various anthropogenic sources like fossil fuel burning, vehicular emission, industrial emission etc., and the UV-A light is reasonably prevalent in the Earth's troposphere. Therefore, it becomes imperative to investigate the oxygen atom exchange reaction between them in response to the UV-A radiation in the lower atmosphere. Based on the high-resolution laser-based cavity-enhanced spectroscopic methods, our findings give evidence of how the heavy oxygen atom i.e.^{18}O isotope in CO_2 driven by near-UV radiation is transmitted to another important atmospheric species, such as NO_2 and how this two molecular species communicate isotopically. Our experimental

observations are substantiated through detailed theoretical calculations and reaction modelling studies. Our proposed underlying mechanisms and the reaction pathways revealed the existence of a near-barrierless transition state from an intermediate containing nitrate portion, which facilitates the transfer of the ^{18}O-isotope from $^{18}O^{12}C^{16}O$ to $N^{16}O_2$ leading to isotopic depletion of ^{18}O in $^{18}O^{12}C^{16}O$. In addition, the calculated reaction rates and new findings obtained in this study can be valuable for a range of atmospheric modelling endeavours and isotopic photochemistry providing enhanced fundamental insights into the atmospheric dynamic processes and isotope-specific chemical transformation mechanisms involved in the lower atmosphere. Several important gaps, however, may remain in our study and further laboratory experiments need to be done to fully understand the mystery of ^{18}O-isotopic communication and reaction dynamics. In view of the importance of CO_2 and NO_2, we have therefore taken for the first time, a major step towards unraveling a missing link of the UV-A driven ^{18}O-isotope exchange between them.

8.5 References

[1] M. C. Liang, G. A. Blake, B. R. Lewis, and Y. L. Yung "Oxygen Isotopic Composition of Carbon Dioxide in the Middle Atmosphere." *Proceedings of the National Academy of Sciences*, 104(1), 21 (2007).

[2] I.E. Gordon, L.S. Rothman, R.J. Hargreaves et al., "The HITRAN 2020 molecular spectroscopic database", *Journal of Quantitative Spectroscopy and Radiative Transfer*, 277, 107949 (2022).

[3] M. C. Liang, S. Mahata, A. H. Laskar, M. H. Thiemens, and S. Newman, "Oxygen Isotope Anomaly in Tropospheric CO_2 and Implications for CO_2 Residence Time in the Atmosphere and Gross Primary Productivity." *Scientific Reports*, 7(1), (2017).

[4] M. C. Liang, A. H. Laskar, E. Barkan, S. Newman, M. H. Thiemens, and R. Rangarajan, "New Constraints of Terrestrial and Oceanic Global Gross Primary Productions from the Triple Oxygen Isotopic Composition of Atmospheric CO_2 and O_2." *Scientific Reports*, 13(1), (2023).

[5] G. A. Adnew, T. L. Pons, G. Koren, W. Peters, and T. Röckmann, "Leaf-Scale Quantification of the Effect of Photosynthetic Gas Exchange on $\Delta^{17}O$ of Atmospheric CO_2." *Biogeosciences*, 17(14), 3903 (2022).

[6] J. Uchikawa, and R. E. Zeebe, "The Effect of Carbonic Anhydrase on the Kinetics and Equilibrium of the Oxygen Isotope Exchange in the CO_2–H_2O System: Implications for $\Delta^{18}O$ Vital Effects in Biogenic Carbonates." *Geochimica et Cosmochimica Acta*, 95, 15 (2012).

[7] S. P. Jones, A. Kaisermann, J. Ogée, S. Wohl, A. W. Cheesman, L. A. Cernusak, and L. Wingate, "Oxygen Isotope Exchange between Water and Carbon Dioxide in Soils Is Controlled by p^H, Nitrate and Microbial Biomass through Links to Carbonic Anhydrase Activity." *SOIL*, 7(1), 145 (2021).

[8] R. S. Bradley, "Chapter 1 - Paleoclimatic Reconstruction. In *Paleoclimatology (Third Edition)*" *Academic Press: San Diego.*, 1 (2015).

[9] H. Graven, R. F. Keeling, and J. Rogelj, "Changes to carbon isotopes in atmospheric CO_2 over the industrial era and into the future." *Global Biogeochemical Cycles*, 34, e2019GB006170 (2020).

[10] S. N. Vardag, S. Hammer, M. Sabasch, D. W. T. Griffith, and I. Levin, "First Continuous Measurements of $\Delta^{18}O$-CO_2 in Air with a Fourier Transform Infrared Spectrometer." *Atmospheric Measurement Techniques*, 8(2), 579 (2015).

[11] P. M. Steur, H. A. Scheeren, D. D. Nelson, J. B. McManus, and H. A. J. Meijer, "Simultaneous Measurement of $\delta^{13}C$ $\delta^{18}O$ and $\delta^{17}O$ of Atmospheric CO_2-Performance Assessment of a Dual-Laser Absorption Spectrometer." *Atmospheric Measurement Techniques*, 14(6), 4279 (2021).

[12] L. Y. Yeung, M. Okumura, J. T. Paci, G. C. Schatz, J. Zhang, and T. K. Minton, "Hyperthermal O-Atom Exchange Reaction O_2 + CO_2 through a CO_4 Intermediate." *Journal of the American Chemical Society*, 131(39), 13940 (2009).

[13] Y. L. Yung, W. B. DeMore, and J. P. Pinto, "Isotopic Exchange between Carbon Dioxide and Ozone via $O(^1D)$ in the Stratosphere." *Geophys Res Lett.*, 18(1), 13 (1991).

[14] C. G. MacDonald, J. P. Mastrogiacomo, J. L. Laughner, J. K. Hedelius, R. Nassar, and D. Wunch, "Estimating Enhancement Ratios of Nitrogen Dioxide, Carbon Monoxide and Carbon Dioxide Using Satellite Observations." *Atmospheric Chemistry and Physics*, 23(6), 3493 (2023).

[15] C. Ghosh, S. Mandal, M. Pal, M. Pradhan, "New Strategy for in Vitro Determination of Carbonic Anhydrase Activity from Analysis of Oxygen-18 Isotopes of CO_2." *Analytical Chemistry*, 90(2), 1384 (2018).

[16] A. Pal, K. Mondal, B. Panda, and M. Pradhan, "Development of a Compact 406 Nm Diode Laser-Based Cavity-Enhanced Spectrometer for High-Sensitive Detection of NO_2 Levels in Exhaust Gas." *Laser Physics Letters*, 20(7), 75701 (2023).

[17] M. J. Frisch, G. W. Trucks, H. B. Schlegel, G. E. Scuseria, M. Robb, J. R. Cheeseman, G. Scalmani, V. P. G. A. Barone, G. A. Petersson, H. J. R. A. Nakatsuji, and X. Li, "Gaussian 16," Revision A. 03, Gaussian. *Inc., Wallingford CT*, 3 *(*2016).

[18] S. Canneaux, F. Bohr, and E. Hénon, "KiSThelP: a program to predict thermodynamic properties and rate constants from quantum chemistry results", *Journal of Computational Chemistry*, 35, 82 (2014).

[19] W. Braun, J. T. Herron, and D. K. Kahaner, "Acuchem: A Computer Program for Modelling Complex Chemical Reaction Systems." *Int. J. Chem. Kinet.*, 20, 51 (1988).

[20] K. Mondal, S. Biswas, A. Chattopadhyay, P. Chatterjee, and T. Chakraborty, "Gas-Phase Oxidation of NO_2 to HNO_3 by Phenol: Atmospheric Implications." *ACS Earth and Space Chemistry*, 5, 2131 (2021).

[21] R. S. Zhu, K. Y. Lai, and M. C. Lin, "Ab Initio Chemical Kinetics for the Hydrolysis of N_2O_4 Isomers in the Gas Phase." *The Journal of Physical Chemistry A*, 116, 4466 (2012).

[22] R. Atkinson, D. L. Baulch, R. A. Cox, J. N. Crowley, R. F. Hampson, R. G. Hynes, M. E. Jenkin, M. J. Rossi, and J. Troe, "IUPAC Task Group on Atmospheric Chemical Kinetic Data Evaluation" *Atmospheric Chemistry and Physics*, 4, 1461 (2004).

Chapter: 9

Development of a LED based cavity-enhanced spectrometer for high-sensitive detection of diacetyl in gas phase

9.1 Introduction

Diacetyl is an organic molecule composed of four carbon, six hydrogen and two oxygen atoms. It is also known as 2,3-butanedione, with the molecular formula $C_4H_6O_2$. It is a vicinal diketone, means it has two carbonyl groups (C=O) that are adjacent to each other on the carbon chain.[1] Diacetyl is a natural byproduct of fermentation and is produced during the metabolism of certain microorganisms.[2-3] Diacetyl can also be synthesized chemically for various industrial applications, including its use in the production of flavourings and fragrances.[4-6] Exposure to high levels of diacetyl vapor has been associated with respiratory issues, leading to a condition known as bronchiolitis obliterans.[7-10] Therefore, gas phase detection of diacetyl is an important research area.

Diacetyl has a butterscotch-like aroma and it is widely used as a flavouring agents. It is an oxidative compound and has significant impact on cellular health. Diacetyl is a degradation product of different food components such as amino acids, fatty acids and carbohydrates.[11-13] An earlier research has shown diacetyl can be produced due to the action of lactic bacteria. Diacetyl is an important wine flavourant synthesized during alcoholic and malolactic fermentation.[14-16] Lactic acid bacteria under controlled physiological condition can produce diacetyl.[17-18] Diacetyl is found in several dairy products such as yogurt, butter, cheese, goat milk, cream and margarine in varied concentrations. In addition diacetyl is also found naturally in

some products like wine and coffee.[19-21] Further, diacetyl has high commercial importance and is manufactured to use as a food additive.

Over the decades the diacetyl was analysed and quantified using gas chromatography detection method. Several other methods used for the detection of this organic compound in subsequent time were high-performance liquid chromatography (HPLC), gas chromatography with a mass selective detector (GC-MS), fluorometric, colorimetric and liquid chromatography mass spectrometry (LC-MS).[22-29] Progressive advance of science and technology has led to the development of bio-sensors for the detection of diacetyl molecule.[30] Different techniques mentioned above are non-spectroscopic and most of them are applicable for liquid phase detection. All these measurement technique demands control and systematic process for sample preparation. Instantaneous gas phase detection of diacetyl molecule is highly required in the dairy farm and fermentation factory where huge numbers of workers are exposed to that environment.

In this work, we have developed a spectroscopic detection strategy for the precise detection of diacetyl molecule in gas phase. High finesse optical cavity was coupled with a LED light source operating at 450 nm. This detection technique is widely known as incoherent broadband cavity enhanced absorption spectroscopy (IBBCEAS). We have optically characterized the spectrometer in details, checked the stability and optimized, and calibrated this developed diacetyl sensor system for real sample analysis. Finally, we have demonstrated the spectrometers for diacetyl detection from different curd samples and beer.

9.2 Experimental

A representation of the experimental setup based on IBBCEAS is depicted in Figure 9.1. We have utilized a LED (M450LP2, Thorlabs) with a centre wavelength ~ 450 nm and output power of ~ 140 mW at 1200 mA input current as an optical light source. Here, a power supply (upLED) was used to operate the LED in continuous mode by modulating the current (0 – 1200 mA), which in turn will vary the intensity of the light emitted from the LED. The diverging light emitted from the LED was primarily passed through an iris diaphragm and then the light was passed through a plano-

convex lens (LA1509-A, Thorlabs) to converge the light beam and couple it into the high finesse optical cavity. The optical cavity was composed of quartz coated 30 cm long cavity attached with two high-reflective (HR) plano-concave mirrors (149645 Layertec) at its both end. High-reflective (HR) mirrors has reflectivity of R > 99.98% for 400-800 nm and 1 m radius of curvature (ROC) as specified by manufacturer. Further, transmitted light from the optical cavity was focused onto the tip of an optical fiber (MF11L1, Thorlabs), utilizing a plano-convex lens (LA1422-A). Ultimately, a spectrometer (CCS-200, Thorlabs) was employed to capture the output optical signal, and the data were acquired through the spectrometer software on a personal computer. To ensure optimal pressure within the cavity, a high-pressure Pirani gauge (CMR 361, Pfeiffer Vacuum) was connected to the optical cavity.

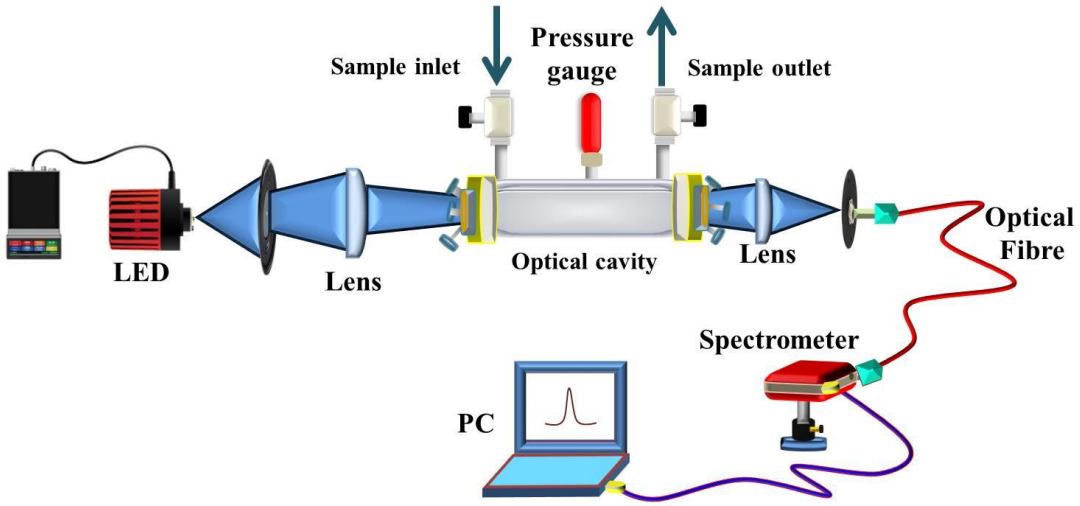

Figure 9.1: *A representation of the developed IBBCEAS setup.*

9.3 Results and discussions

Diacetyl molecule has significant absorption feature in the UV-Visible region. We have selected the LED source with central wavelength around 450 nm to develop the IBBCEAS setup for the gas phase detection of diacetyl molecule in trace levels. The LED profile was accumulated with the spectrometer and fitted with the Gaussian line shape function as shown in Figure 9.2a. We obtained the line-width of this LED source to be ~ 18 nm. The absorption cross-section of diacetyle is in the order of ~10-

^{20} cm^2 molecule^{-1} for the wavelength region of 440 nm to 460 nm. More specifically the absorption cross-section of diacetyl is 4.06 X 10^{-20} cm^2 molecule^{-1} at 450 nm, which is the wavelength of our interest for this experimental setup development.

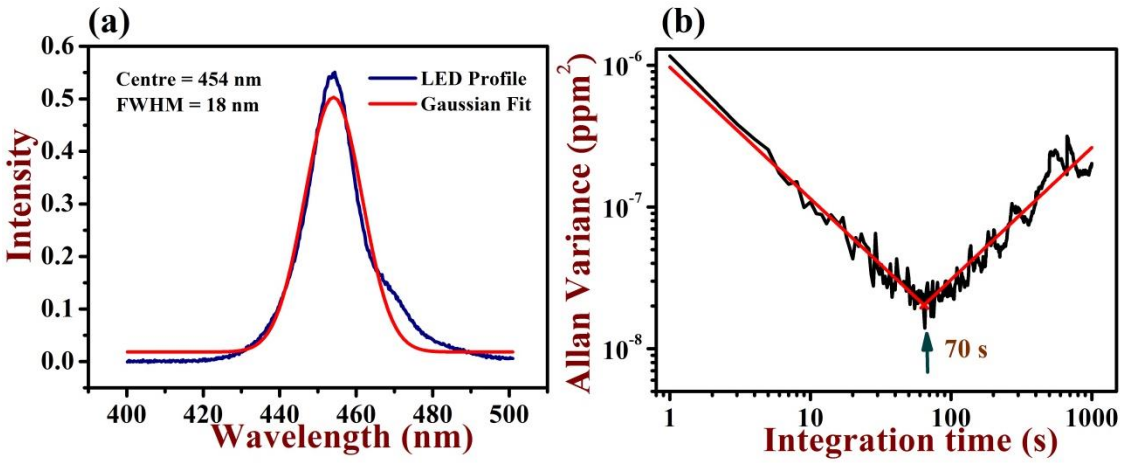

Figure 9.2: (a) *LED profile fitted with Gaussian line shape function depicts the centre wavelength and line width.* **(b)** *Allan variance analysis to find the stability of the developed sensor system.*

We investigated the stability of the developed incoherent broadband cavity enhanced spectrometer by means of Allan variance analysis. This analysis will help us to determine the optimum integration time to improve the limiting sensitivity by maximizing the signal to noise ratio. We have captured the empty cavity transmitted intensity profile for consecutive two hours in the interval of four seconds. Figure 9.2b shows the plot of the Allan variance versus integration time. On successive averaging of the data it was observed that the Allan variance decreasing linearly depicting the white noise region. Hence, we achieved the optimum integration time of ~ 70 s corresponding to 4 s data acquisition time of an empty cavity transmitted light intensity. After this 70 s optimum time various fluctuations come into scenario, therefore further data averaging did not yield better signal-to-noise ratios. The Allan variance analysis also allows us to determine the precision of the measurement i.e. how precisely we can measure the concentration with our developed cavity-enhanced sensor system. From the Allan variance plot, the precision estimated to be ~ 0.1 ppb corresponds to 70 s optimum integration time.

The known concentration of nitrogen dioxide was employed to determine the optical path length of our developed IBBCEAS setup for the precise detection of diacetyl molecule from different sources. High-sensitive CRDS coupled with QCL was utilised to measure the concentration of nitrogen dioxide.

We have utilized pure nitrogen dioxide (NO_2) gas (INTERGAS, Newfield Industrial Estate, 99.5% Grade) diluted with ultra-high purity (UHP) nitrogen gas to determine the path length of our developed IBBCEAS setup. We have selected the interference free ro-vibrational transition line of NO_2 to determine its concentration exploiting the high-sensitive cavity ring-down spectroscopy coupled with quantum cascade laser operating at 6.2 μm wavelength region. We have captured the spectral trace of NO_2 by varying the pressure inside the cavity using the diluted mixture of NO_2 with nitrogen shown in Figure 9.3. Then the peak centre at 1632.6777 cm^{-1} with absorption cross-section 5.189 X 10^{-20} cm^2 $molecule^{-1}$ was considered to evaluate the mixing ratio from the slope of the peak-area vs pressure curve Figure 9.4. The spectral trace was fitted with voigt line shape function to find the peak area. We obtained the mixing ratio for NO_2 in this prepared gas mixture to be 910 ppb (parts per billion by volume). This same gas mixture was then injected into the cavity of the developed IBBCEAS setup to determine its path length from the intensity drop utilizing Beer-Lambert law.

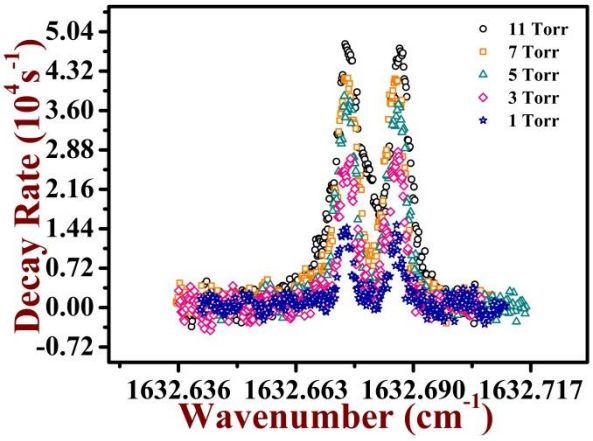

Figure 9.3: *CRDS spectra of NO_2 for the prepared gas mixture.*

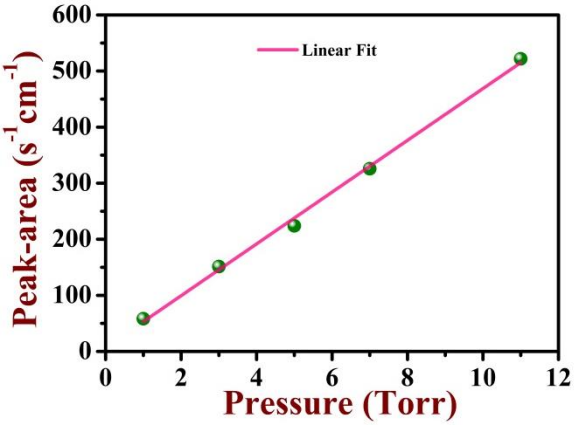

Figure 9.4: *Plot of peak-area vs pressure and fitted with linear regression.*

We have introduced this nitrogen dioxide gas inside the optical cavity to observe the value of intensity change (Figure 9.5) and using the Beer-Lambert law (equation 9.1) we have evaluated the optical path length of the developed IBBCEAS setup.

$$I(\lambda) = I_0(\lambda)e^{(-L[X]\sigma_\lambda)} \quad \textbf{(9.1)}$$

where, $I_0(\lambda)$ is the intensity when the cavity is empty, $I(\lambda)$ is the intensity when the cavity is filled with sample, L is the effective path length through the sample, [X] is the concentration of molecular species and σ_λ is the absorption cross-section.

Equation 9.1 can be re-written as:

$$L = \frac{\ln\left(\frac{I_0}{I}\right)}{[X]\sigma_\lambda} \quad \textbf{(9.2)}$$

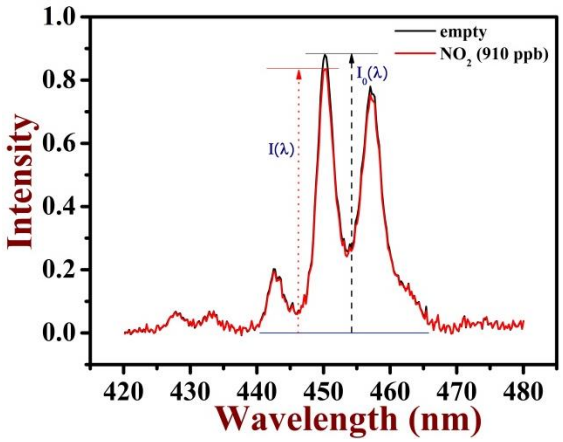

Figure 9.5: *Intensity change by inserting 910 ppb NO_2 to determine the optical path length of the developed sensor.*

The absorption cross-section of nitrogen dioxide at 450 nm wavelength is 4.272 X 10^{-19} cm^2 $molecule^{-1}$ and we have utilized the known concentration of NO_2 (910 ppb) for path length calculation of the developed sensor. Optical cavity was filled with known concentration of NO_2 at 95 Torr cavity pressure. Based on these parameters we have obtained the optical path length of our developed IBBCEAS setup to be 4.5 kilo-meters. Hence, we have evaluated the mirror reflectivity to be ~99.99% for 450 nm wavelength region. Minimum absorption coefficient i.e. the limiting sensitivity of the present IBBCEAS setup was estimated to be $\alpha_{min} = 2.51\times10^{-8}$ cm^{-1}. A typical detection limit for diacetyl in terms of mixing ratio corresponding to absorption cross-section of 4.06 X 10^{-20} cm^2 $molecule^{-1}$ at a 100 Torr cavity pressure was determined to be ~ 190 ppb (parts per billion, 1 part in 10^9).

Next, to validate and verified whether our developed sensor can really able to sense the diacetyl molecule. Hence, we have utilized 2,3-Butanedione (97 % pure, Sigma Aldrich) for our experiment. We have taken the liquid diacetyl molecule in sample vial and collected the gas from the head space of the sample vial in a controlled way. As the vapour pressure of diacetyl is significantly high which implies that the concentration of diacetyl in the gas sample collected from head space will also be high, so direct insertion of this sample inside the optical cavity may lead to saturation of the transmitted signal. Therefore, we have mixed this sample with ultra-high purity (UHP) nitrogen gas to dilute it to some standard concentrations. The collected gas sample from the head space was mixed with nitrogen gas in different mixing ratios to obtain various concentration of diacetyl.

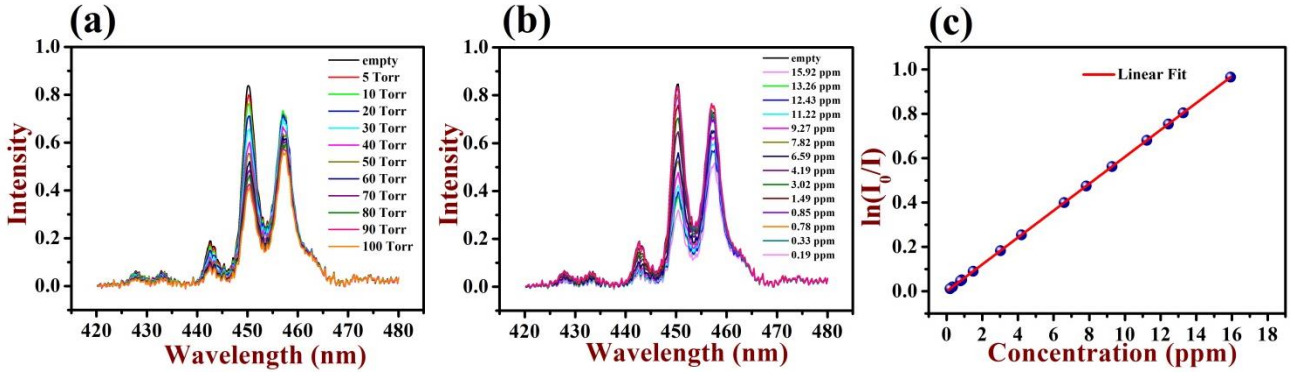

Figure 9.6: **(a)** *Variation of intensity due to absorption at different pressure for known diacetyl gas concentration.* **(b)** *Variation of intensity of laser spectra due to absorption for*

different known concentrations of diacetyl gas. **(c)** *Calibration curve representing a linear nature between ln(I_0/I) verses different mixing ratios.*

Figure 9.6a and 9.6b clearly depicts that our developed setup is fully able to detect the diacetyl concentration in the collected air sample. Primarily we have taken the gas sample containing 11 ppm diacetyl. Further, we injected this gas mixture inside the optical cavity and varied the cavity pressure from 5 Torr to 100 Torr (Figure 9.6a). It was observe from the Figure 9.6a that with the increase in pressure the absorption becomes much more prominent. This happens because number of molecule per unit volume increases with increase in pressure, hence number of diacetyl molecule contributing for absorption increases, therefore absorption enhances gradually with increase in pressure. Since, we have observed the maximum absorption for 100 Torr cavity pressure so we have maintained this pressure inside the optical cavity throughout our experiment. Subsequently, we have injected the gas samples with different diacetyl concentration varying from 15.92 ppm to 0.19 ppm and acquired the transmitted intensity profile depicted in Figure 9.6b. As with the increase in concentration number of molecule per unit volume increases therefore we found that the absorption drops significantly with increase in diacetyl concentration. Then, we have plotted $\ln(I_0/I)$ vs concentration and obtain the linear relationship among them (Figure 9.6c) validating the Beer-Lambert law. Further, we have fitted this plot with a linear regression and the slope obtained will allow us to determine the concentration of diacetyl content in any gas sample limited to the detection limit of our developed setup by knowing the value of I_o and I experimentally.

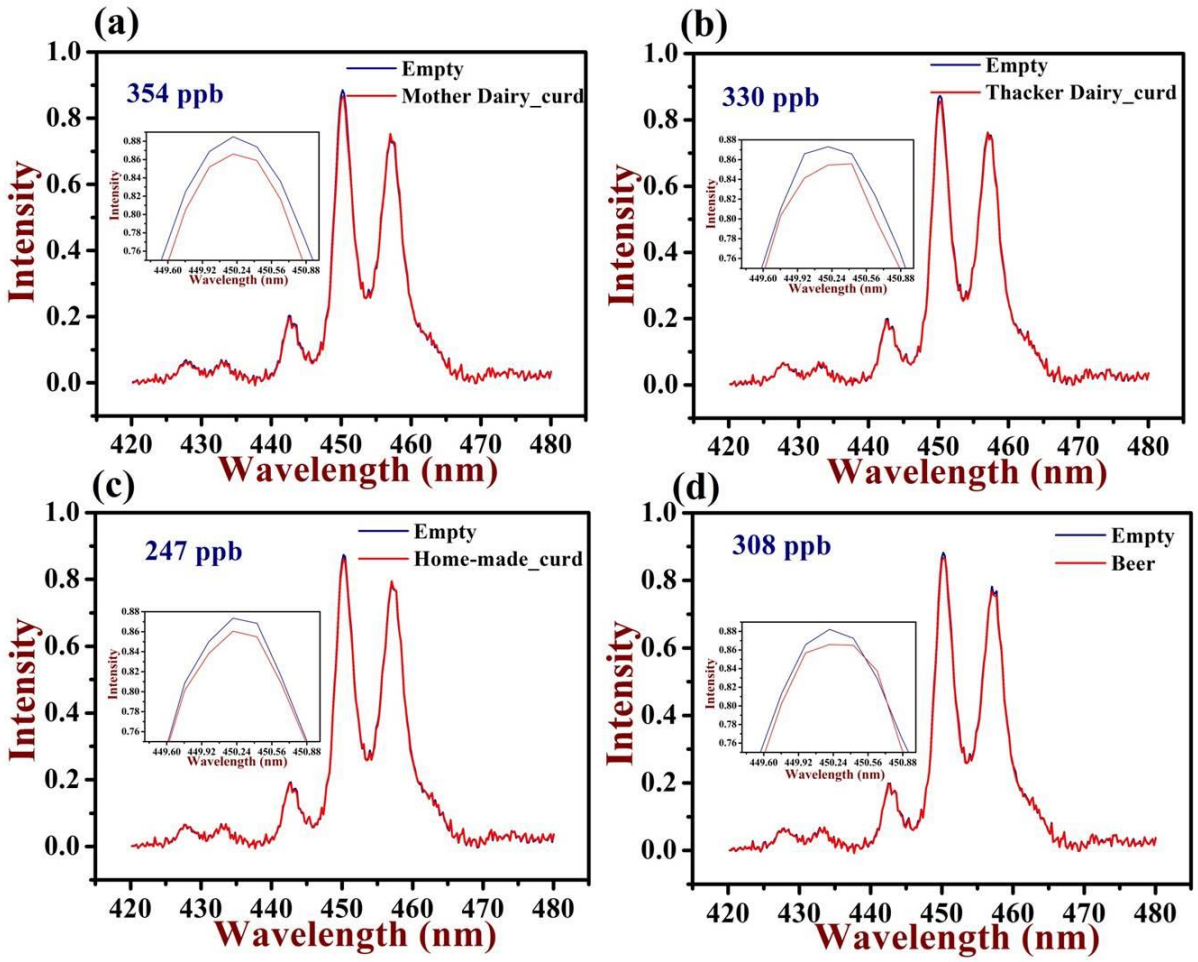

Figure 9.7: (a), (b), (c) & (d) *Drop in intensity for gas samples collected from mother dairy curd, thacker dairy curd, home-made curd and beer due to the presence of diacetyl.*

Finally, we have measured the concentration of diacetyl molecule in various gas samples collected from different sources. We have broadly selected two types of sample curd and beer. Among this curd we have taken three different categories of curds one was home-made and other two were from mother dairy and thacker dairy. So, in total we have tested for four different samples. Henceforth, to measure the concentration of diacetyl molecule we have collected the gas sample from the head space of the container containing these curd and beer. Then we have injected these samples into the optical cavity of our developed system one by one to obtain the value of drop down intensity (I) due to absorption Figure 9.7. Therefore, we obtained the diacetyl concentration to be 354 ppb, 330 ppb, 247 ppb and 308 ppb for mother dairy curd, thacker dairy curd, home-made curd and beer, respectively.

Taken together, this study will open an avenue for the gas phase spectroscopic detection of diacetyl molecule.

9.4 Conclusions

In summary, we have designed, developed and implemented a simple optical sensor system at 450 nm vis-region for sensitive detection of diacetyl based on optical incoherent broadband cavity-enhanced absorption spectroscopy technique. Detection limit of 190 ppb for diacetyl was achieved with a data acquisition time of ~ 4 s. An effective optical path-length of 4.5 km was achieved within the high-finesse optical cavity. We have utilized the developed sensor for the detection of diacetyl levels in the gas samples collected from head space of curd and beer container. This setup can be further employed for the detection of real-time diacetyl concentration in the air of the dairy farms and fermentation factories. This in turn will allow to control and regulate the air quality standards in those places and help the workers to take proper precautions to restrict the inhalation of this air.

9.5 References

[1] D. J. Hewitt, "Diacetyl." *Hamilton & Hardy's Industrial Toxicology*, 683 (2015).

[2] I. Rosca, A. R. Petrovici, M. Brebu, I. Stoica, B. Minea and N. Marangoci, "An original method for producing acetaldehyde and diacetyl by yeast fermentation." *Brazilian journal of microbiology*, 47, 949 (2016).

[3] Y. Wang, W. Sun, S. Zheng, Y. Zhang and Y. Bao, "Genetic engineering of Bacillus sp. and fermentation process optimizing for diacetyl production." *Journal of biotechnology*, 301, 2 (2019).

[4] W. Hao, F. Ji, J. Wang, Y. Wang, Y. Zhang, and Y. Bao, "Metabolic engineering of Bacillus sp. for diacetyl production." *Process Biochemistry*, 58, 69 (2017).

[5] L. F. Chuang, and E. B. Collins, "Inhibition of Diacetyl Synthesis by Valine and the Roles of α-Ketoisovaleric Acid in the Synthesis of Diacetyl by Saccharomyces cerevisiae." *Microbiology*, 72(1), 201 (1972).

[6] D. K. Verma, S. T. G. Al-Sahlany, A. K. Niamah, M. Thakur, N. Shah, S. Singh, D. Baranwal, A. R. Patel, G. L. Utama, and C. N. Aguilar, "Recent trends in microbial

flavour Compounds: A review on Chemistry, synthesis mechanism and their application in food." *Saudi Journal of Biological Sciences*, 29(3), 1565 (2022).

[7] P. Harber, K. Saechao and C. Boomus, "Diacetyl-induced lung disease." *Toxicological reviews*, 25, 261 (2006).

[8] F. G. B. G. J. Van Rooy, L. A. Smit, R. Houba, V. A. Zaat, J. M. Rooyackers, and D. J. Heederik, "A cross-sectional study of lung function and respiratory symptoms among chemical workers producing diacetyl for food flavourings." *Occupational and environmental medicine*, 66(2), 105 (2009).

[9] F. G. van Rooy, J. M. Rooyackers, M. Prokop, R. Houba, L. A. Smit, and D. J. Heederik, "Bronchiolitis obliterans syndrome in chemical workers producing diacetyl for food flavorings." *American journal of respiratory and critical care medicine*, 176(5), 498 (2007).

[10] D. L. Morgan, G. P. Flake, P. J. Kirby, and S. M. Palmer, "Respiratory toxicity of diacetyl in C57BL/6 mice." *Toxicological* sciences, 103(1), 169 (2008).

[11] T. Shibamoto, "Diacetyl: occurrence, analysis, and toxicity." *Journal of agricultural and food chemistry*, 62(18), 4048 (2014).

[12] T. Kaneko, H. Suzuki, and T. Takahashi, "Diacetyl formation and degradation by Streptococcus lactis subsp. diacetylactis 3022." *Agricultural and biological chemistry*, 50(10), 2639 (1986).

[13] A. Harden, and D. Norris, "The diacetyl reaction for proteins." *The Journal of Physiology*, 42(4), 332 (1911).

[14] E. J. Bartowsky, and P. A. Henschke, "The 'buttery'attribute of wine—diacetyl—desirability, spoilage and beyond." *International journal of food microbiology*, 96(3), 235 (2004).

[15] B. Martineau, T.E. Acree, and T. Henick-Kling, "Effect of wine type on the detection threshold for diacetyl." *Food Research International*, 28(2), 139 (1995).

[16] Y. Hayasaka, and E. J. Bartowsky, "Analysis of diacetyl in wine using solid-phase microextraction combined with gas chromatography− mass spectrometry." *Journal of Agricultural and Food Chemistry*, 47(2), 612 (1999).

[17] J. Hugenholtz, and M. J. Starrenburg, "Diacetyl production by different strains of Lactococcus lactis subsp. lactis var. diacetylactis and Leuconostoc spp." *Applied Microbiology and Biotechnology*, 38, 17 (1992).

[18] T. Bintsis, "Lactic acid bacteria as starter cultures: An update in their metabolism and genetics." *AIMS microbiology*, 4(4), 665 (2018).

[19] M. I. Rincon-Delgadillo, A. Lopez-Hernandez, I. Wijaya, and S.A. Rankin, "Diacetyl levels and volatile profiles of commercial starter distillates and selected dairy foods." *Journal of dairy science*, 95(3), 1128 (2012).

[20] S. Clark, and C. K. Winter, "Diacetyl in foods: a review of safety and sensory characteristics." *Comprehensive Reviews in Food Science and Food Safety*, 14(5), 634 (2015).

[21] R. Attaie, "Quantification of volatile compounds in goat milk Jack cheese using static headspace gas chromatography." *Journal of Dairy science*, 92(6), 2435 (2009).

[22] T. Shibamoto, "Analytical methods for trace levels of reactive carbonyl compounds formed in lipid peroxidation systems." *Journal of pharmaceutical and biomedical analysis*, 41(1), 12 (2006).

[23] G.D. Revel, L. Pripis-Nicolau, J. C. Barbe, and A. Bertrand, "The detection of α-dicarbonyl compounds in wine by formation of quinoxaline derivatives." *Journal of the Science of Food and Agriculture*, 80(1), 102 (2000).

[24] H. Cheng, "Volatile flavor compounds in yogurt: A review." *Critical reviews in food science and nutrition*, 50(10), 938 (2010).

[25] X. Li, A. Duerkop, and O. S. Wolfbeis, "A fluorescent probe for diacetyl detection." *Journal of fluorescence*, 19, 601 (2009).

[26] S. L. McCarthy, "Analysis of diacetyl and 2, 3-pentanedione in beer by HPLC with fluorometric detection." *Journal of the American Society of Brewing Chemists*, 53(4), 178 (1995).

[27] E. Stotz, and J. Raborg, "A colorimetric determination of acetoin and diacetyl." *Journal of Biological Chemistry*, 150(1), 25 (1943).

[28] J. Zhao, Y. Shin, Y. Jin, K. M. Jeong, and J. Lee, "Determination of enantiomeric vigabatrin by derivatization with diacetyl-l-tartaric anhydride followed by ultra-high performance liquid chromatography-quadrupole-time-of-flight mass spectrometry." *Journal of Chromatography B*, 1040, 199 (2017).

[29] P. Li, Y. Zhu, S. He, J. Fan, Q. Hu, and Y. Cao, "Development and validation of a high-performance liquid chromatography method for the determination of diacetyl in beer using 4-nitro-o-phenylenediamine as the derivatization reagent." *Journal of agricultural and food chemistry*, 60(12), 3013 (2012).

[30] J. A. Hernandez-Valdes, A. Solopova, and O. P. Kuipers, "Development of Lactococcus lactis biosensors for detection of diacetyl." *Frontiers in Microbiology*, 11, 1032 (2020).

Chapter: 10

Summary and future perspective

10.1 Summary of the thesis

The works in this thesis involved the development, design, implementation and utilization of different variants of cavity enhanced absorption spectroscopy technique such as cavity ring down spectroscopy, integrated cavity output spectroscopy and incoherent broadband cavity enhanced spectroscopy for detection, isotopic exchange study and fundamental spectroscopic analysis of trace molecules and their isotopes.

Λ-type and *l*-type doublets are very fundamental molecular property found in diatomic and linear polyatomic molecules, respectively. Those doublet spectral transitions were studied to explore various spectroscopic properties using the above mentiond spectroscopic techniques. High-resolution spectroscopic investigation of *l*-type doubling of β-N_2O was performed in the ν_1 fundamental vibration band at 7.8 μm using the *cw* EC-QCL based ultra-sensitive CRDS technique. We probed 32 *l*-type doublet spectral lines corresponding to the P- and R-branches in the $(11^10)\leftarrow(01^10)$ transition. We also probed the $(12^20)\leftarrow(02^20)$ ro-vibrational transition of β-N_2O to observe the fine structure splittings between the e and f sub-states in Δ vibrational state. Further, we have analysed these experimentally obtained spectral doublets to determine several new spectroscopic parameters such as *l*-type doubling constants, Coriolis constants, rotational constants and centrifugal distortion constants. We also performed the pressure broadening effects on the doublets at room temperature and subsequently determined the broadening coefficients of e and f sub-states to understand the pressure-induced spectral features. We have utilized the highly-sensitive CRDS technique coupled with the EC-QCL radiation source for studying the Λ-doublets of nitric oxide (NO) in the $(^2\prod_{1/2}, 1)\leftarrow(^2\prod_{1/2}, 0)$ and $(^2\prod_{3/2}, 1)\leftarrow(^2\prod_{3/2}, 0)$ vibrational transitions near 5.2 μm. the Λ-doublet splittings between the e and f

sub-states of 33 ro-vibrational spectral lines in the R-branch belonging to the above mentioned transitions were acquired experimentally. Some fundamental spectroscopic parameters like Λ-type doubling constants, Herman-Wallis coefficients and vibrational transition dipole moments were evaluated from these experimentall obtained spectral transitions. We have performed the pressure broadening study of the Λ-doublets in collision with zero air, He and Ar as perturbing gases and their J-dependence were investigated.

Next, we have developed a compact spectrometer exploiting cavity enhance absorption spectroscopy coupled with diode laser operating at 406 nm for the precise detection of nitrogen dioxide. We have utilized this sensor system for the high-sensitive and selective measurement of NO_2 in an interference-free absorptive region and free of aerosol indeed Rayleigh and Mie scatterings. Nitrogen dioxide content in the vehicular exhaust gases were also measured with this developed setup. Utilizing this developed setup and ICOS spectroscopic methods, our findings give evidence of how the heavy oxygen isotope in CO_2 driven by near-UV radiation is transmitted to another important atmospheric species, such as NO_2 and how this two molecular species communicate isotopically. Our experimental observations are substantiated through detailed theoretical calculations and reaction modelling studies. Our proposed underlying mechanisms and the reaction pathways revealed the existence of a near-barrierless transition state from an intermediate containing nitrate portion, which facilitates the transfer of the ^{18}O-isotope from $^{18}O^{12}C^{16}O$ to $N^{16}O_2$ leading to isotopic depletion of ^{18}O in $^{18}O^{12}C^{16}O$. In addition, the calculated reaction rates and new findings obtained in this study can be valuable for a range of atmospheric modelling endeavours and isotopic photochemistry providing enhanced fundamental insights into the atmospheric dynamic processes and isotope-specific chemical transformation mechanisms involved in the lower atmosphere. Further, we have designed, developed and implemented a simple optical sensor system at 450 nm vis-region for sensitive detection of diacetyl based on optical incoherent broadband cavity-enhanced absorption spectroscopy technique. Detection limit we have achieved for the detection of diacetyl was 190 ppb. We have

utilized the developed sensor for the detection of diacetyl levels in the gas samples collected from head space of curd and beer container.

10.2 Future perspective

10.2.1 Fundamental spectroscopic study of α-nitrous oxide

In chapter 4 and chapter 5, we have discussed the fundamental spectroscopic study of β-nitrous oxide. α-nitrous oxide also possess the *l*-type doublet feature. Therefore, we will utilize the cavity rind down spectroscopy coupled with quantum cascade laser to obtain the *l*-type doublet spectral transitions for α-nitrous oxide. Various spectroscopic parameters will be evaluated and we will compare those parameters with our previously obtained parameters for β-nitrous oxide. This will help us to clearly differentiate and distinguish between the site specific nature of the nitrous oxide isotope. We will try to simultaneously detect the α-nitrous oxide and β-nitrous oxide by capturing them in a single laser scan over the region of 0.1 cm^{-1}.

10.2.2 Study of nitrogen dioxide from car exhaust

In chapter 7, the developed CEAS technique coupled with diode laser operating at 406 nm was demonstrated for the detection of NO_2 present in the exhaust gases. We a future plane to utilize this developed setup to observe the concentration of NO_2 released from different four wheeler vehicles depending on their engine capacity. We will also like to see how this NO_2 concentration varies with the aging of the engine, engine operated at different speed and after varied hours of continuous engine operation. Further, it should be mention that the similar setup could be used for detection of other important trace gases just by modifying the setup with the optical source of that specified wavelength.

10.2.3 Develop and work on different experimental techniques

Most of the work in this thesis is related to the gas phase studies. I have interest to explore and extend my knowledge towards condensed phase and nanoparticle chemistry. To work in this area two experimental techniques like evanescent wave cavity ring-down spectroscopy (Ew-CRDS) and surface plasmon resonance (SPR) are

widely used along with other well known techniques. So selecting some specific system and working in this techniques will allow me acquire knowledge and enhance my research field.